universität wien

MASTERARBEIT / MASTER'S THESIS

Titel der Masterarbeit / Title of the Master's Thesis

„Polygonal Impact Craters (PICs) on Rhea, Dione, Tethys, Ceres and Vesta"

verfasst von / submitted by

Tanja Neidhart, BSc

angestrebter akademischer Grad / in partial fulfilment of the requirements for the degree of

Master of Science (MSc)

Wien, 2018 / Vienna 2018

Studienkennzahl lt. Studienblatt / degree programme code as it appears on the student record sheet:	A 066 861
Studienrichtung lt. Studienblatt / degree programme as it appears on the student record sheet:	Astronomie
Betreut von / Supervisor:	Univ.-Prof. Dr. Maria Gertrude Firneis

Contents

Acknowledgements

First of all, I would like to express my gratitude to my supervisor Univ.-Prof. Dr. Maria Firneis (Institute of Astrophysics, University of Vienna) for her continuous support and motivation during the time I worked on this thesis.

Further, I would like to thank Dr. Johannes Leitner (Research Platform: ExoLife, University of Vienna) for his advice, patient guidance, and endless discussions on the topic of this thesis and science in general.

Special thanks are also due to Florian Hofbauer, BSc (Institute of Pathology, Karl Landsteiner University, Krems) for his patience while helping me with the installation of ISIS 3.

I owe my deepest gratitude to my parents, for their continual support and encouragement. They have enabled me to pursue all my interests and always believed in me.

Finally, I would also like to give thanks to my family and friends for their support during my work on this thesis and for my life in general.

List of Figures

Ich habe mich bemüht, sämtliche Inhaber der Bildrechte ausfindig zu machen, und ihre Zustimmung zur Verwendung der Bilder in dieser Arbeit eingeholt. Sollte dennoch eine Urheberrechtsverletzung bekannt werden, ersuche ich um Meldung bei mir.

List of Tables

List of Abbreviations

APOD	Astronomy Picture of the Day
AU	Astronomical Unit
CIC	Circular Impact Crater
CICs	Circular Impact Craters
$\mathbf{D}_{tr}$	Simple-to-complex transition diameter
DLR	German Aerospace Center
ESA	European Space Agency
GIMP	GNU Image Manipulation Program
HED	Howardite–Eucrite–Diogenite
IAU	International Astronomical Union
IC	Impact Crater
ICs	Impact Craters
IDA	Institute for Defense Analyses
ISIS	Integrated Software for Imagers and Spectrometers
JPL	Jet Propulsion Laboratory
MPS	Max Planck Institute
NASA	National Aeronautics and Space Administration
PIC	Polygonal Impact Crater
PICs	Polygonal Impact Craters
PSI	Planetary Science Institute
SAR	Synthetic Aperture Radar
SSI	Space Science Institute
UCLA	University of California, Los Angeles
USGS	United States Geological Survey

1 Introduction

1.1 Definition of a Polygonal Impact Crater (PIC)

A polygonal impact crater (PIC) is a crater whose crater rim does not have a circular shape in plane view but shows straight crater rim segments. Such craters exist on all objects in our Solar System that have a cratered surface (see Fig. 1.1).

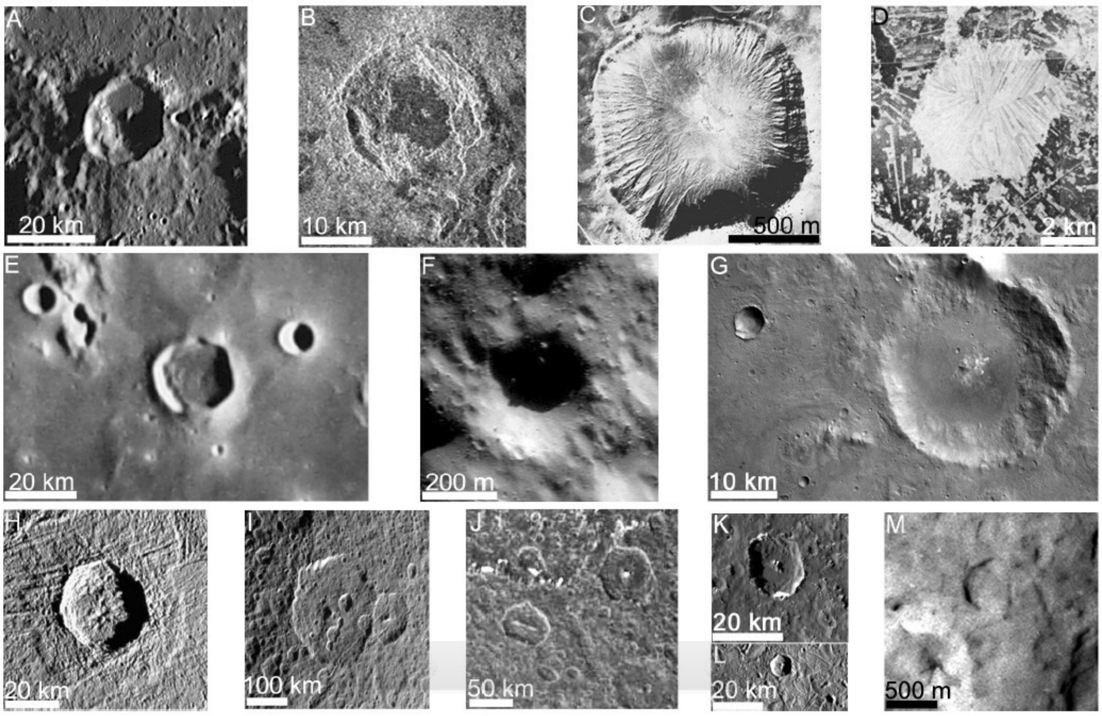

Figure 1.1: Examples of PICs on several bodies of the Solar System. A) Mercury. B) Venus. C) Earth (Meteor Crater). D) Earth (Söderfjärden impact structure). E) Moon. F) Eros. G) Mars. H) Ganymede. I) Rhea. J) Iapetus. K) Callisto. L) Europa. M) P/Wild-2. Credit: Öhman (2009), p. 93, and references therein.

Previous studies have shown that on Mercury, Venus, Mars, and the Moon about 10-25% of craters are polygonal (Weihs et al., 2015; Aittola et al., 2010; Öhman et al., 2008; Öhman et al., 2010). Beddingfield et al. (2016) studied PICs on the Saturnian satellite Dione, finding that 76% of the impact craters analysed in the "wispy" terrain (a region showing large visible fractures), and 35% of impact craters outside the wispy terrain have at least one straight crater rim segment. Former investigations on Ceres found 258 PICs, most of them having diameters between 10 km and 50 km (Otto et al., 2016).

Although there exist several studies on PICs on the terrestrial planets and the Moon, there are very few investigations on PICs on other satellites and asteroids, even though surface maps of Rhea, Tethys, Dione, Ceres, and Vesta that have an appropriate resolution exist. Therefore, the aim of this study is to acquire more information about the abundance and characteristics of PICs on these bodies.

Throughout this master's thesis, for the classification of a polygonal impact crater, the definition by Öhman et al. (2003) has been used. It states that a crater is polygonal if it consists of "at least two straight rim segments and a clearly discernible angle between them" (see Fig. 1.2).

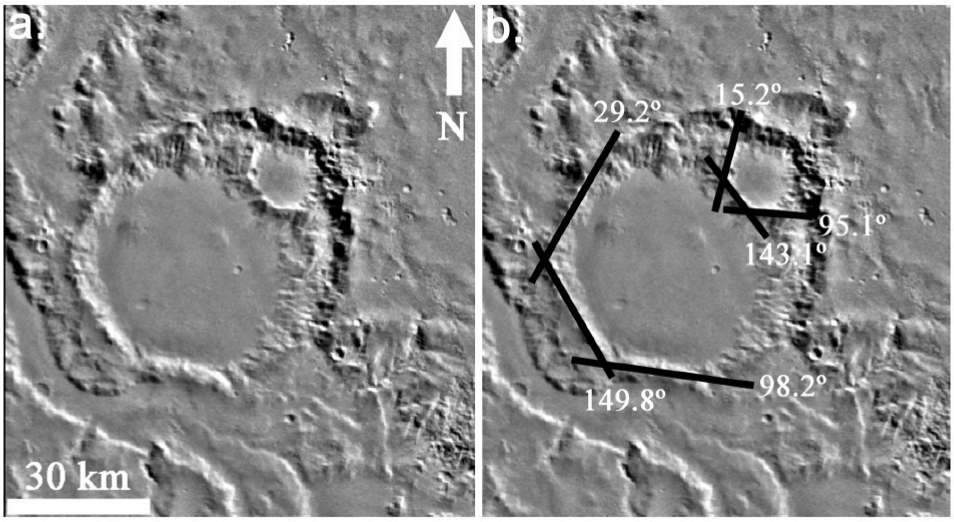

Figure 1.2: a) Polygonal impact craters (PICs) north of the Argyre basin located at 36.3°W, 30.5°S. b) Marked straight crater rim segments and the angles between them (Öhman et al., 2006). Credit: Öhman et al. (2006), p. 1166.

Therefore, only craters having neighbouring straight crater rim segments were considered as polygonal and craters with only one straight rim or several straight rims that do not comprise an angle were disregarded. If the studies of other authors that I refer to in this thesis use different definitions of polygonal impact craters, then this is mentioned explicitly.

As several studies have shown that PICs form due to weakness zones in the crust and that some straight crater rim segments are parallel to different tectonic features, these craters can provide an important tool in acquiring more information about properties of the examined object's crust, especially weakness zones, even if they are not visible (e.g. Öhman, 2009). This knowledge also leads to more information concerning fracture networks, tectonic history, material properties and the formation process itself (e.g. Watters, 2006; Öhman, 2009). Therefore, "impact craters are not merely circular holes in the ground, but highly complex geologic structures that can also aid in the interpretation of the geologic history of the surrounding regions" (Öhman (2009), p. 17).

1.2 Overview

In this master's thesis, first of all I will give an introduction about the definition of PICs and their occurrence throughout the Solar System, as well as an outline of theories regarding their formation processes. Chapter 2 will deal with previous research by other authors of polygonal impact craters on the terrestrial planets, the Moon, and other bodies of the Solar System. In chapter 3, I will describe the databases and methods I used in this study. After giving a short overview about the characteristics of the examined Saturnian satellites (Rhea, Dione, Tethys) and asteroid belt objects (Ceres, Vesta) in chapters 4 and 5, I will present my findings in chapters 6 and 7, concluding with a discussion in chapter 8 that compares my results with those found in the studies of other authors.

1.3 Formation of Polygonal Impact Craters (PICs)

Pre-impact target inhomogeneities like faults, joint sets, fractures, lithologic boundaries or weakness zones support the formation of PICs when impact occurs (e.g. Eppler et al., 1983; Aittola et al., 2010; Öhman et al., 2010). Fractures in rock can form through tension (subcrustal heating, tidal attraction), compression (heating, hydration, subcrustal cooling) and shear (impacts, tectonic forces) (Fulmer and Roberts, 1963). By studying PICs at different degradational stages and illumination angles on Mars (for further detals see chapter 2), Öhman et al. (2006) showed that neither crater degradation nor illumination geometry have an effect on the formation of these types of craters. From their studies Öhman et al. (2008) also conclude that "it appears that the most prominent clusters of PIC rim orientations emerge when two or more orientations of structural weakness coincide" (Öhman et al. (2008), p. 1623).

Concerning the exact formation mechanisms which are still unknown, different formation models have been suggested depending on the resulting impact crater. Eppler et al. (1983) state that simple craters form during the excavation stage whereas "excavation occurs preferentially in directions parallel to trends of structural weakness" (Eppler et al. (1983), p. 204). This process leads to straight crater rim segments that make an angle of about 45° with joint sets or fractures (Shoemaker, 1963). The best studied simple PIC on Earth is the quadrangular-shaped, 50 000 year old Barringer Crater in Arizona (see Fig. 1.3) which has a diameter of about 1.2 km and 50 m high rims (see Shoemaker, 1963; Roddy, 1978; Poelchau et al., 2009).

Shoemaker (1960) concluded that "regional jointing has controlled the shape of the crater, which is somewhat square in outline; the diagonals of the "square" coincide with the trend of two main sets of regional joints" (Shoemaker (1960), p. 310). After numerical simulations, Poelchau et al. (2009) state that in their model "a comparison of surface stress to the excavation force exerted on arbitrarily defined rock units parallel and at a 45° angle to orthogonal joints shows that 1.41 times less force is needed to eject rock units parallel to joint sets, suggesting a possible mechanical factor responsible for preferred ejection along the joint sets, which should result in a square-shaped crater with its diagonals parallel to the joints" (Poelchau et al. (2009), p. 14). They also mention that "the effect of target heterogeneity on the crater shape increases with time and progressing crater excavation, while the effect of obliquity decreases with time" (Poelchau et al. (2009), p. 14).

Eppler et al. (1983) also suggest a formation model for complex craters which states that they form in the modification stage in which "walls fail and slumps develop along trends of structural weakness" (Eppler et al. (1983), p. 204), resulting in straight crater rim segments that are parallel to weakness zones. The transition between simple and complex impact craters on Earth takes place at a diameter of about 3 to 5 km (Melosh and Ivanov, 1999). An example of a hexagonal, complex PIC on Earth is

Figure 1.3: Barringer Crater in Arizona which is a simple PIC having a diameter of about 1.1 km and an age of about 50 000 years (NASA, 2004) (see Shoemaker, 1963; Roddy, 1978; Poelchau et al., 2009). Credit: U.S. Geological Survey.

the eroded Söderfjärden crater in western Finland which has a diameter of about 6.6 km (see Abels, 2003; Raitala, 1985).

Hexagonal and pentagonal PICs were produced in basalt by high-explosive cratering studies in the Nevada test site, but unfortunately there are no studies of the joint system where the experiment took place prior to the cratering studies (Fulmer and Roberts, 1963).
Gault et al. (1974) performed cratering experiments at the NASA Ames Vertical Gun Range into jointed targets leading to square-shaped and also hexagonal polygonal impact craters although there were only two perpendicular joint sets. Öhman (2009) mentioned that "unfortunately Gault et al. (1968) did not specify the relationships between the joint sets and the straight rim segment strikes of the small hexagonal impact crater that resulted from their experiment" (Öhman (2009), p. 107).
Fulmer and Roberts (1963) concluded from explosion cratering experiments that joints are parallel to the PIC rims and their diagonals and that circular craters form in a loose, soft, or unconsolidated medium. They also found that PICs only form if a dominant joint system is present where fractures are neither too widely spaced nor very complex (Fulmer and Roberts, 1963).

Öhman et al. (2008) studied both simple and complex impact craters on Mars but did not find a difference concerning their orientation of straight crater rim segments. Therefore, they proposed an additional PIC formation model (see Fig. 1.4) that could be applied to both crater types proposing that "the shape of at least simple and relatively small complex polygonal craters can originate from thrusting along pre-existing target structures" (Öhman et al. (2008), p. 1622) during the excavation stage, arguing that thrusting also occurs in simple crater rims and was observed in cratering experiments, which supports their additional PIC formation model. Öhman et al. (2008) also suggest that the formation model proposed by Eppler et al. (1983) and their model could happen at the same time and that "the typical partial hexagon shape of PICs probably originates from thrusting or slumping along orientations with an angle of about 120° between the fractures. Fracture sets with an angle of about 120° are commonly formed in conjugate shear fracturing" (Öhman et al. (2008), p. 1622). Concerning the question why some parts of the crater rims of PICs are straight and some are circular, Öhman et al. (2008) suggest that the space between the fractures is not adequate or that there are no dominant structural trends.

Another factor that is important concerning the formation of PICs is the size of the crater. Aittola et al. (2007) conclude that "smaller crater size favours the formation of them, but otherwise PICs show characteristics similar to the other craters. The reason for this diameter-dependence could be related for example to the thickness of the elastic lithosphere, the depth or the spacing of the tectonic structures as well as the destructive effect of the large impact event itself. It is also quite possible that there is a specific size range with respect to the simple-complex transition diameter that favours the formation of polygonality." Additionally, Öhman found that PICs on Venus favour a size range of 3-4 $\times$ D_{tr}, on Mars 2-5 $\times$ D_{tr} and on the Moon 1.3-3 $\times$ D_{tr}. The transition diameter D_{tr} between simple bowl-shaped and complex impact craters that show terraced rims and central structures depends on the surface gravity and the target material (Bland, 2013) (see Fig. 1.5). "In general, the transition occurs at smaller crater diameters for higher surface gravities and rocky (as opposed to icy) bodies" (Bland (2013), p. 512).

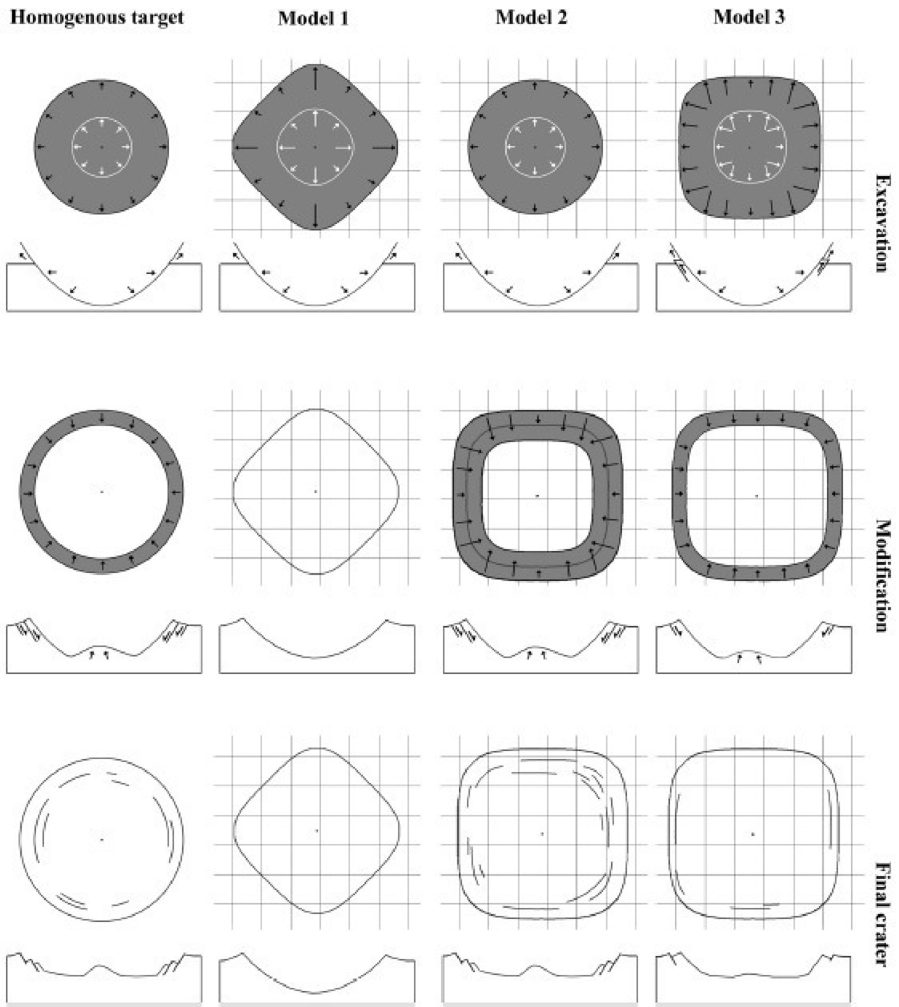

Figure 1.4: Formation of circular impact craters and polygonal impact craters in the three different stages of crater formation showing plan views and profiles. Models 1 and 2 were proposed by Eppler et al. (1983), and the resulting PICs are simple and complex, respectively. Model 3 was proposed by Öhman (2009). Note that "the excavation stage of large complex craters (model 2) may be structurally controlled according either to model 1 or model 3, but the structurally controlled slumping in the modification stage overshadows this. Simple craters (model 1 and 3) and small complex craters (model 3) do not slump significantly, and thus the polygonal morphology obtained at the excavation stage prevails" (Öhman et al. (2008), p. 1623). Credit: Öhman (2009), p. 163.

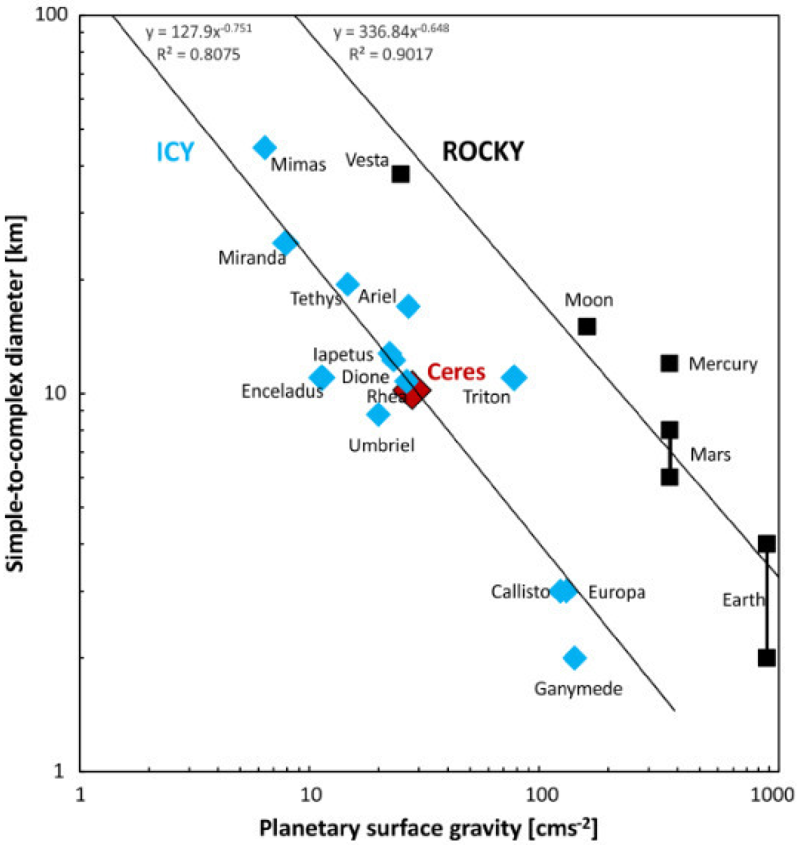

Figure 1.5: Simple-to-complex transition diameters of different objects of the Solar System. Credit: Platz et al. (2016).

2 Previous studies on Polygonal Impact Craters (PICs)

Polygonal impact craters were first known on the Moon around 1800 and the first studies on them were conducted in the 1960s and 1970s (Öhman, 2009). Then, for a long time, no research concerning them was done and the most recent examinations on PICs have taken place since 2000. Most of the recent studies focus on Venus and Mars but PICs on the Moon, Mercury, Ceres, and Dione have also been considered. To date, there have been no detailed studies on PICs on other objects and they have only been mentioned casually, if at all, by some authors.

2.1 PICs on Mercury

Wood et al. (1977) examined 537 craters on Mercury with diameters greater than 30 km found in the Brown University Mercury Crater Library (Cintala et al., 1976), classifying these based on their morphology from class 1 (fresh, sharp rims) to class 5 (most degraded) and comparing them with the data of 1474 lunar craters. Of class 1, 16% of craters were considered to have "quasipolygonal (13%) or strongly polygonal (3%) rims with polygonal features decreasing to about 3% for class 5 craters" (Wood et al. (1997), p. 3508). Polygonal crater outlines are not as well developed as on the Moon and the authors mention that they did not recognize any correlations between the orientations of the straight rims of polygonal impact craters and tectonic features (Wood et al., 1977).

Melosh and Dzurisin (1978) investigated the global tectonics on Mercury, making a map of linear scarps, ridges and troughs, including "linear segments of crater rims with distinctly polygonal outlines in plan view, since crater polygonalization presumably reflects structural control by preexisting lithospheric fractures" (Melosh and Dzurisin (1978), p. 229). Due to the fact that old craters exist that are polygonal, the authors conclude that linear lithospheric fractures must have existed before the heavy bombardment (Melosh and Dzurisin, 1978).

Strom et al. (1990) conducted a geological mapping of the Bach quadrangle using images from the Mariner 10 mission, having a maximal resolution of 0.5 km per pixel, defining five different crater ages from fresh to heavily degraded and examining craters larger than 15 km in diameter. By studying this 1 570 000 km^2 large area, they mention the existence of polygonal crater walls, stating that "joint-controlled mass movements are most likely responsible for the polygonal crater-wall segments; segments as long as 100 km suggest that these fractures extend deep into the lithosphere. The most conspicuous trends of these lineaments are east-west, N.50°W., and N.40°E." (Strom et al. (1990), p. 10). The authors also mention that there are old craters with polygonal shapes (e.g. Cervantes) and conclude that structural lineaments exist that are older than the oldest craters classified (Strom et al., 1990).

Further studies on PICs on Mercury have been conducted by Weihs et al. (2015) who analysed 291 impact craters with diameters greater than 12 km, using the IAU/NASA/USGS Planetary Database and images with a resolution of 0.5 km/pixel from Mariner 10 and Messenger. They found 33 PICs all of which are complex craters, having terraced rims. Figure 2.6 shows an example of a PIC on Mercury - Crater Saikaku (left). The three crater rims were marked and the angles between the straight segments were measured (right) (Weihs, 2012). Crater Saikaku has a diameter of 64 km and is located at a latitude of 71.96° and a longitude of 177.97° (IAU, 2017).

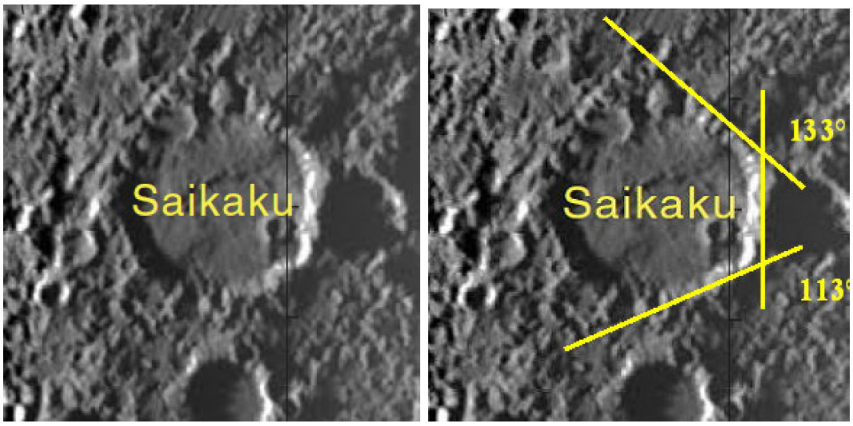

Figure 2.6: Crater Saikaku on Mercury (left) with (marked) three straight crater rim segments (right) and measured angles between the segments yielding 133° and 113° (Weihs (2012), p. 23). The crater has a diameter of 64 km, a latitude of 71.96° and a longitude of 177.97° (IAU, 2017). Credit: Weihs (2012), p. 23.

The mean number of straight crater rim segments is 2.5 (calculated by the author, based on results from Weihs (2012), see Fig. 2.7) and the angles between the straight rims vary between 98° and 132°, yielding a mean angle of 112° (Weihs, 2012).

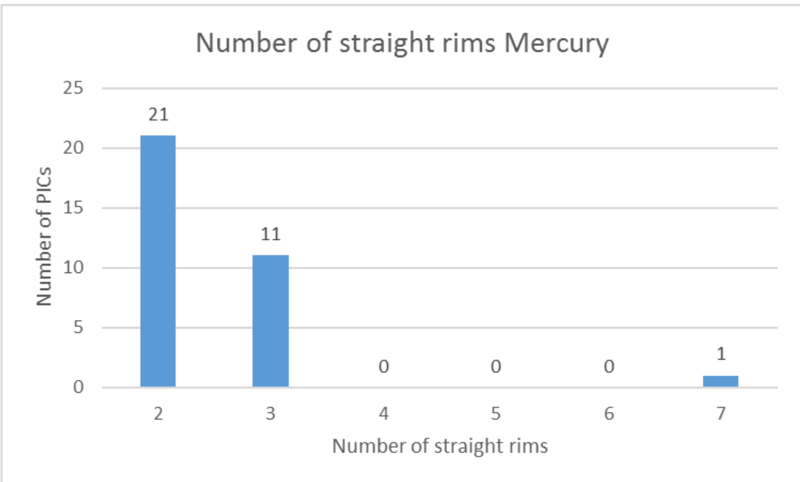

Figure 2.7: Number of straight crater rim segments as a function of the number of PICs on Mercury. Values taken from Weihs (2012). There are twenty-one craters that have two straight rim segments, eleven have three straight segments, and only one crater has seven straight crater rims (Weihs, 2012).

The diameters of the non-polygonal impact craters on Mercury range from 20 km to 720 km while the diameters of PICs range only from 65 km to 240 km, indicating that PICs seem to favour small to mid-sized diameters (Weihs et al., 2015) (see Fig. 2.8).

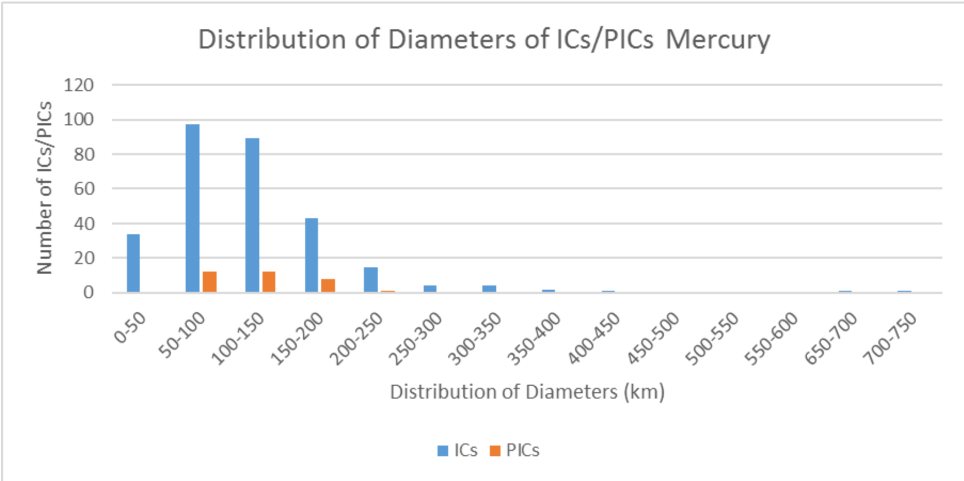

Figure 2.8: Number of non-polygonal impact craters (ICs) and polygonal impact craters (PICs) as a function of their diameters (km). The blue bars represent the number of ICs while the orange bars show the number of PICs. The diameters of ICs are between 20 and 720 km while the diameters of PICs only range from 65 km to 120 km (Weihs et al., 2015). Credit: Weihs et al. (2015), p. 81 (modified by the author).

No striking distribution pattern was found, the distribution of PICs seems to be roughly proportional to the number of impact craters (Weihs et al., 2015) (see Fig. 2.9).

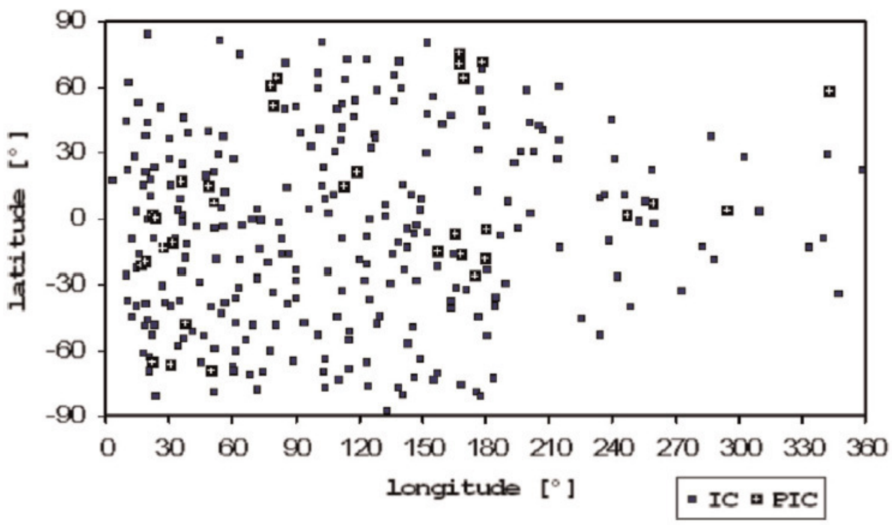

Figure 2.9: Distribution of non-polygonal impact craters (IC) and polygonal impact craters (PIC) on the surface of Mercury. The small boxes represent the non-polygonal impact craters (IC) while the large boxes show the polygonal ones (PIC). Credit: Weihs et al. (2015), p. 80.

2.2 PICs on Venus

Prior to the studies of polygonal impact craters on Venus by Aittola et al. (2007) and other authors, the only person to have mentioned the occurrence of PICs on this planet was Herrick et al. (1997) who made a database of Venusian craters and classified twelve of them as PICs.

There were no more studies until 2007 when Aittola et al. (2007) studied the abundance, distribution, and possible correlations between the orientations of straight crater rim segments of PICs with a diameter larger than 12 km and the existence of tectonic features. They made use of Magellan SAR images having a resolution of 75 m/pixel and image data having a resolution of 225 m/pixel for areas that are not covered by SAR (Aittola et al., 2007). Using the catalogue from Herrick et al. (1997), Aittola et al. (2010) found 121 PICs among 550 craters greater than 12 km in diameter which is about 22%. All of the PICs they found are complex due to the dense atmosphere which prevents the formation of craters having diameters less than 2 km (Herrick and Phillips, 1994; Basilevsky and Head, 2003). Figure 2.10 shows an example of a PIC on Venus, Behn crater, having four straight rim segments (Aittola et al., 2007).

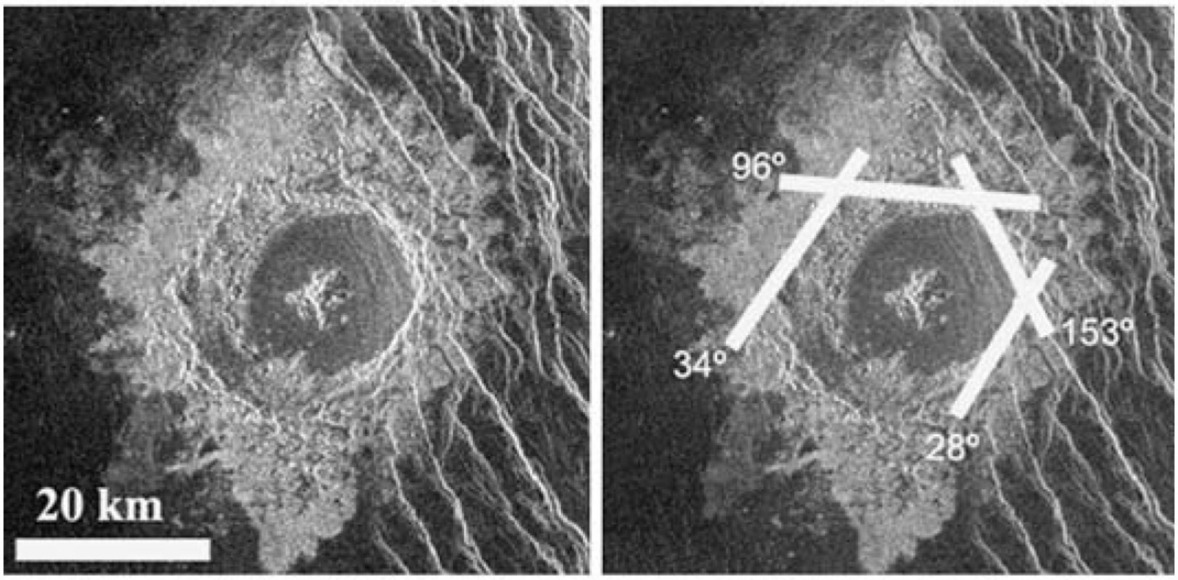

Figure 2.10: Example of a polygonal impact crater (PIC) on Venus. The Behn crater (32.5 S/142 E) has four straight rim segments (Aittola et al., 2007). Credit: Aittola et al. (2007), p. 44.

The PICs they found seem to be distributed randomly over the surface as non-polygonal craters do on Venus (see Fig. 2.11), whereas rift zones, tessera terrain, or lowland plains show no correlation with the distribution of PICs (Aittola et al., 2007; Kukkonen et al., 2015). There is also no correlation between the existence of polygonality and the degradation state, floor reflectance, parabolic features around the crater, or crater age (Aittola et al., 2007).
While 53% of all PICs are less than 20 km in diameter, only 35% of non-polygonal craters lie in this size range and there is a lack of PICs having diameters greater than 50 km, concluding that PICs seem to favour small crater sizes (Aittola et al., 2007) (see Fig. 2.12).

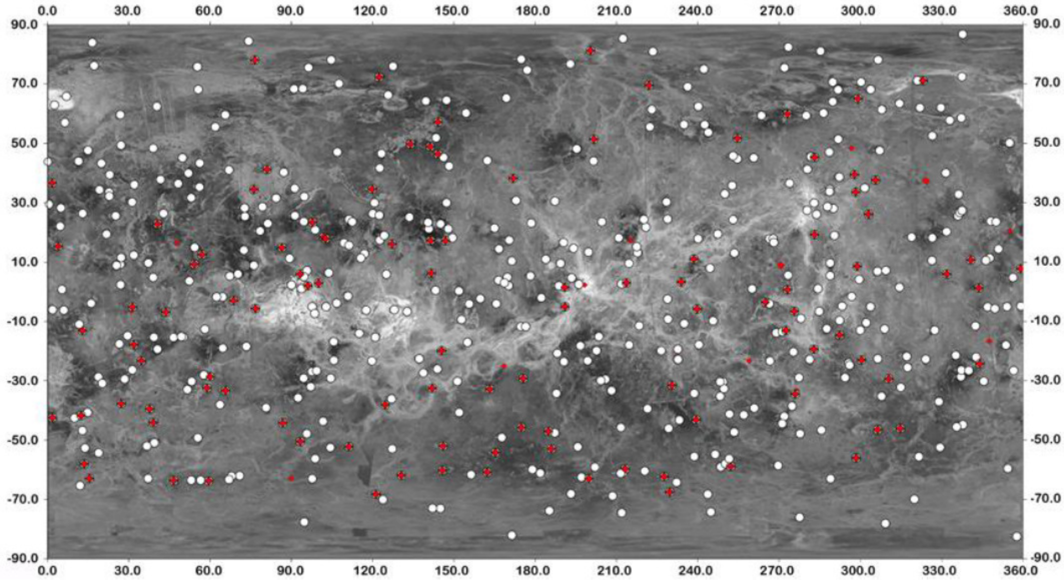

Figure 2.11: The distribution of non-polygonal impact craters (white) and polygonal impact craters (red), greater than 12 km in diameter plotted on Magellan data shows a regular distribution (Kukkonen et al., 2015). Credit: Kukkonen et al. (2015).

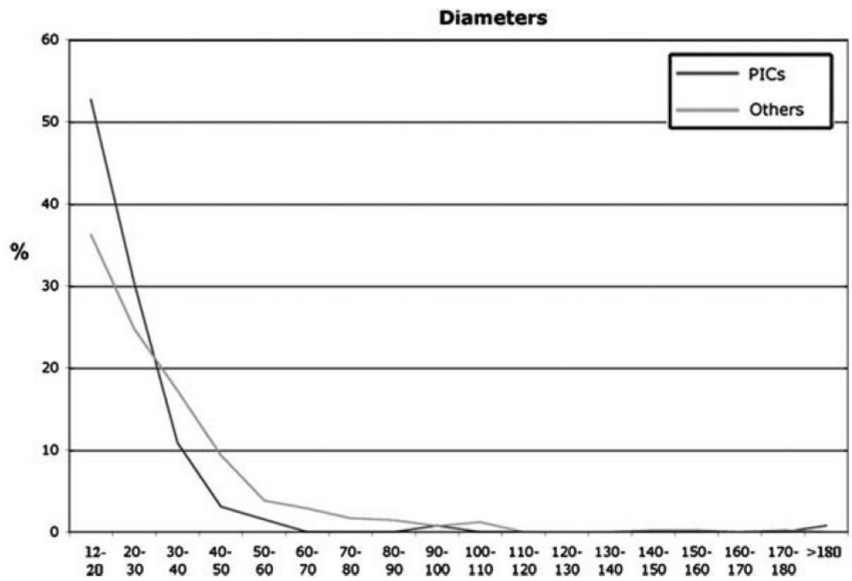

Figure 2.12: Diameters (km) of polygonal impact craters (PICs) in comparison to non-polygonal impact craters on Venus show that PICs seem to favour small to medium-sized crater diameters (Aittola et al., 2007). Credit: Aittola et al. (2007), p. 48.

The only difference concerning the morphological classes between PICs and non-polygonal impact craters is the fewer number of PICs that have peak rings or multiple peaks, an obvious fact in that most of the PICs have small diameters and only large craters show these characteristics (Aittola et al., 2007).

Aittola et al. (2010) carried out further studies concerning possible correlations between the straight crater rim segments of PICs and tectonic features, stating that "straight rim segments are often parallel to the orientations of the surrounding tectonic structures, particularly those in tessera terrain and young rift zones, as well as the concentric components of coronae" (Aittola et al. (2010), p. 356) (see Fig. 2.13). The correlation is much better if the tectonic feature is close to the crater (Aittola et al., 2010). 75% of PICs show a straight crater rim segment parallel (+/-7°) to the annulus of the corona if the distance between the corona and the PIC lies within two crater diameters and 43% of PICs show such a correlation if the distance is within two to ten crater diameters (Aittola et al., 2010). Aittola et al. (2010) conclude that "straight crater rims are actually indications of the concentric deformation and stresses caused by corona formation process. If this is the case, the PIC may reveal how far the crustal deformation caused by the corona formation extends" (Aittola et al. (2010), p. 361).

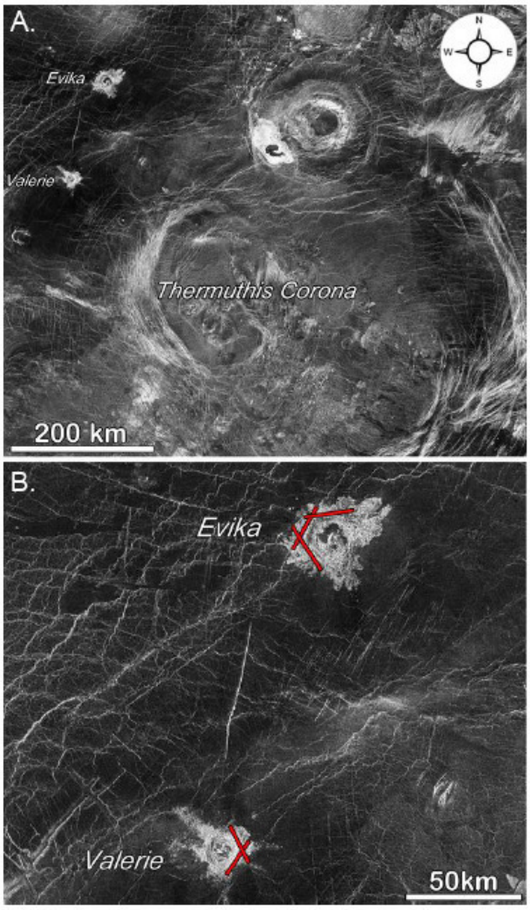

Figure 2.13: A) PICs Valerie and Evika near Thermuthis Corona. Valerie is located at 6.4°S, 30.9°E and has a diameter of about 13.6 km (Kukkonen et al., 2015). Evika (5.1°S, 31.430.9°E) has a diameter of about 20.3 km (Kukkonen et al., 2015). B) Image showing the straight rim segment of Valerie which is parallel to the radial component of the corona and the straight rim segment of Evika which is parallel to the concentric component of Thermuthis (Kukkonen et al., 2005). Credit: Kukkonen et al. (2015).

However, for about 18% of PICs no correlation with any tectonic features was found (Aittola et al., 2010). Therefore, Kukkonen et al. (2014) conclude that only large coronae can cause crustal weakness that might lead to the existence of PICs because the studied coronae that have positive correlations have large diameters.

Weihs et al. (2014) chose 22 PICs having more than 30 km in diameter and determined the relative age of these PICs using criteria by Basilevsky and Head (2006), yielding about 0.3 T to 0.6 T where T is the age of Venus' surface which is about 500 to 700 Myrs. Figure 2.14 shows the mean relative ages of different geological units and PICs on Venus (Weihs et al., 2014). No age differences between PICs and non-polygonal impact craters were found on Venus (Weihs et al., 2014).

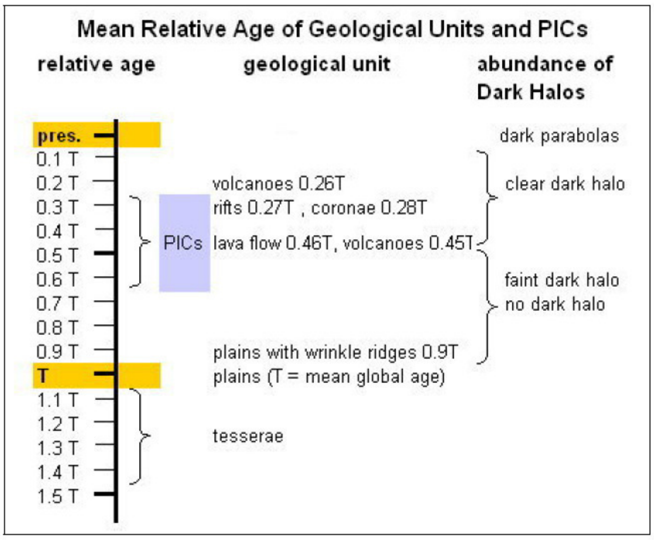

Figure 2.14: Mean relative age of different geological units (volcanoes, rifts, coronae, lava flows, plains with wrinkle ridges, plains, tesserae) on Venus together with the abundance of dark haloes (Weihs et al., 2014). T is the mean global age which is about 500 to 750 Myr (Weihs et al., 2014). Credit: Weihs et al. (2014).

2.3 PICs on the Moon

The first mention of polygonal craters on the Moon probably dates back to Lamech (1934) who wrote about craters and mare, having polygonal shapes (Fielder, 1961). Lamech (1934) noted craters whose "walls are, in general, oriented in preferential directions characteristic of the region in which they are situated" (Fielder (1961), p. 217, and references therein).

Quaide et al. (1965) studied 169 fresh impact craters on the Moon and noted that craters having diameters greater than 20 km are more often polygonal compared to smaller ones and that most of the polygonal craters are terraced.

Ronca and Salisbury (1966) measured the circularity of 86 lunar craters greater than 25 km in diameter and distinguished between two populations of craters: those that are more circular and those that are less so. They also discuss different hypotheses that could explain why these two different crater populations exist, for example the angle and velocity of the projectile and the target material, concluding that it is most probable that “subcircular craters were formed during a period of stress in the lunar crust” (Ronca and Salisbury (1966), p. 130). Additionally, they found that non-circular craters are older than the maria (Ronca and Salisbury, 1966).

Further studies on circularity and crater types were conducted by Adler and Salisbury (1969) who examined 487 craters, concluding that there is a relationship between these craters, fractures, and the formation of mare. They classified craters into five different classes according to their rim sharpness or completeness where class 1 craters have the sharpest rims (Adler and Salisbury, 1969). Most craters belonging to class 1 were found to be circular while those of higher classes were subcircular and young craters were found to be more circular than older ones (Adler and Salisbury, 1969). Also, craters having peaks are more circular than craters that lack this feature (Adler and Salisbury, 1969). Their conclusion is that “Our finding that subcircular craters are produced preferentially around the circular maria, suggests that most of them are genetically related to the fracture system and local stress history associated with mare formation” (Adler and Salisbury (1969), p. 52).

Pohn and Offield (1970) studied lunar crater morphology using Orbiter IV photographs with a resolution of 70 to 100 metres and examined more than 1000 lunar craters. They differentiated craters into three size classes: Class I craters are greater than 45 km in diameter, class II craters are between 20 to 45 km in diameter, and class III craters are from 8 to 20 km in diameter. They then divided these into age classes from 0.0 (oldest) to 7.0 (youngest) (Pohn and Offield, 1970), mentioning that “class I craters are generally circular when formed and become slightly to markedly polygonal after age 4.0, depending on influences such as local fracture pattern and superposed cratering events. Class II craters form with polygonal outlines and remain obviously polygonal throughout all stages of modification. Class III craters form with circular outline; polygonality develops by age 4.5 and reaches a maximum at age 2.5” (Pohn and Offield (1970), p. 155). Pohn and Offield (1970) described the rim crest, walls and rims of several impact craters and considered Kepler, Timocharis, Horrocks, Nöggerath, Manzinus, Sacrobosco, Regiomontanus, Baco E, Rosenberger A, and Baco J as being polygonal (Pohn and Offield, 1970) (see Fig. 2.15).

Wood et al. (1977) compared morphological characteristics of 537 craters on Mercury that have diameters greater than 30 km to 1474 lunar craters but only mentioned that there is no data concerning the polygonality of lunar craters, so that they could not make a comparison to the values they yielded for the examined craters on Mercury (Wood et al., 1977).

Pike (1977) studied 200 lunar craters from images of the Apollo 15-17 missions that have diameters from 0.4 km to 370 km, pointing out that “circularity is not constant with crater size but attains a maximum at a rim diameter of 10 km or so” (Pike (1977), p. 497). No difference between fresh craters on the upland and fresh mare craters was found (Pike, 1977).

Eppler et al. (1977) used Fourier analysis to study the shape of 247 craters on the near side of the Moon greater than 18 km in diameter, using 1:100 000 lunar maps from the USGS, concluding that “Mare craters are more circular than highland craters, probably as a reflection of the relative structural and lithologic simplicity of thick flood basalt filling mare basins as compared with more complex

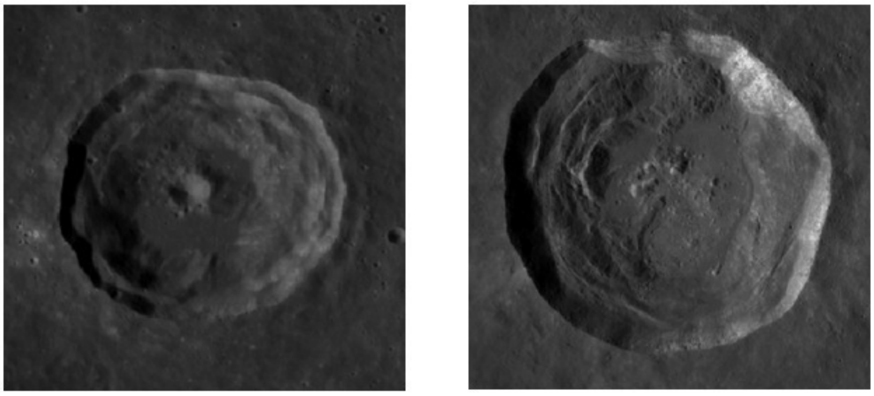

Figure 2.15: Left: Polygonal impact crater Kepler on the Moon having a diameter of 29.49 km located at a latitude of 8.12° and a longitude of -38.01°. Credit: IAU/NASA/USGS Planetary Database (2016). Right: Polygonal impact crater Timocharis on the Moon having a diameter of 34.14 km located at a latitude of 26.72° and a longitude of -13.1°. Credit: IAU/NASA/USGS Planetary Database (2016).

geologic relationships that exist in highland regions" (Eppler et al. (1977), p. 511). Also, younger and larger craters are more circular than older, smaller craters (Eppler et al., 1977). The authors think too that "It is conceivable that impact events in highly faulted terrain will excavate craters that display elongation in a direction parallel to regional faulting" (Eppler et al. (1977), p. 519-520).

Öhman et al. (2010) studied impact craters greater than 10 km in diameter on the near side of the Moon (10°N-50°S, 10°W-40°E) in an area of about 960-1490 km $\times$ 1820 km (see Fig. 2.16), using images from the Consolidate Lunar Atlas. They found 160 named and 7 unnamed PICs and 656 non-polygonal impact craters without any significant concentration of PICs (Öhman et al., 2010). The highest density is in the Werner-Airy basin (Öhman et al., 2010). The diameters of PICs range from 11 km to 199 km, in which "the relative abundance of polygonal impact craters drops rapidly for diameters below $\sim$20 km, whereas the relative abundance of the nonpolygonal craters increases with decreasing size" (Öhman et al. (2010), p. 60), as can be seen in Figure 2.17. Small complex craters are more frequently polygonal than simple craters are (Öhman et al., 2010).

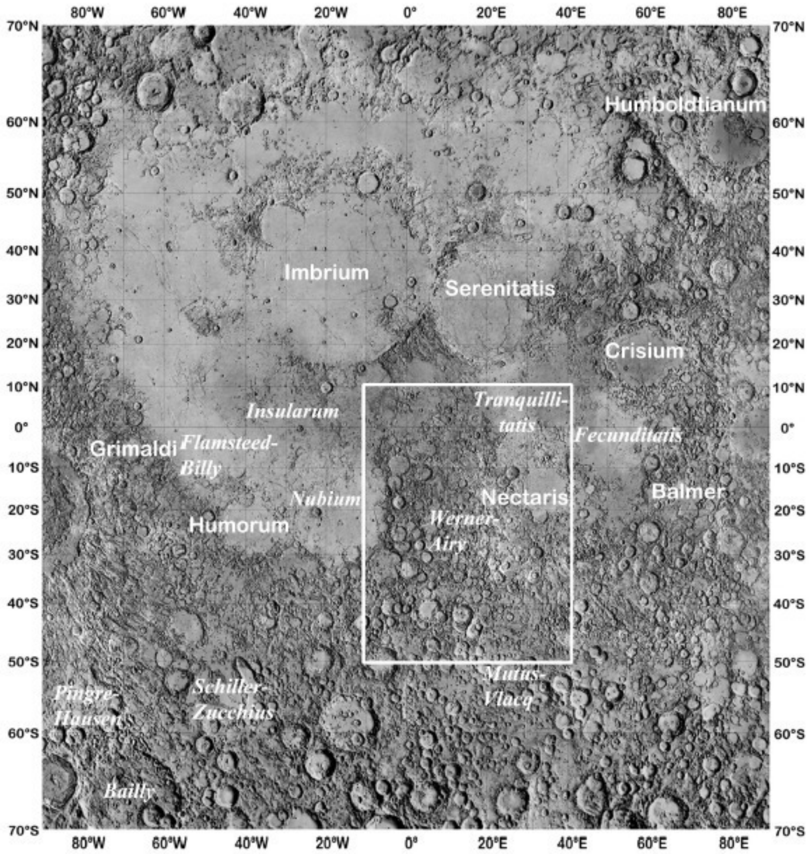

Figure 2.16: Study region (white box) of polygonal impact craters on the near side of the Moon, located at 10°W-40°E, 10°N-50°S (Öhman, 2009). Credit: Öhman (2009), p. 116.

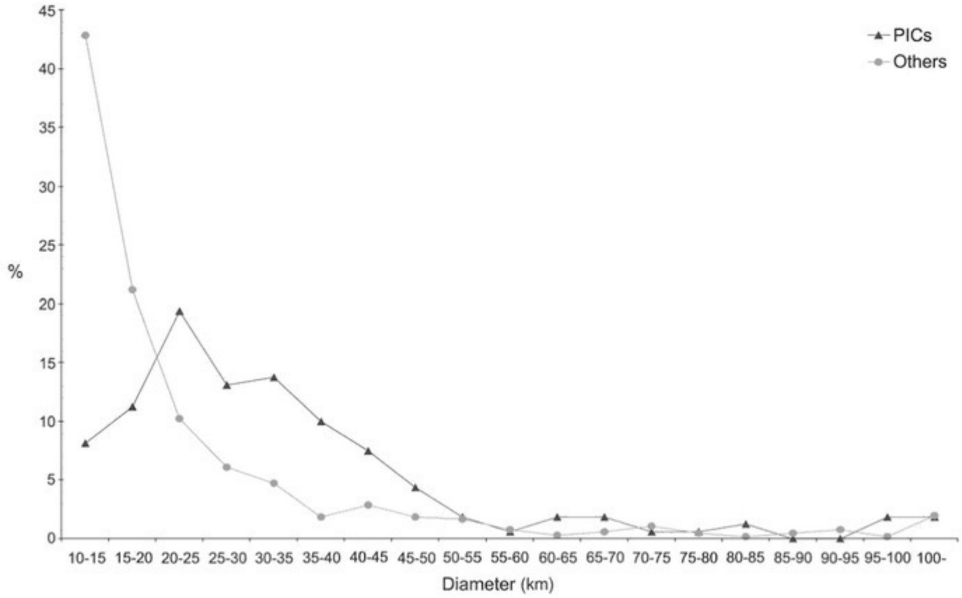

Figure 2.17: Diameters of polygonal impact craters (PICs) and non-polygonal impact craters (others) in the study region of the Moon. Credit: Öhman et al. (2010), p. 60.

2.4 PICs on Mars

Pike (1971) studied depths and diameters of 41 craters on Mars which had diameters between 6 km and 36 km, using Mariner IV images, stating that "Most smaller craters are simple in shape, resembling freshly formed terrestrial impact, explosive, and meteorite craters; craters over 10-15 km diameter are much more complex and tend to have subdued rims, polygonal outlines, flat floors, central peaks, irregular rim crests, and rim-slope terraces" (Pike (1971), p. 385-386).

PICs on Mars were studied in the greater Hellas region and in the Argyre region by Öhman et al. (2010); Öhman (2009); Öhman et al. (2008); Öhman et al. (2006) and Öhman et al. (2003). Valles Marineris is located north-northwest of the study regions (see Fig. 2.18).

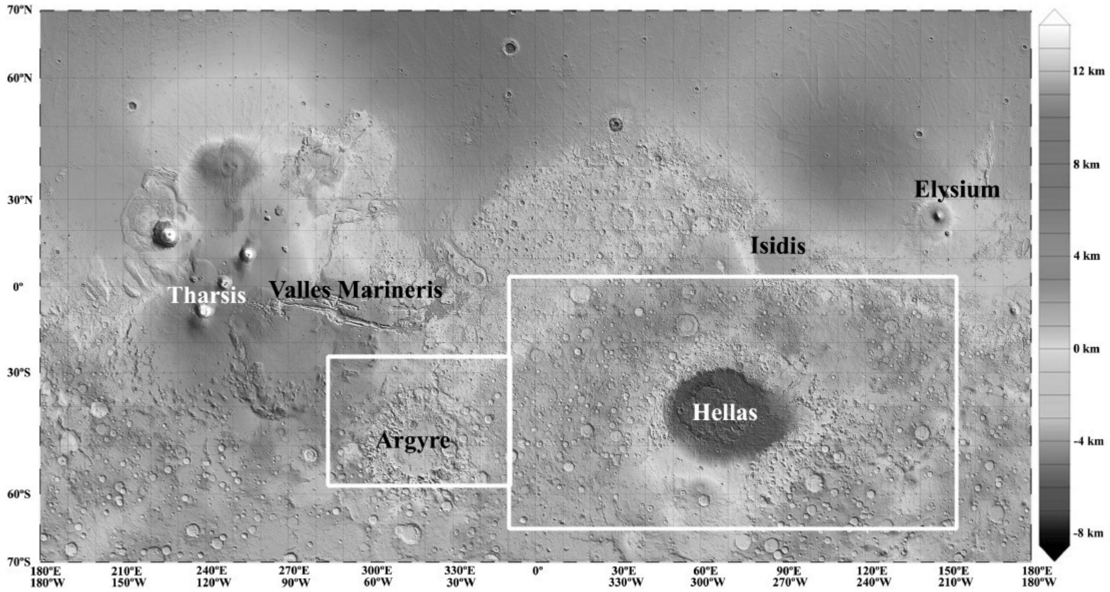

Figure 2.18: Study regions of PICs on Mars (white boxes). Valles Marineris is located north-northwest of these regions. Credit: Öhman (2009), p. 45.

For the greater Hellas region, Viking Orbiter Mars Digital Image Mosaics were used which have a resolution of 0.231 km per pixel at the equator to study the distribution of PICs and the orientation of their straight rim segments (Öhman et al., 2006).
In total, Öhman et al. (2006) found 269 PICs in the Argyre region which comprises about 17% of the total crater population greater than 7 km in diameter. In this region they measured 820 straight rims. In the greater Hellas region 1306 PICs were found (Öhman, 2009). Figure 2.19 shows two examples of polygonal impact craters on Mars (Öhman et al. 2006).
The authors state that the "vast majority of polygonal craters in the greater Hellas region are, or have a tendency towards being hexagonal (...) pentagons occur relatively often, but clearly square-shaped craters tend to be rare" and that "polygonal impact craters are most common in the northern part of the study area close to the Isidis impact basin" (Öhman et al., 2003). Also, a correlation between straight rim orientation and the Hellas and Isidis basins was found (Öhman et al., 2006).
Öhman et al. (2006) examined whether different lighting conditions could have an effect on the

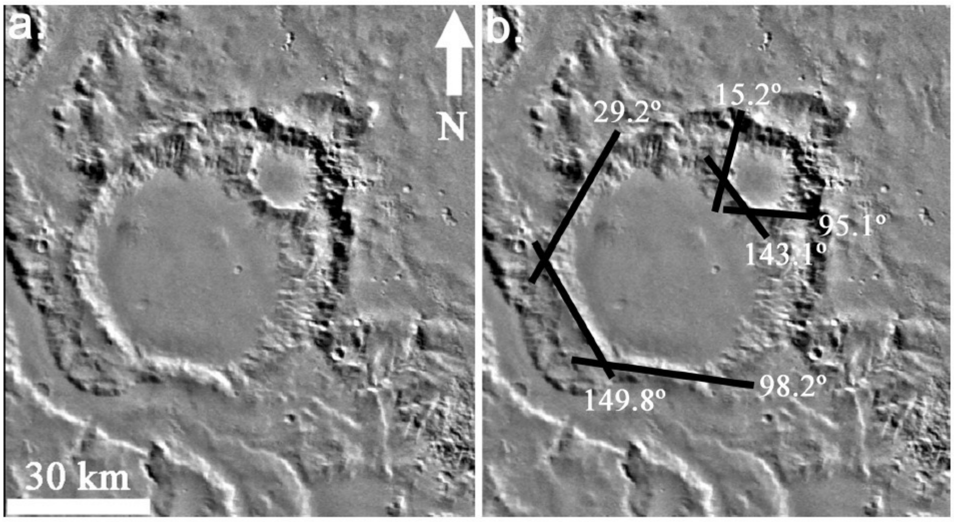

Figure 2.19: a) Polygonal impact craters (PICs) north of the Argyre basin located at 36.3°W and 30.5°S (Öhman et al., 2006). b) Straight rim segments and the angles between them. "The smaller crater's rims parallel those of the larger one's, despite the fact that the larger crater's impact should have destroyed any preexisting fracture patterns. A possible explanation is that the regional fracture pattern is quite deep-seated and has been reactivated after the formation of the larger crater, thus affecting also the shallower depths and therefore the formation of the smaller crater" (Öhman et al. (2006), p. 1166). Credit: Öhman et al. (2006), p. 1166.

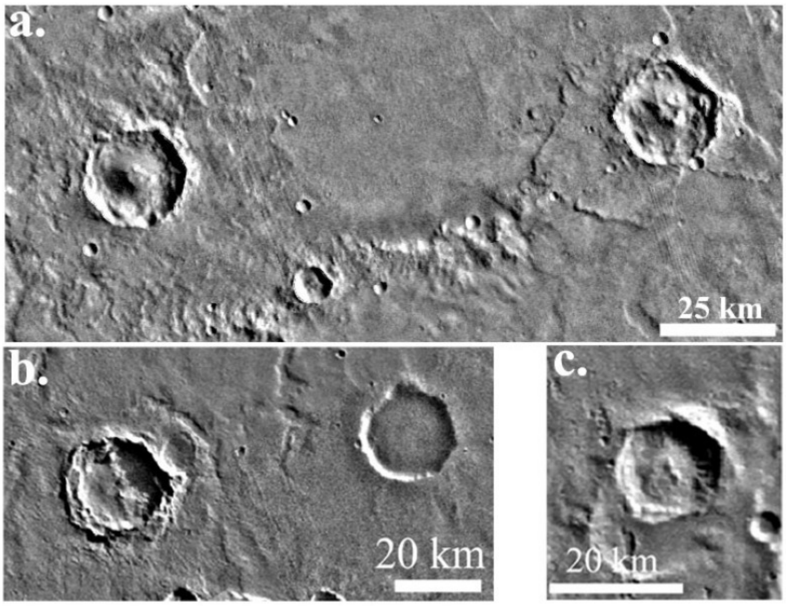

Figure 2.20: a) Three polygonal impact craters (PICs) located north of the Hellas basin at 2.8°S 298°W. b) Fresh complex PIC (left) and degraded complex PIC (right), both being nearly hexagonal, located at about 29.5°S 22.5°W in the Argyre region, Mars. c) Polygonal impact crater (PIC) northeast from the Argyre basin. Credit: Öhman (2009), p. 95.

classification whether a crater was polygonal or not and they studied PICs on two data sets which had different illumination geometries. They found no differences and also no correlation between the degradation stage of the craters and the number of straight crater rim segments, concluding that higher degraded craters are not more polygonal than younger ones and that PICs are common at all degradation stages (Öhman et al., 2006) (see Fig. 2.20).
On Mars, the transition from simple to complex crater morphologies occurs at a diameter of about 7 km (Pike, 1980; Garvin et al., 2003). Öhman et al. (2008) found no difference in the orientation of simple and complex crater rim segments.
The percentage of PICs is higher in older geological units than in younger ones (Öhman et al., 2008). Also, a correlation between the orientation of straight crater rim segments and the nearby Argyre and Ladon impact basins was found (Öhman et al., 2008).

Additionally, the striking effect of crater diameter and polygonality could be confirmed for Mars. "In the size range of 20-25 km (...) there are about 15% of all PICs (...) but only about 8% of other craters" (Öhman et al. (2008), p. 1613) (see Fig. 2.21).

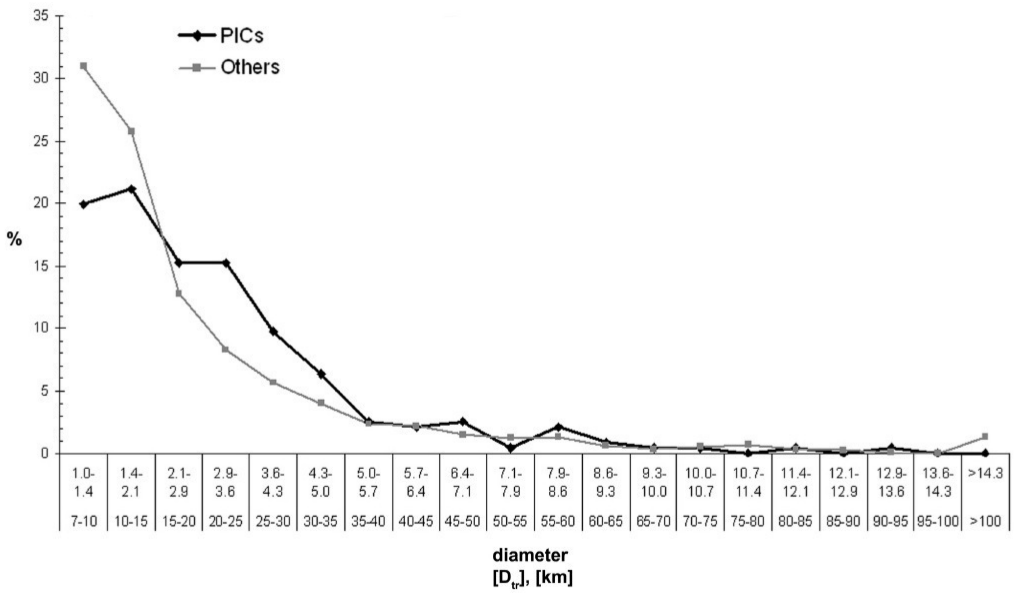

Figure 2.21: Distribution of diameters of polygonal impact craters (PICs) and non-polygonal impact craters (Others) in the Argyre region of Mars. The upper size range on the x-axis refers to multiples of the simple-to-complex transition diameter which is about 7 km on Mars, whereas the lower size range corresponds to the diameter of the crater in kilometres (Öhman et al., 2008). Credit: Öhman et al. (2008), p. 1614.

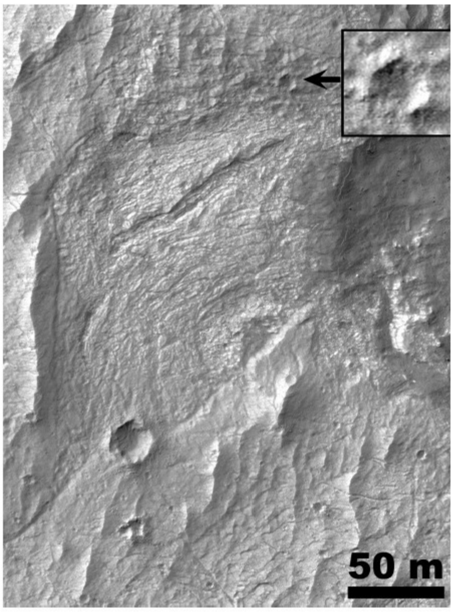

Figure 2.22: Straight crater rim segments of polygonal impact craters (PICs) from the Ius Chasma (7.7°S, 80.5°W), part of Valles Marineris, are parallel to SW-NE-orientated fractures (Öhman et al. (2008), p. 1624). Credit: Öhman et al. (2008), p. 1624.

2.5 PICs on other Solar System bodies

PICs on Ceres

Platz et al. (2015) describe complex craters on Ceres mentioning that "crater rims vary in shape from circular/elliptical to rectangular and penta-/hexagonal or in some cases developed a combination of semi-circular and angular (plane view) outline" (Platz et al., 2015).

Otto et al. (2016) studied images from the Framing Camera of the Dawn mission which had a resolution of up to 35 m/pixel, finding 258 polygonal craters with diameters between 5 km and 280 km. Most of these were 10 to 50 km in diameter, resulting in a mean diameter of 21 km (Otto et al., 2016) (see Fig. 2.23). The northern latitudes have a slightly higher polygonal crater density than the southern latitudes which could be down to the advanced relaxation of craters in this area due to higher temperatures and the existence of larger craters in the southern regions, which could have destroyed preexisting crustal structures (Otto et al., 2016).

Most of the polygonal impact craters have six or seven straight rim sections, where a decreasing crater size leads to fewer edges (Otto et al., 2016) (see Fig. 2.24).
One explanation of this phenomena, according to Otto et al. (2016), could be that the impactor creating the small polygonal impact crater has less energy, so that the straight rim sections are formed during the excavation stage and possibly lead to fewer straight rim sections compared to polygonal impact craters that are formed during the modification stage. Concerning the orientation of the straight rim segments, Otto et al. (2016) state the following: "Straight rim sections and edges of polygonal

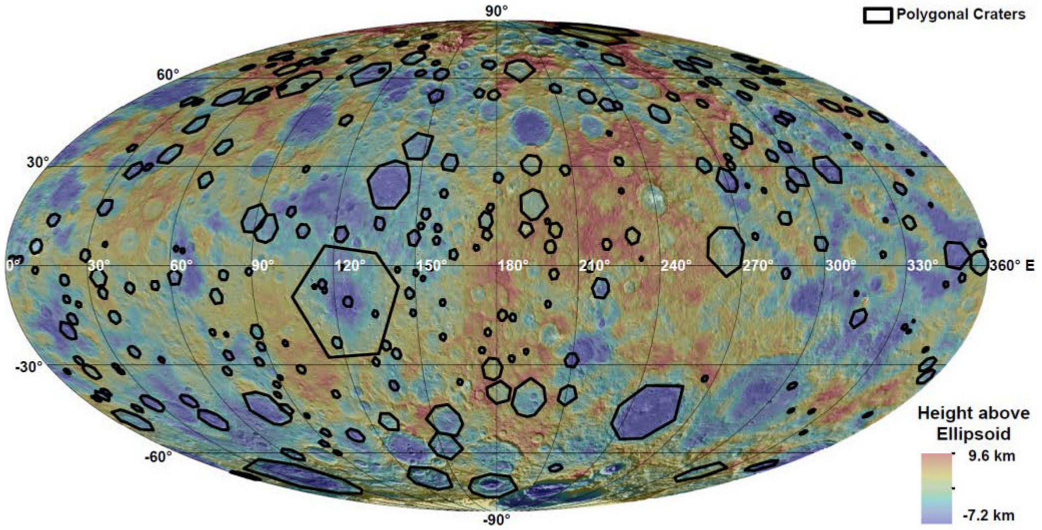

Figure 2.23: Map of Ceres showing polygonal impact craters (PICs) on its surface (Otto et al., 2016). Credit: Otto et al. (2016).

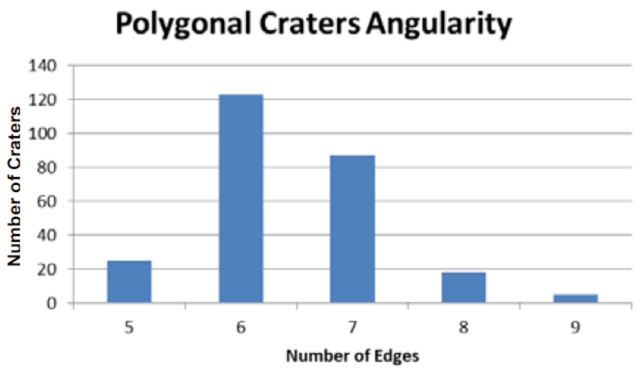

Figure 2.24: Number of edges of the 258 polygonal impact craters (PICs) found on Ceres (Otto et al., 2016). Credit: Otto et al. (2016).

craters often align with linear features associated with Ceres' tectonics. Small and medium-sized polygonal crater rims tend to align with the general direction of linear features, whereas very large polygonal crater edges tend to be intersected by the linear features. This may hint at the different formation processes of polygonal craters depending on the embedded energy. In contrast, polygonal craters are also present in areas with no obvious tectonic features. These polygonal craters may be produced by sub-resolution or subsurface fissures and fractures."

PICs on Dione

Beddingfield et al. (2016) studied polygonal impact craters (PICs) in the wispy terrain, a region showing fractures, and the non-wispy terrain which shows no fractures (Beddingfield et al., 2016) (see Fig. 2.25).

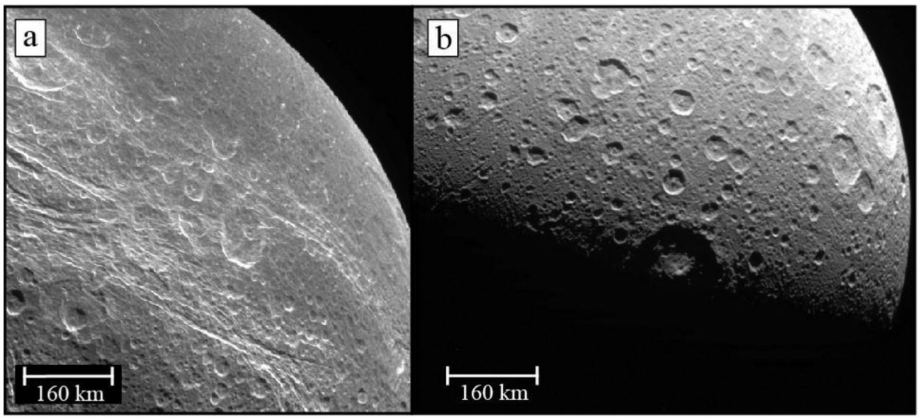

Figure 2.25: a) "Dione's wispy terrain (lower left corner) on the trailing hemisphere" (Beddingfield et al. (2016), p. 166), having a resolution of 432 m/px b) "Dione's non-wispy terrain on the leading hemisphere" (Beddingfield et al. 2016, p. 166), having a resolution of about 765 m/pixel. Both images were taken from the Cassini mission (Beddingfield et al., 2016). Credit: Beddingfield et al. (2016), p. 166.

The authors studied five areas in the wispy terrain and thirty in the non-wispy terrain; for each area they examined the closest five impact craters in the wispy terrain and the closest ten craters in the non-wispy terrain. Figure 2.26 shows the randomly selected study regions by Beddingfield et al. (2016).

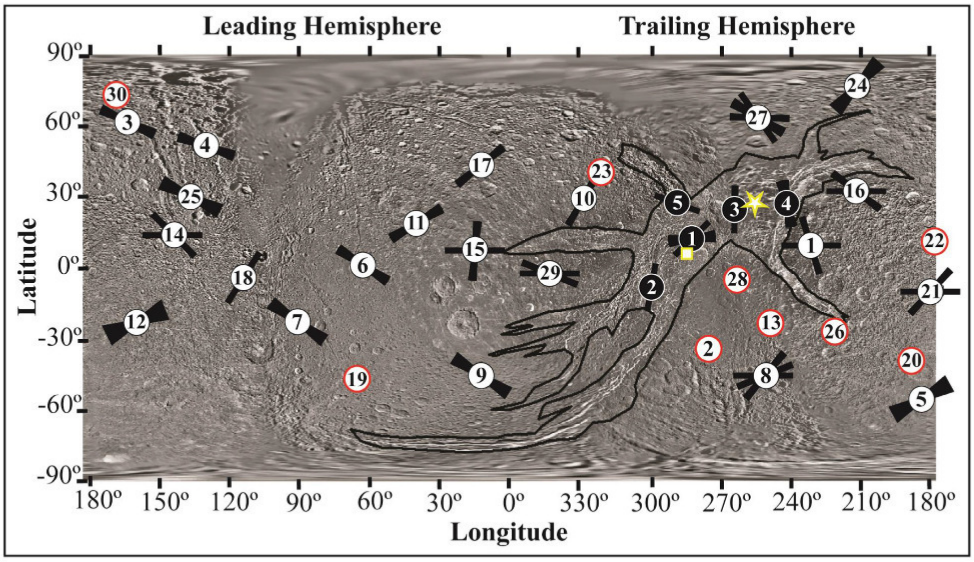

Figure 2.26: Map of Dione showing the wispy terrain study locations (numbers 1 to 5, in black) and the non-wispy terrain study locations (numbers 1 to 30, in white, the red circles represent study region without any PICs in the non-wispy terrain, the square shows Amata crater and the star an unnamed crater (Beddingfield et al., 2016). In all the study regions the PIC azimuths are marked (Beddingfield et al., 2016). The black borders show the wispy terrain. "The presence of PICs imply that subtle fractures are present throughout Dione's non-wispy terrain" (Beddingfield et al. (2016), p. 173). Credit: Beddingfield et al. (2016), p. 173.

The authors termed craters polygonal that have only one straight crater rim segment, arguing that "even a single straight rim segment can reflect a controlling fracture, we use this more general definition to capture more completely the possible presence of fractures. Thus, our results may be more inclusive than those of other studies" (Beddingfield et al. (2016), p. 164).

They found that about 76% of craters in the wispy terrain and 35% in the non-wispy terrain are polygonal and concluded that "subtle and/or nonvisible fractures are present within Dione's non-wispy terrain" (Beddingfield et al. (2016), p. 171). Also, a correlation between the orientation of straight crater rim segments and fractures and lineations was found and a map of fractures and faults on Dione was created using the straight segment orientations (see Fig. 2.27).

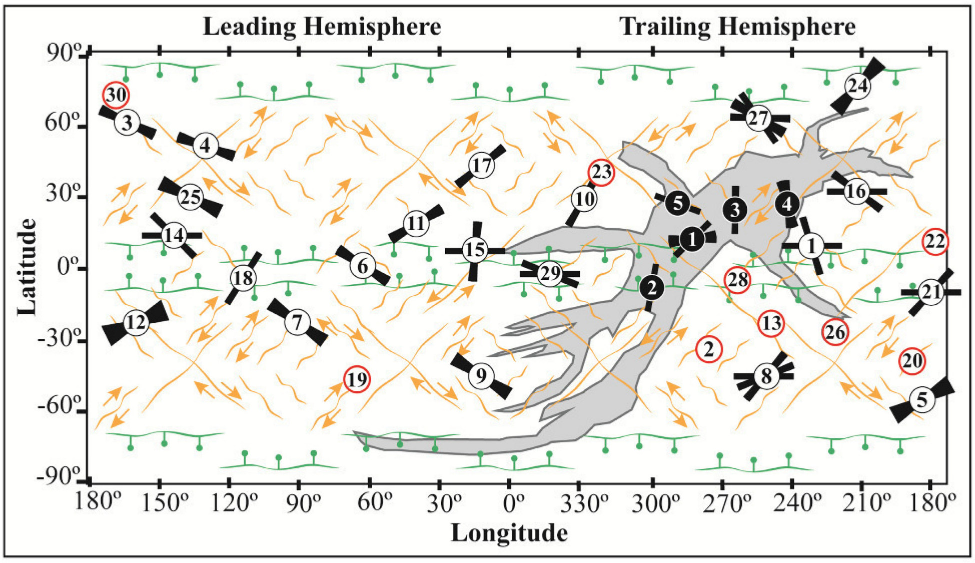

Figure 2.27: "The deformation pattern, including normal faults (green) and strike-slip faults (orange) associated with separate occurrences of satellite volume expansion and despinning for a satellite with a thinner lithosphere in the equatorial region and a thicker lithosphere in the polar regions (Beuthe, 2010). Rose diagrams of inferred fractures for wispy terrain (gray) and non-wispy terrain (white) study locations are also shown" (Beddingfield et al. (2016), p. 176). Credit: Beddingfield et al. (2016), p. 176.

Beddingfield et al. (2016) did not find a fixed distribution of diameters of polygonal impact craters (see Fig.2.28).

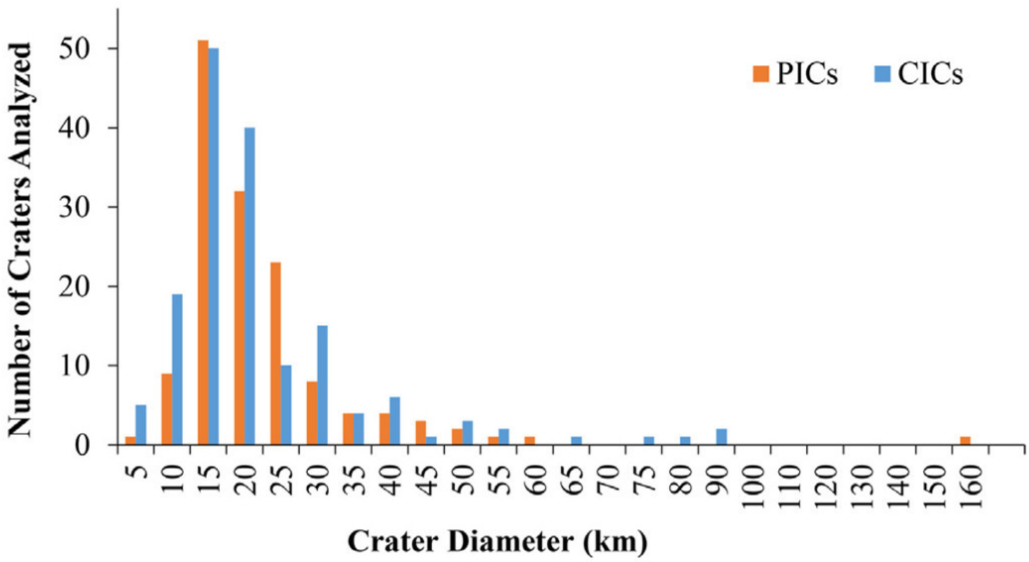

Figure 2.28: Distribution of diameters of polygonal impact craters (PICs) and non-polygonal impact craters (CICs) in the non-wispy terrain of Dione (Beddingfield et al., 2016). "These two distributions are similar" (Beddingfield et al. (2016), p. 175). Credit: Beddingfield et al. (2016), p. 175.

PICs on other objects of the Solar System

Crater Nergal on Ganymede, which has a diameter of about 8 km, is polygonal and has a central peak where "the eastern rim is highly modified and appears to follow the trend of impinging lineaments in Byblus" which is a groove lane (Thomas et al., 1998).

Helfenstein et al. (2005) mention that the surface of Enceladus not only shows various tectonic features like fractures and grooves, but also polygonal craters.
Many craters which are greater than 10 km on Rhea are polygonal; Moore et al. (1985) measured the orientations of 191 crater rim segments finding that they showed preferred trends and therefore reflected regional stresses. The authors also stated that "large craters are just as likely to have polygonal rims as small craters (≥10 km) with the same morphological freshness" (Moore et al. (1985), p. 792).

Denk et al. (2005) point out that what is probably the largest impact basin on Iapetus is polygonal, with a diameter of about 550 km located near 15°C/30°W. Porco et al. (2005) report the existence of a large basin having a diameter of about 380 km located near 15°S, 120°W on the anti-Saturn hemisphere of Iapetus having a polygonal outline and probably a central peak.

Ruesch et al. (2014a) mention that degraded craters on Vesta "might display a polygonal shape" (Ruesch et al. (2014a), p. 46).
On 433 Eros polygonal impact craters were found as well (Zuber et al., 2000; Prockter et al., 2002). PICs are present on the surface of Mathilde too, which is a C-type asteroid with a size of 66 km × 48 km × 46 km (Veverka et al., 1997). Craters having diameters of 26 km and 6 km with polygonal outlines can be seen, "craters larger than 5 km show strong polygonality" and "the only possible

evidence of a fractured fabric within Mathilde is the occurrence of polygonal-shaped, medium-sized craters" (Veverka et al. (1997), p. 2112).

Also, some impact craters found on comet Wild 2 are polygonal (Basilevsky and Head, 2006).

3 Data and Methods

The first and probably the most important task was to select the bodies on which PICs should be studied. This also depended on the availability of surface maps, their resolution, and global coverage. The IAU/NASA/USGS Planetary Database, created by the IAU Working Group for Planetary System Nomenclature, provides surface maps of many objects, including lists of different features on their surfaces, for example craters, where information about their diameters and coordinates can be acquired (see Fig. 3.29).

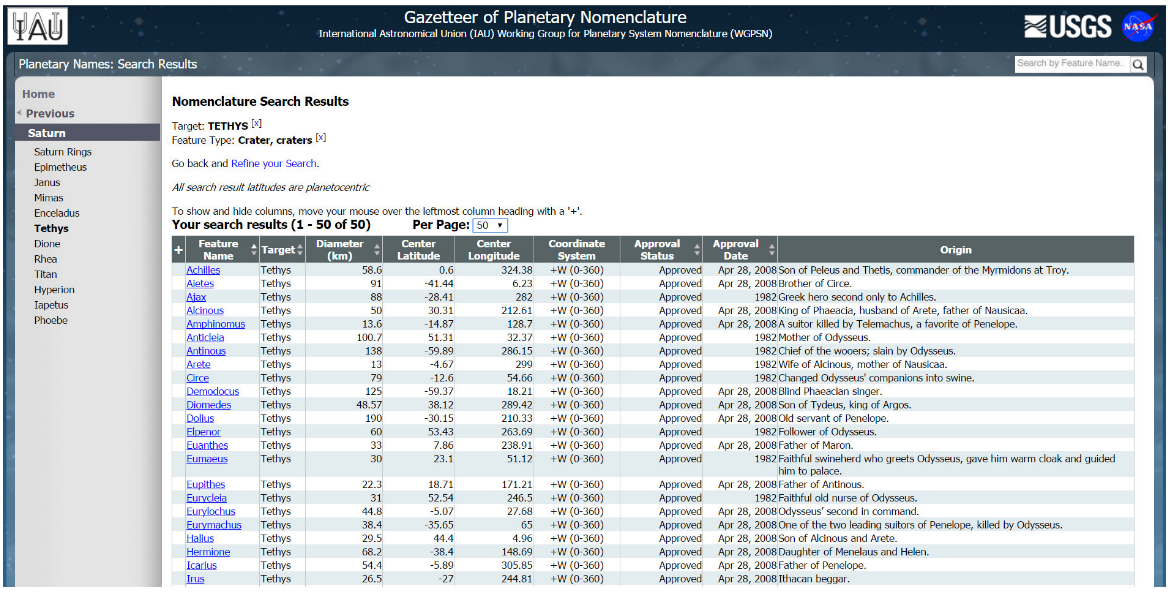
Gazetteer of Planetary Nomenclature
International Astronomical Union (IAU) Working Group for Planetary System Nomenclature (WGPSN)
Planetary Names: Search Results

Home
Previous
Saturn
Saturn Rings
Epimetheus
Janus
Mimas
Enceladus
Tethys
Dione
Rhea
Titan
Hyperion
Iapetus
Phoebe

Nomenclature Search Results

Target: **TETHYS** [x]
Feature Type: **Crater, craters** [x]

Go back and Refine your Search.

All search result latitudes are planetocentric

To show and hide columns, move your mouse over the leftmost column heading with a '+'.
Your search results (1 - 50 of 50) **Per Page:** 50

Feature Name	Target	Diameter (km)	Center Latitude	Center Longitude	Coordinate System	Approval Status	Approval Date	Origin
Achilles	Tethys	58.6	0.6	324.38	+W (0-360)	Approved	Apr 28, 2008	Son of Peleus and Thetis, commander of the Myrmidons at Troy.
Aietes	Tethys	91	-41.44	6.23	+W (0-360)	Approved	Apr 28, 2008	Brother of Circe.
Ajax	Tethys	88	-28.41	282	+W (0-360)	Approved	1982	Greek hero second only to Achilles.
Alcinous	Tethys	50	30.31	212.61	+W (0-360)	Approved	Apr 28, 2008	King of Phaeacia, husband of Arete, father of Nausicaa.
Amphinomus	Tethys	13.6	-14.87	128.7	+W (0-360)	Approved	Apr 28, 2008	A suitor killed by Telemachus, a favorite of Penelope.
Anticleia	Tethys	100.7	51.31	32.37	+W (0-360)	Approved	1982	Mother of Odysseus.
Antinous	Tethys	138	-59.89	286.15	+W (0-360)	Approved	1982	Chief of the wooers; slain by Odysseus.
Arete	Tethys	13	-4.67	299	+W (0-360)	Approved	1982	Wife of Alcinous, mother of Nausicaa.
Circe	Tethys	79	-12.6	54.66	+W (0-360)	Approved	1982	Changed Odysseus' companions into swine.
Demodocus	Tethys	125	-59.37	18.21	+W (0-360)	Approved	Apr 28, 2008	Blind Phaeacian singer.
Diomedes	Tethys	48.57	38.12	289.42	+W (0-360)	Approved	Apr 28, 2008	Son of Tydeus, king of Argos.
Dolius	Tethys	190	-30.15	210.33	+W (0-360)	Approved	Apr 28, 2008	Old servant of Penelope.
Elpenor	Tethys	60	53.43	263.69	+W (0-360)	Approved	1982	Follower of Odysseus.
Euanthes	Tethys	33	7.86	238.91	+W (0-360)	Approved	Apr 28, 2008	Father of Maron.
Eumaeus	Tethys	30	23.1	51.12	+W (0-360)	Approved	1982	Faithful swineherd who greets Odysseus, gave him warm cloak and guided him to palace.
Eupithes	Tethys	22.3	18.71	171.21	+W (0-360)	Approved	Apr 28, 2008	Father of Antinous.
Eurycleia	Tethys	31	52.54	246.5	+W (0-360)	Approved	1982	Faithful old nurse of Odysseus.
Eurylochus	Tethys	44.8	-5.07	27.68	+W (0-360)	Approved	Apr 28, 2008	Odysseus' second in command.
Eurymachus	Tethys	38.4	-35.65	65	+W (0-360)	Approved	Apr 28, 2008	One of the two leading suitors of Penelope, killed by Odysseus.
Halius	Tethys	29.5	44.4	4.96	+W (0-360)	Approved	Apr 28, 2008	Son of Alcinous and Arete.
Hermione	Tethys	68.2	-38.4	148.69	+W (0-360)	Approved	Apr 28, 2008	Daughter of Menelaus and Helen.
Icarius	Tethys	54.4	-5.89	305.85	+W (0-360)	Approved	Apr 28, 2008	Father of Penelope.
Irus	Tethys	26.5	-27	244.81	+W (0-360)	Approved	Apr 28, 2008	Ithacan beggar.

Figure 3.29: Table section of approved impact craters on Tethys from the IAU/NASA/USGS Planetary Database. Credit: IAU/NASA/USGS (2016).

Throughout this master's thesis all crater diameters and coordinates are taken from this database unless otherwise stated.

Table 3.1 shows the number of approved impact craters on different objects, including their minimum and maximum impact crater diameters and the maximum resolution of surface maps which are available from the IAU/NASA/USGS Planetary Database. Unknown diameters of 48 craters on Rhea were measured by the author.

For the study of polygonal impact craters, the Saturnian Satellites Rhea, Dione and Tethys, and the asteroids Ceres and Vesta, were selected due to the availability of global coverage maps that have an appropriate resolution. Another motive for choosing these objects was that there are only very few studies of PICs on these bodies (see chapter 2).

For the display of surface maps of Rhea, Dione, Tethys, Ceres, and Vesta, USGS's ISIS 3 (Integrated Software for Imagers and Spectrometers) and the program "qview" (see Fig. 3.30) were used, which

Object	# Craters	min. dia. (km)	max. dia. (km)	mean dia. (km)	Res. (m/px)
Mercury	392	0.93	1002	113.87	116
Venus	880	2.00	270.00	21.61	75
Moon	1616	0.06	536.37	57.64	100
Mars	1087	0.12	467.25	43.54	100
Phobos	17	1.50	9.00	3.09	5
Ceres	90	0.40	280.00	58.50	140
Vesta	90	0.57	450.00	34.72	60
Europa	41	1.10	50.00	12.46	500
Ganymede	128	2.90	343.00	73.92	1000
Callisto	141	11.10	210.00	60.60	1000
Enceladus	53	4.30	34.09	15.48	100
Tethys	50	11.80	445.00	73.54	293
Dione	73	11.90	350.00	63.02	154
Rhea	128	2.9	480.0	69.8	417
Titan	11	20.00	392.00	100.27	450
Iapetus	58	0.06	767.74	125.36	803

Table 3.1: Number of approved craters according to the IAU/NASA/USGS Database including the smallest and largest diameters and their maximum resolution. Unknown diameters of 48 approved craters on Rhea were measured by the author. Unapproved craters and dropped craters were removed from the list.

enable one "to manipulate imagery collected by current and past NASA and International planetary missions sent throughout our Solar System" (USGS, 2017). The same program was also used for the measurement of the unknown diameters of 48 craters on Rhea.

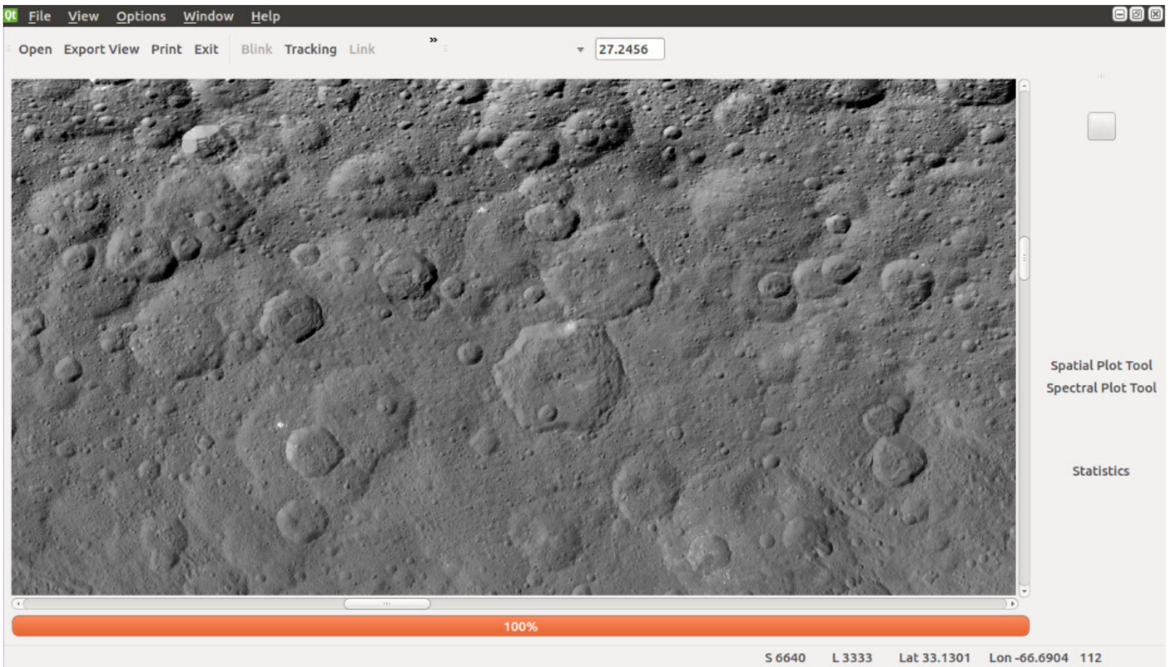

Figure 3.30: Surface of Ceres using ISIS 3 "qview" which enables the display of images by planetary missions. Credit: IAU/NASA/USGS (2016).

The global surface map of Rhea was created using data from the NASA's Cassini and NASA's Voyager fly-bys and has a resolution of about 417 metres/pixel (USGS, 2016). The map of Dione uses images of the Cassini spacecraft fly-bys and the Voyager mission, having a resolution of about 154 metres/pixel (USGS, 2016). The surface map of Tethys consists of images taken from Cassini fly-bys and has a resolution of about 293 metres/pixel (USGS, 2016).
The surface maps of Ceres and Vesta were created using images from the Dawn framing camera, having resolutions of about 140 metres/pixel and about 60 metres/pixel, respectively (USGS, 2016).

Of all approved impact craters on these objects, PICs were identified according to the definition by Öhman et al. (2003); the straight crater rim segments were marked and the angles between the straight segments were measured using the image editor GIMP (see Fig. 3.31 and Fig. 3.32).

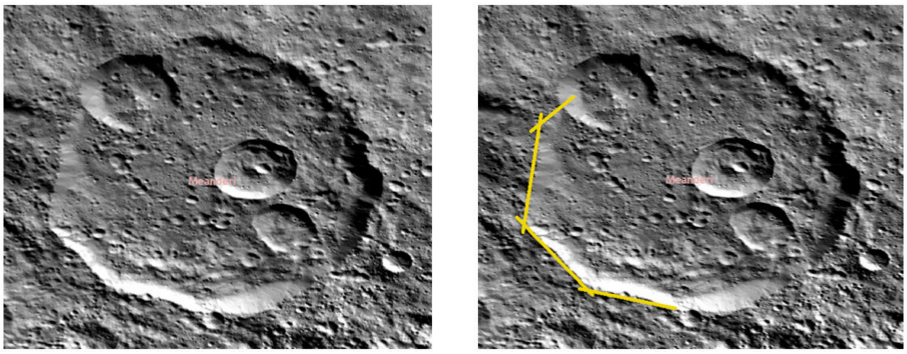

Figure 3.31: Polygonal impact crater Meanderi on Ceres having a diameter of 103 km located at a latitude of -40.8° and a longitude of 194.19° (left), including its marked straight crater rim segments (right). Credit: IAU/NASA/USGS (2016).

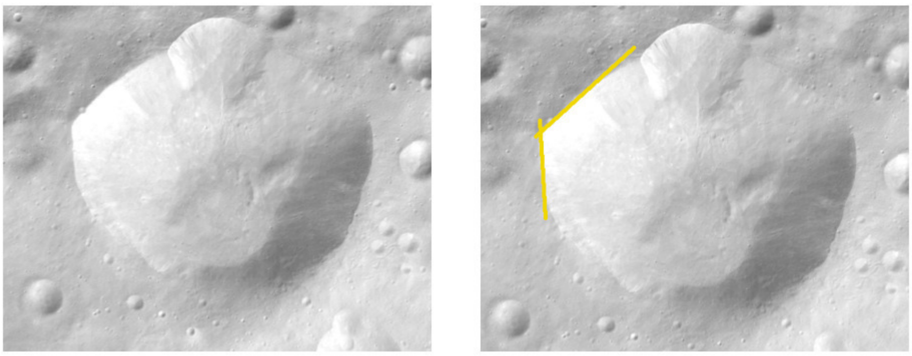

Figure 3.32: Polygonal impact crater Lepida on Vesta having a diameter of 42.9 km located at a latitude of 16.74° and a longitude of 96.76° (left), including its marked straight crater rim segments (right). Credit: IAU/NASA/USGS (2016).

4 Saturnian Satellites

4.1 Rhea

Saturn's satellite Rhea was discovered by Giovanni Domenico Cassini on 23 December 1672 and is named after the Greek Titan Rhea whose husband was Kronus, the Roman Saturn (NASA Rhea, 2017).

Having a mean radius of about 764 km and a mass of 23.1×10^{20} kg (NASA, 2015), it is after Titan the second largest satellite of Saturn (e.g. Tortora et al., 2016). Rhea orbits Saturn tidally locked at a distance of about 527 000 km in 4.5 days within Saturn's magnetosphere at the outer edge of the E-ring (e.g. Filacchione et al., 2012; Scipioni et al., 2014). Its orbit has an eccentricity of 0.0010 and an inclination of 0.35° (NASA, 2015), while its surface gravity is about 0.264 m/s^2 (NASA JPL, 2017). Rhea does not have an internal magnetic field (Khurana et al., 2008). The surface temperature ranges from about 25 K at the poles up to about 99 K in the equatorial region (Khurana et al., 2008; Howett et al., 2016). Figure 4.33 shows an image of Rhea's trailing hemisphere taken from the Cassini spacecraft on 21 November 2009 at a distance of about 30 000 km (NASA, 2010).

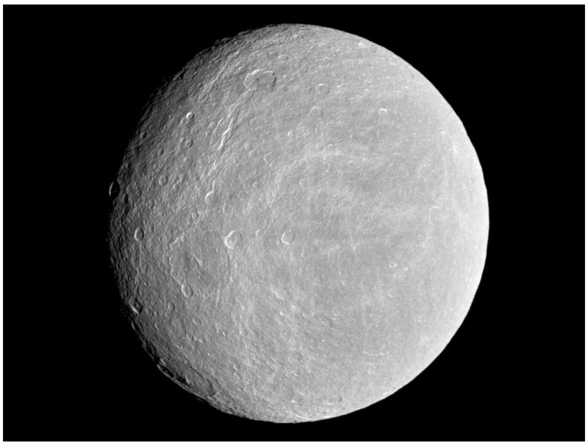

Figure 4.33: Rhea's trailing hemisphere showing its cratered plains and bright fractures (left) (NASA 2010) taken from the Cassini spacecraft on 21 November 2009 at a distance of about 30 000 km. Credit: NASA/JPL/Space Science Institute.

Rhea's albedo is 0.65 (Wagner et al., 2008), where a strong dichotomy between Rhea's leading and trailing hemisphere can be seen. Rhea's leading hemisphere is brighter than its trailing hemisphere, the difference in albedo being about 20% (Buratti et al., 1990). This effect is caused by the "bombardment of charged particles from the interplanetary medium and driven by Saturn's magnetosphere" (Scipioni et al., 2015, and references therein) which contaminate the surface. Another cause of the dichotomy are the impact of pure water ice grains originating from plumes at the south pole of Enceladus which give rise to a brighter leading hemisphere (Scipioni et al., 2015, and references therein).

The surface of Rhea consists mostly of water ice with minor contributions of organic polymers and carbon dioxide (Czechowski, 2012). Rhea's low mean density of about 1240 kg/m^3 (NASA, 2015) indicates a composition mainly of water ice (Scipioni et al., 2014). It is unknown whether Rhea is differentiated or not (Thomas et al., 2007; Iess et al., 2007; Anderson and Schubert, 2010; Asmar et al., 2009; Thomas, 2010). Castillo (2005) proposed ten different models concerning the interior of Rhea using different states of differentiation, rock densities, degrees of hydration, and the presence or absence of ice II but did not favour a certain model. Anderson and Schubert (2010) state that "Rhea is an undifferentiated satellite made up of about 25% rock-metal and 75% water ice by mass" (Anderson and Schubert (2010), p. 176). Other authors propose a weak differentiated interior consisting of a denser core and a water ice mantle and crust, which is also in accordance with observations that Rhea's crust consists of almost pure water ice, where the depth of the ice in the crust is at least 4 km (Tortora et al., 2016; Stephan et al., 2012).

Rhea is heavily cratered and shows various features, for example, rift zones (chasmata), troughs, ridges and graben (e.g. Byrne et al., 2015; Wagner et al., 2010b) (see Fig. 4.33). The leading hemisphere of Rhea shows a higher crater density than the trailing one (APOD, 2006). The high number of impact craters on Rhea indicates a surface age of about 4 billion years, older than the surfaces of Dione and Tethys which are not so heavily cratered (Wagner et al., 2010a). The simple-to-complex transition diameter is about 8 km (White and Schenk, 2011).
The largest crater on Rhea, Tirawa, has a diameter of 360 km and is located at 34.2°N and 151.7°W (Howett et al., 2014). Another notable crater is Inktomi (see Fig. 4.33 (left)) which has a diameter of about 48 km and is located on the leading hemisphere at 14.1°S and 112.1°W. Inktomi is very young (8-280 Ma) and shows "an extended system of bright rays" (Howett et al. (2014), p. 240) extending for hundreds of kilometers (Scipioni et al., 2014) (see Fig. 4.34). Additionally, the largest ice particles which have been found on the surface of Rhea are located at this crater (Stephan et al., 2012). Almost pure water ice is found near tectonic scarps and young impact craters (Stephan et al., 2012).

The largest rift zones are Galunlati Chasma and Yamsi Chasma which "are both located close to the center of Rhea's trailing hemisphere" (Byrne et al., 2015) and have a N-S trend. Galunati Chasma is the largest, extending over about 1500 km (Byrne et al., 2015). Both rift zones have widths from 40 to 90 km (Byrne et al., 2015). The graben have widths of up to 30 km (Wagner et al., 2010b). The phase transformation of ice in the interior of Rhea leads to the expansion of the outer layers causing these tectonic features (Faure and Mensing, 2007). These rift zones can be seen as bright streaks on Rhea's surface as shown in Fig. 4.35.

Rhea has a thin exosphere consisting of oxygen and carbon dioxide which shows seasonal changes having peak densities of 5 and $2 \pm 1 \times 10^{10}$ molecules/m^3 respectively (Teolis and Waite, 2011; Teolis et al., 2010, 2011; Teolis and Waite, 2016). "Rhea's O_2 is a chemical decomposition product of the surface ice due to irradiation by Saturn's magnetospheric plasma. Exospheric CO_2 may be (i) synthesized from radiolysis involving surface-bound oxygen and endogenic and/or implaneted organics, and/or (ii) may be due to escape of primordial CO_2 from the ice" (Teolis and Waite, 2011).

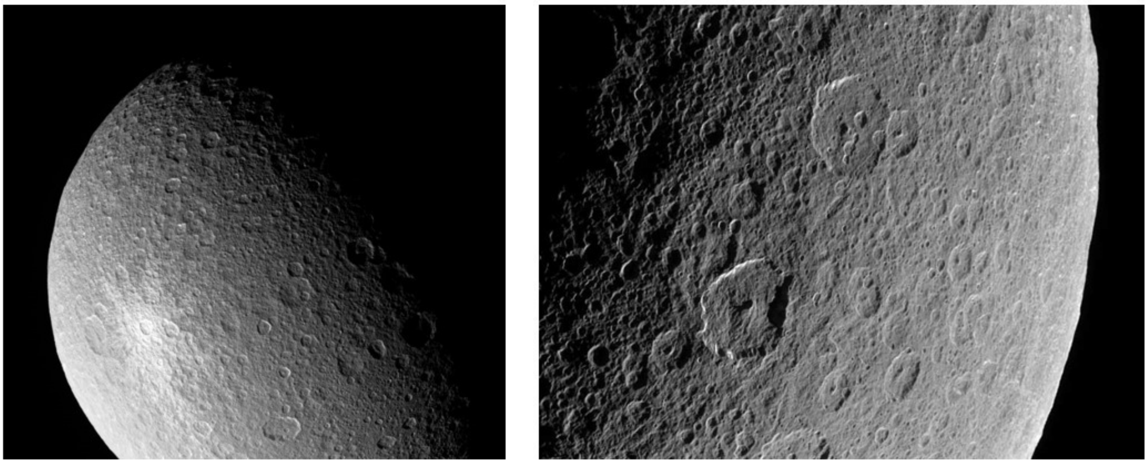

Figure 4.34: Left: Young crater Inktomi on Rhea having a diameter of about 48 km on the leading hemisphere and showing bright rays which extend for hundreds of kilometers (Howett et al., 2014). Credit: NASA/JPL/Space Science Institute. Right: Old, heavily cratered terrain on Saturn's leading hemisphere, taken by the Cassini spacecraft at a distance of about 100 000 km (APOD, 2006). Credit: Cassini Imaging Team, SSI, JPL, ESA, NASA.

Figure 4.35: Rhea's hemisphere opposite Saturn showing bright stripes which are rift zones having ice cliffs (DLR, 2017). Credit: NASA/JPL/Space Science Institute.

4.2 Dione

Dione was discovered on 21 March 1684 by Giovanni Domenico Cassini and is named after the Greek godness Dione, the daughter of Tethys (sister of Kronus) (NASA Dione, 2017).
Dione orbits Saturn within 2.7 days at a distance of 377.40×10^3 km (NASA, 2015) in a locked orbit within the E-ring (Hendrix and Hansen, 2005). Its eccentricity is 0.0022 and its inclination is 0.02° (NASA, 2015). With a size of $563 \times 561 \times 560$ km and a mass of 11.0×10^{20} kg Dione's density,

of about 1480 kg/m^3 (NASA, 2015), is higher than that of Rhea. It has a surface temperature of about 87 K (NASA Dione, 2017) and a surface gravity of 0.232 m/s^2 (NASA JPL, 2016b). There are two trojan moons, Helene and Polydeuces, located at L4 and L5 respectively (NASA Dione, 2017).

Dione consists primarily of water ice and may have a core composed of silicates (Hendrix et al., 2005). In a model by Thomas et al. (2007), the core makes up 54% of the satellite's mass and has a radius of about 360 km. Figure 4.36 shows an image of Dione taken by the Cassini spacecraft at a distance of about 211 000 km (NASA, 2008).

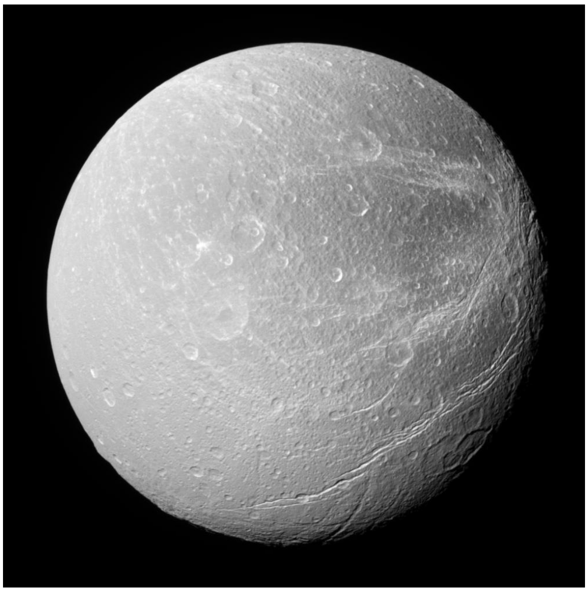

Figure 4.36: Image of Dione showing cratered surface, canyons (right) and albedo differences, taken by the Cassini spacecraft at a distance of about 211 000 km (NASA, 2008). Credit: NASA/JPL/Space Science Institute.

Dione has an albedo of about 0.7 in which a strong dichotomy between the leading and trailing hemispheres can be observed. The albedo of the leading hemisphere is about 40% higher than that of the trailing hemisphere (Buratti et al., 1990). There is a decrease in the flux of the E-ring particles from Tethys to Dione to Rhea, depending on the distance to Enceladus which also affects the ice cleanness of their surfaces (Ostro et al., 2010). As on Rhea, the surface of Dione is also affected by Saturn's charged particles and E-ring particles (Filacchione et al., 2012).

Dione's surface consists primarily of water ice (99%), minor amounts of carbon dioxide and, probably, minor amounts of methane or ammonia (Hendrix and Hansen, 2005; Clark et al., 2008). "Carbon dioxide is distributed relatively uniformly over Dione's surface" (Clark et al. (2008), p. 377) where its abundance is higher than it is on Rhea (Scipioni et al., 2014). The surface of Dione is heavily cratered but not as much as on Rhea (Scipioni et al., 2012) (see Fig. 4.37); less cratered plains can also be seen on the surface (Scipioni et al., 2012, and references therein). The heavily cratered plains on Dione are estimated to be older than 4 gyr, whereas smooth plains, which have been resurfaced, are younger, having ages of about 1.5 gyr (Kirchoff and Schenk, 2010). The largest crater on Dione is Evander which has a diameter of 350 km and is located at a latitude of -57° and a longitude of 145° (IAU, 2017).

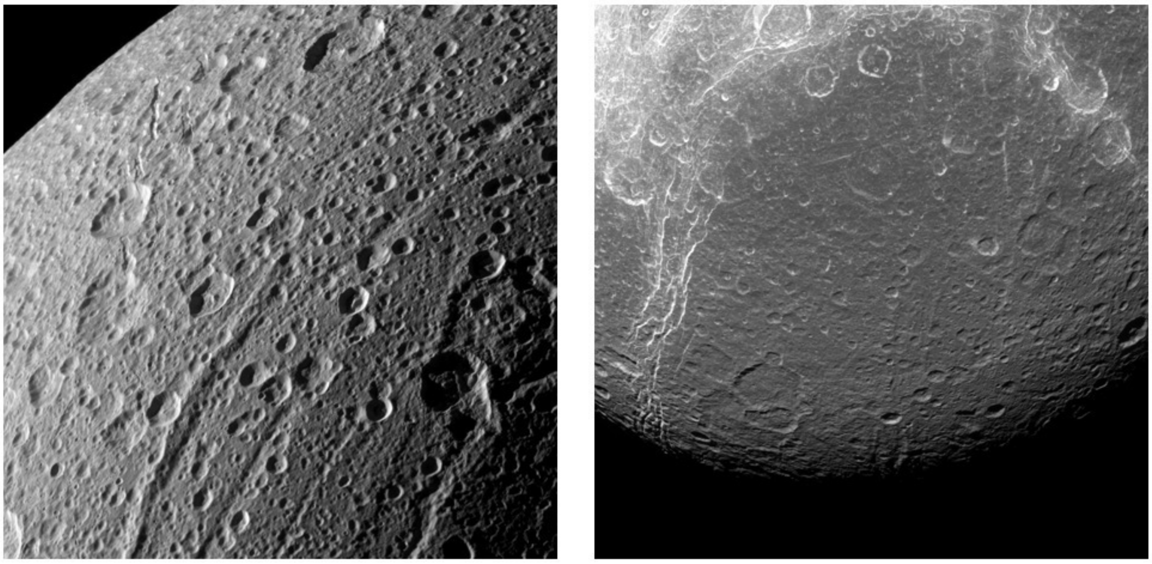

Figure 4.37: Left: Image of Dione's leading hemisphere showing fractures and craters, taken by the Cassini spacecraft on 27 January 2010 at a distance of about 46 000 km (NASA, 2013). Credit: NASA/JPL/Space Science Institute. Right: Image of Dione's trailing hemisphere showing bright linear tectonic features and impact craters taken by the Cassini spacecraft on 11 April 2015 at a distance of about 110 000 km (NASA, 2016). Credit: NASA/JPL-Caltech/Space Science Institute.

The largest ray crater on Dione is Creusa, having a diameter of about 36.2 km (Wagner et al., 2011) (see Fig. 4.38) . Its "bright rays extend over several hundreds of kilometers almost over the entire sub-Saturnian hemisphere" (Wagner et al., 2011). Creusa is a very young crater with an estimated age of less than 500 ma (Wagner et al., 2011) showing "the highest amount of fresh, non-contaminated water ice" (Scipioni et al., 2013). As the trailing hemisphere is more cratered than the leading hemisphere one theory is that an impact spun the satellite around (NASA Dione, 2017).

Other features of Dione's surface are the rifts resulting from tectonic processes which are more complex on Dione than they are on Rhea and Tethys and have a N-S orientation on the trailing hemisphere (Byrne et al., 2015). The largest rifts are Palatine Chasmata, Eurotas Chasmata and Padua Chasma which have widths between 40 to 70 km; all rifts have a total length of about 1300 km (Byrne et al., 2015). There are also lineaments which have high albedos across the whole hemisphere (Moore et al., 2004).

There are some indications that geologic activity has occurred in the recent past, for example the presence of smooth plains that have been resurfaced and the relaxation of Janiculum dorsum (a ridge with a length of about 500 km) which cannot be explained by radioactive decay alone (Howett et al., 2014). Therefore, one possible explanation for this relaxation could be the presence of a subsurface ocean at the time when Janiculum dorsum was formed (Howett et al., 2014).

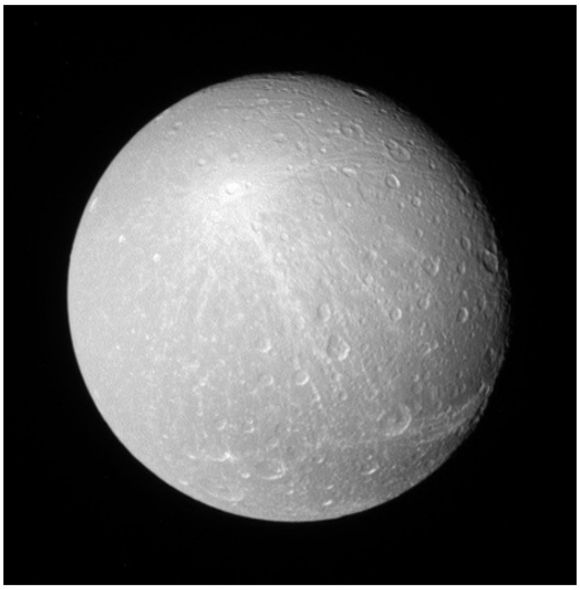

Figure 4.38: Image of Dione's surface showing bright rays of young crater Creusa taken by the Cassini spacecraft on 26 November 2016 at a distance of about 560 000 km (NASA, 2017). Credit: NASA/JPL-Caltech/Space Science Institute.

Dione has a thin atmosphere consisting of oxygen and carbon dioxide with a density of about $2 \times 10^{10}\,\mathrm{m}^{-3}$ showing seasonal variability (Teolis and Waite, 2012, 2016).

4.3 Tethys

Tethys was discovered on 21 March 1684 by Giovanni Domenico Cassini and is named after the Greek goddess Tethys, a sister to Kronos, who was mother of the chief rivers (NASA Tethys, 2017).
Having a diameter of about 1066 km (Wagner et al., 2013b) and a mass of 6.18×10^{20} kg (NASA, 2015) it orbits Saturn locked within 1.9 days at a distance of 294.66×10^3 km (NASA, 2015). Tethys lies in both Saturn's magnetosphere and the E-ring (Kriegel et al., 2009). Its orbit has an eccentricity of 0.0000 and an inclination of about 1.86° (NASA, 2015). Tethys does not have an intrinsic magnetic field (Kriegel et al., 2009) and is in a 1:2 resonance with Mimas (Buratti et al., 2010). There are two trojan moons, Telesto, located at L4, and Calypso, at L5 (NASA Tethys, 2017). The average temperature on the surface of Tethys is about -187 °C (NASA Tethys, 2017).

The satellite has a very low mean density of about 0.985 g/cm^3 and models by Thomas et al. (2007) imply that its core has a radius of about 145 km which comprises only 6% of the total mass. Other authors, for example Thomas et al. (2006), propose that Tethys is undifferentiated and composed mostly of water ice. Figure 4.39 shows an image of Tethys taken by the Cassini spacecraft on 30 August 2007 at a distance of about 97 000 km (NASA, 2007). The giant multi-ringed impact basin Odysseus can be seen to the upper left.

Tethys has an albedo of about 0.8 which is the second largest albedo of any satellite of Saturn after Enceladus (NASA, 2015). As on Rhea and Dione, an albedo difference between the leading and trail-

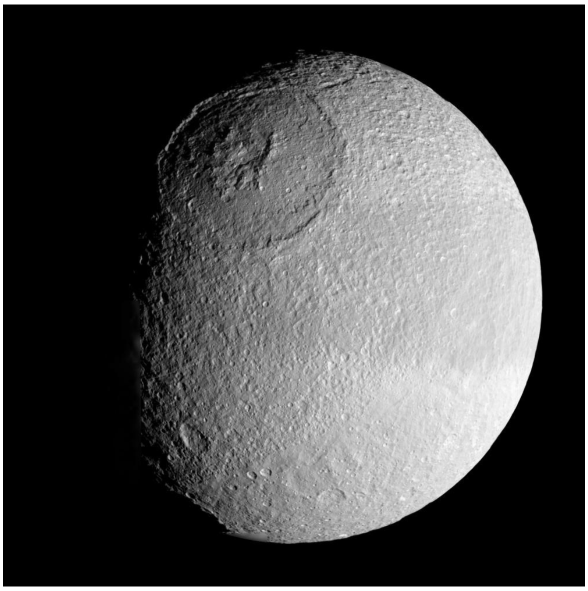

Figure 4.39: Image of Tethys showing the giant multi-ringed impact basin Odysseus (upper left), taken by the Cassini spacecraft on 30 August 2007 at a distance of about 97 000 km (NASA, 2007). Credit: NASA/JPL/Space Science Institute.

ing hemispheres can be seen on Tethys, where the leading hemisphere is 10-15 % brighter (Buratti et al., 1990).

The surface of Tethys consists mostly of water ice (Stephan et al., 2015) and is affected by E-ring particles originating from Enceladus, plasma ions, neutral particles and energetic particles (Royer and Hendrix, 2013). Faults, graben, hilly cratered terrain and smooth plains can be seen on Tethys (e.g. Stephan et al., 2016, 2013; Giese et al., 2007). The surface of Tethys is not as heavily cratered as it is on Rhea and Dione, probably due to tidal warming caused by being nearer to Saturn (NASA Tethys, 2017).

Two major features on the surface of Tethys can be seen: the 400 km diameter, multi-ringed impact basin Odysseus comprising about 40% of the satellite's diameter and the large graben system Ithaca Chasma (Wagner et al., 2013a; Scipioni et al., 2015). The impact basin Odysseus "is a fresh to partly degraded large impact structure with a central peak complex, wall terraces, secondary crater chains, and slivers of smooth deposits within the heavily cratered plains, possibly impact ejecta" (Wagner et al., 2013a). "Odysseus is characterized by an elevated complex, including a central peak surrounded by a horsehoe-shaped mountain" (Stephan et al. (2016), p. 12) named Scheria Montes which has a diameter of about 100 km (Roatsch et al., 2009). One theory is that the impact which caused the Odysseus basin also led to the formation of Ithaca Chasma (Smith et al., 1981, 1982), but crater counts show that the impact basin Odysseus is younger than Ithaca Chasma which has an estimated age of about 4 Ga (Giese et al., 2007).
One of the youngest craters is Telemachus which has "a sharp crater rim, well-discernible ejecta blankets, and a low superimposed crater frequency" (Wagner et al., 2013a) and also shows strong water

ice absorptions. The transition from simple to complex impact craters takes place at a diameter of about 15.4 km according to Moore et al. (2004).

Ithaca Chasma has a depth of about 3 km, a width of between 70 km and 110 km and an extension of over 2000 km; it contains rims with heights of about 0.5 km compared to the surroundings and flanks up to 6 km (Giese et al., 2006; Byrne et al., 2015; Giese et al., 2007) (see Fig. 4.40). One possible explanation for the origin of Ithaca Chasma lies in the extension of freezing water (Moore and Ahern, 1983). Ithaca Chasma is heavily cratered (Stephan et al., 2016) and does not show strong water ice absorption features in contrast to Rhea and Dione whose graben systems "show fresh ice exposed on steep walls" (Stephan et al., 2013), which suggests that Ithaca Chasma is very old. "Whereas geologically young surface features are characterized by pure H_2O-ice composition with relatively large particles, which match the particle sizes measured for fresh surface features also on Dione and Rhea, geologically old weathered regions are dominated by submicron-sized ice particles" (Stephan et al. (2016), p. 1).

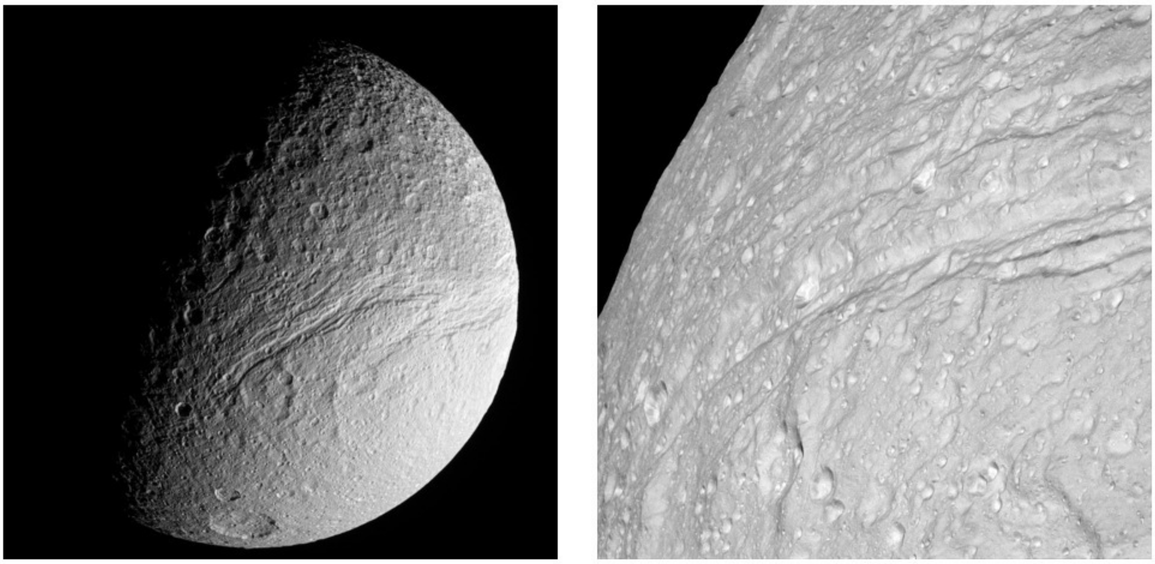

Figure 4.40: Left: Ithaca Chasma on Tethys (right) taken by the Cassini spacecraft (APOD, 2008). Credit: Cassini Imaging Team, SSI, JPL, ESA, NASA. Right: Image of Ithaca Chasma showing ice cliffs and craters, taken by the Cassini spacecraft at a distance of 32 000 km (APOD, 2005). Credit: Cassini Imaging Team, SSI, JPL, ESA, NASA.

Just as with the surface of Mimas, variations in thermal inertia have also been observed on Tethys resulting "in warmer nighttime and cooler daytime temperatures by about 15 K than their surroundings" (Howett et al., 2013); these are most likely due to the bombardment of electrons (Howett et al., 2013, 2012, 2014) (see Fig. 4.41). "It is likely that these electrons mobilize water molecules in their path, and the water molecules recondense at grain contacts. This serves to increase the contact area between grains and thus increases the thermal conductivity (and hence thermal inertia); in essence the grains are glued together" (Howett et al. (2014), p. 240).

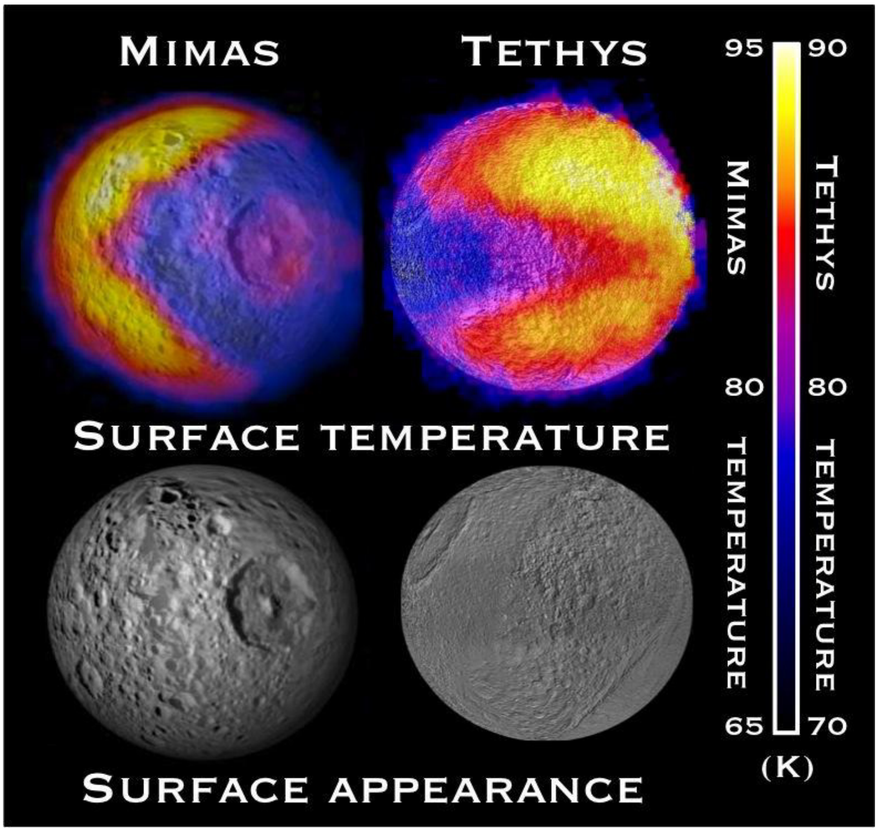

Figure 4.41: Temperature variations on Mimas and Tethys (NASA, 2012); these are most likely due to the bombardment of electrons leading to an increase in thermal conductivity resulting in "warmer nighttime and cooler daytime temperatures by about 15 K than their surroundings" (Howett et al., 2013). Credit: NASA/JPL.

5 Asteroid Belt Objects

5.1 Ceres

Ceres was discovered by Giuseppe Piazzi on 1 January 1801 and is named after the Roman goddess of corn and harvests (NASA Ceres, 2017).
With a diameter of $965 \times 961 \times 891$ km and a mass of about 9.393×10^{20} kg (NASA, 2016), it comprises about 25% of the total mass of the asteroid's belt (NASA Ceres, 2017). Ceres orbits the sun at a distance of about 2.8 AE within 4.60 yrs (NASA, 2016) and has a rotation period of about 9.074 h; its eccentricity is 0.0758 and its inclination is 10.59° (NASA, 2016).
Having a density of about 2.09 g/cm^3 (NASA JPL, 2016a), which is much lesser than the density of the terrestrial planets, suggests that Ceres contains large amounts of water ice (Bland, 2013). It is differentiated consisting of a rocky core, an ice-rich mantle and a crust (Bowling, 2016; Thomas et al., 2005; McCord and Sotin, 2005). Ceres has an albedo of 0.09 (Li et al., 2006) and temperatures of about 150-160 K at the equator and about 120 K in the polar regions, but over most of the surface area the temperature is about 160 K or higher (Bland et al., 2016; Dombard and Schenk, 2013). The surface gravity of Ceres is 0.28 m/s^2 (NASA JPL, 2016). Figure 5.42 shows an image of Ceres' cratered surface and the bright spots in the Occator crater, taken at a distance of 13 600 km (APOD, 2015).

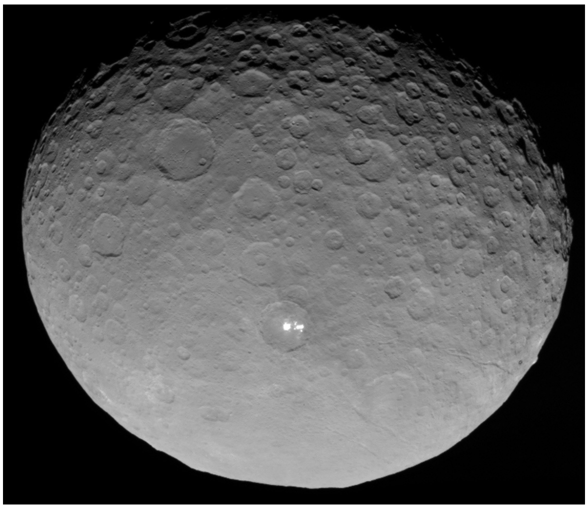

Figure 5.42: Image of Ceres taken at a distance of about 13 600 km, showing its heavily cratered surface and the bright spots in the Occator crater (APOD, 2015). Credit: NASA/JPL-Caltech/UCLA/MPS/DLR/IDA.

Prior to the Dawn mission it was believed that there were only a few craters on Ceres due to crater relaxation on the icy surface at the temperatures present on this asteroid (Bland, 2013). However, the first images by Dawn revealed a heavily cratered surface meaning that the surface does not contain as much water ice as expected, it is estimated that it consists of less than 40% ice by volume (Scully

et al., 2016; Raymond et al., 2016). Ceres' dark and dry surface (Russell et al., 2016) consists of ammoniated phyllosilicate, magnetite, antigorite and carbonate (De Sanctis et al., 2016a). Water ice is thermodynamically not stable on the surface (Fanale and Salvail, 1989) and has not been observed spectroscopically (Vernazza et al., 2005).
Linear structures can be seen including fractures and troughs where "a set of regional linear structures (RLS) cross much of the eastern hemisphere of Ceres" (Buczkowski et al., 2016). There are also densely and not as densely cratered plains on Ceres' surface having ages of up to 3.7 Ga and 3 Ga respectively (Wagner et al., 2016b,a) (see Fig. 5.43). Compared to the asteroid Vesta, there is a lack of large impact basins having diameters larger than 300 km which cannot be explained convincingly (Bowling, 2016; Raymond et al., 2016). According to collisional models, there should be at least ten craters having diameters greater than 400 km (Marchi et al., 2016). Raymond et al. (2016) suggest that Ceres is not fully differentiated and never had such a crust or that it lost its ice crust due to impacts.

Craters on Ceres show different degradation stages from pristine, well-preserved young craters to those that are highly degraded (Crown et al., 2016). The simple to complex crater transition is expected to be at diameters of about 12 km according to Schmedemann et al. (2015) and this suggests "that there is a significant amount of ice in the near surface" (Bowling (2016), and references therein). In general, impact craters on Ceres are similar to those on Saturn's midsized icy satellites (Schenk et al., 2015). Kerwan and Yalode are the largest impact craters on Ceres having diameters of about 280 km and 260 km (IAU, 2017) and ages of 2.8 Ga and 1.8 Ga respectively (Wagner et al., 2016b). The crater rim of Kerwan is heavily degraded, whereas its interior "is filled with a 'smooth terrain' that also extends beyond the rim to the east and west" which "hosts a significantly lower impact crater density than most of the rest of Ceres' surface" (Williams et al., 2016). Williams et al. (2016) suggest that "Kerwan impact occurred when Ceres' crust had a greater proportion of ice than at present, and that impact heating melted crustal material resulting in resurfacing of the Kerwan region by an icy impact melt, or possibly initiated cryovolcanic flows." Parts of the rim of the Yalode basin are sharply defined but are also irregular or degraded, whereas "the western rim of Yalode is disrupted by Urvara basin" (Crown et al., 2016). The crater Urvara which has a diameter of 170 km is located at a latitude of -45.66° and a longitude of 249.24° (IAU, 2017) and is about 0.48 Ga old (Wagner et al. 2016). One very young crater is Oxo with a diameter of 10 km located at a latitude of 42.21° and a longitude of 359.6° having an age between 0.5 and 1 Ma (Wagner et al., 2016a).

Several bright spots can be seen on the surface, for example in the Occator, Haulani and Oxo craters (De Sanctis et al., 2016a), with the brightest spots present within the Occator crater (see Fig. 5.44) which have a "reflectance more than 10 times the average of Ceres" (Schäfer et al., 2016) in contrast to the dark surface. Occator is a young crater less than 100 million years old (Zolotov, 2016). The bright spots are made of sodium carbonate which is very rare throughout the Solar System with Ceres having the largest known deposit (Zolotov, 2016). It is also present in the plumes of Enceladus (Zolotov, 2016). There are no tidal forces acting on this satellite (Nathues et al., 2015). De Sanctis et al. (2016b) propose that the bright spots are "the solid residue of crystallization of brines and entrained altered solids that reached the surface from below" (De Sanctis et al. (2016b), p. 54) where impacts are the heat source. Water vapour was detected at the Occator and Oxo craters and

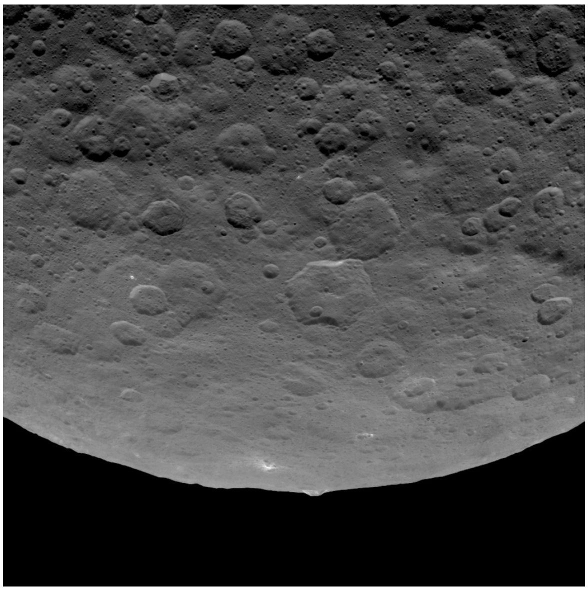

Figure 5.43: Image of heavily cratered surface on Ceres including bright spots in the Occator crater taken by the Dawn spacecraft (NASA JPL, 2015). Credit: NASA/JPL-Caltech/UCLA/MPS/DLR/IDA.

haze, probably consisting of water ice particles and dust which show diurnal variation (Nathues et al., 2015). Nathues et al. (2015) compare these processes with those on a comet's surface where "the haze forms in the morning after sunrise by the sublimation of water. The stream of vapour lifts tiny particles of dust and residual ice" (Nathues et al. (2015), p. 239). The detection of water vapour also suggests the presence of water ice near the surface of these two craters (Hughson et al., 2016). As water ice is not stable on the surface of Ceres and sublimates, calculations by Bowling et al. (2016) show that a region which is as large as that in the Occator crater is depleted within about 2000 years and, a region having a diameter of about 100 m, is depleted within 0.2 years. Salts are more stable on the surface than water ice (Combe et al., 2016). Another possible explanation for the bright spots could be the "release of subsurface materials by eruptions due to hydrothermal activity" as proposed by Combe et al. (2016).
The highest mountain on Ceres, Ahuna Mons which has a height of 4 km and a width of 17 km, is likely a cryovolcano (Ruesch et al., 2016) (see Fig. 5.45). It is located at a latitude of -10.48° and a longitude of 316.2° (IAU, 2017). At its summit, ridges, troughs and lineations can be seen suggesting "multiple phases of activity" (Ruesch et al., 2016). Ruesch et al. (2016) also estimated "the age of the most recent activity on Ahuna Mons to be within the past 210 $\pm$ 30 million years".

Aliphatic organic material has been detected on Ceres' surface near the Ernutet crater in a region having an expansion of about 1000 km^2 and a diameter of about 53 km, located at a latitude of about 53°N and a longitude of about 45.5°E (De Sanctis et al., 2017). De Sanctis et al. (2017) argue that the delivery of this material by an impact is very unlikely and that its origin is most probably due to internal processes. "The combined presence on Ceres of ammonia-bearing hydrated minerals, water ice, carbonates, salts, and organic material indicates a very complex chemical environment" (De Sanctis et al. (2017), p. 719).

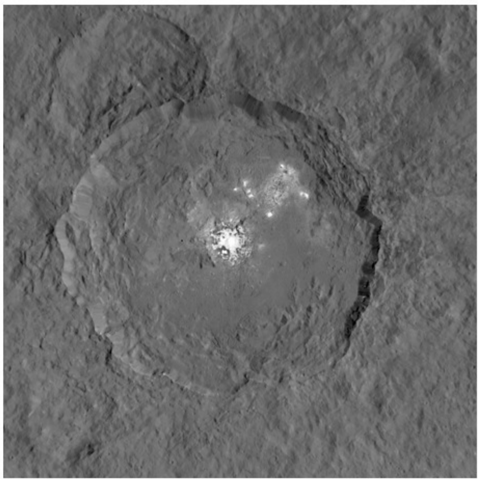

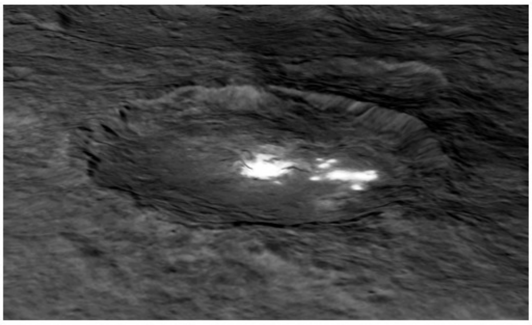

Figure 5.44: Left: Image of the Occator crater on Ceres showing bright spots, taken by the Dawn spacecraft (NASA/JPL, 2015a). Credit: NASA/JPL-Caltech/UCLA/MPS/DLR/IDA. Right: "An image of Occator Crater dropped over a digital terrain model provides a 3-D-like perspective view of the impact structure" showing bright spots (NASA/JPL, 2015b). Credit: NASA/JPL-Caltech/UCLA/MPS/DLR/IDA.

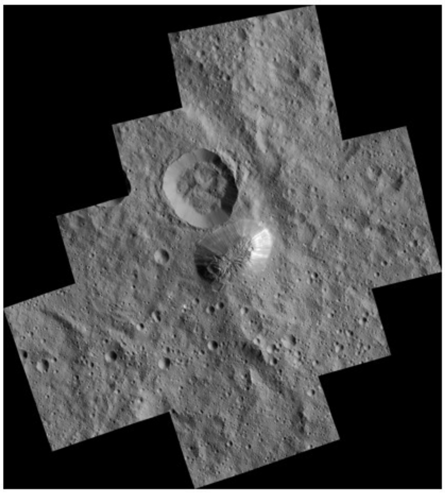

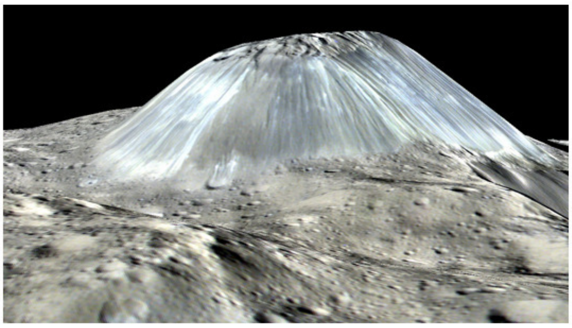

Figure 5.45: Left: Image of Ahuna Mons on Ceres taken by the Dawn spacecraft at a distance of 385 km in December 2015 (NASA/JPL, 2016a). Credit: NASA/JPL-Caltech/UCLA/MPS/DLR/IDA. Right: "Simulated perspective view" of Ahuna Mons "using enhanced color images" taken by the Dawn spacecraft at a distance of 385 km (NASA/JPL, 2016b). Credit: NASA/JPL-Caltech/UCLA/MPS/DLR/IDA/PSI.

5.2 Vesta

Vesta was discovered on 29 March 1807 by Heinrich Wilhelm Olbers and is named after the Roman goddess of the hearth and household (NASA Vesta, 2017).
Vesta is "the second largest object by mass and third largest object by volume in the main belt" (Ermakov et al. (2014), p. 146), orbiting the sun at a distance of 2.36 AU (Williams et al., 2014c) within 3.63 years (NASA, 2015). Vesta has a rotation period of about 5.3 hours (NASA, 2015); its eccentricity is 0.0889 and its inclination is 7.14° (NASA, 2015). It has a mass of 2.59×10^{20} kg and a

diameter of $569 \times 555 \times 453$ km leading to a bulk density of 3.456 g/cm^3(Russell et al., 2012). Vesta's gravity at the surface is 0.25 m/s^2 (Scully et al., 2014) and its high albedo of 0.4228 (JPL, 2017) makes it possible to see with naked eye (Ermakov et al., 2014). The minimum temperature at the surface yields 180 K and the maximum temperature is 273 K (Tosi et al., 2014).
The northern hemisphere of Vesta has a spherical shape, in opposition to the south pole region which varies highly in altitude due to two major impact events (Combe et al., 2015; Thomas et al., 1997; Zellner et al., 2005; Jaumann et al., 2012; Gaskell, 2012). Vesta is the parent body of more than 900 HEDs (McSween et al., 2011) and the vestoids which were probably caused by impact event(s) on the south pole and show the same composition as Vesta's surface (e.g. Ammannito et al., 2015; Prettyman et al., 2015). HEDs "make up ~6% of the meteorites seen to fall on Earth" (Russell et al. (2012), p. 684).

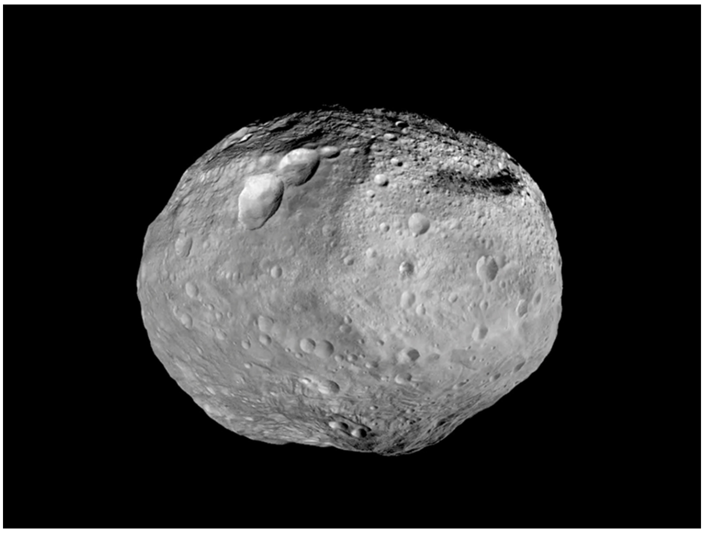

Figure 5.46: Image of Vesta taken by the Dawn spacecraft showing its heavily cratered surface and the non-spherical shape of the southern hemisphere due to two large impacts (NASA JPL, 2013). Credit: NASA/JPL-Caltech/UCLA/MPS/DLR/IDA.

Vesta is differentiated consisting of "a metallic core, an ultramafic mantle, and a basaltic crust" (McSween et al. (2011), p. 142). Its core is very large having a radius of about 110 km (Russell et al., 2014a). Vesta's crust consists of mixtures of eucritic, howarditic, and diogenetic materials (De Sanctis et al., 2012). "Eucrites have high-iron and low-calcium clinopyroxenes, while diogenites have low-iron and no-calcium orthopyroxenes" (Combe et al. (2015), p.54, and references therein). Howardites are mixtures of eucrites and diogenites (Cloutis et al., 2013). Howardits and eucrites dominate the equatorial regions, whereas diogenites are found in the southern hemisphere, especially the Rheasilvia basin (Stephan et al., 2014). The upper crust is eucritic whereas the lower crust is diogenitic (Combe et al., 2015). At the surface fine howarditic regolith is present (Longobardo et al., 2015). "Local occurrences of diogenite-dominated material are generally related to specific impact crater features (e.g., the impact ejecta or crater material)" (Stephan et al. (2014), p. 795).

The differences in brightness on Vesta's surface are very high, having the highest albedo variations of any asteroids where bright and dark material can be found (Russell et al., 2013; Palomba et al., 2014). The dark material is often associated with craters suggesting that is was delivered by impacts (Palomba et al., 2014; Daly and Schultz, 2016) (see Fig. 5.47). Palomba et al. (2014) found more than 220 such dark units and Jaumann et al. (2014) found about 500 impact craters containing dark material. Bright units consist of unaltered soil (Zambon et al., 2014), representing "fresh uncontaminated Vestan pyroxenes from a variety of lithologies exposed from beneath the surface by impacts" (Zambon et al. (2014), p. 73). Hydrogen is also present at Vesta's surface, whereas its abundance is lower at the Rheasilvia basin (O'Brien et al., 2014).

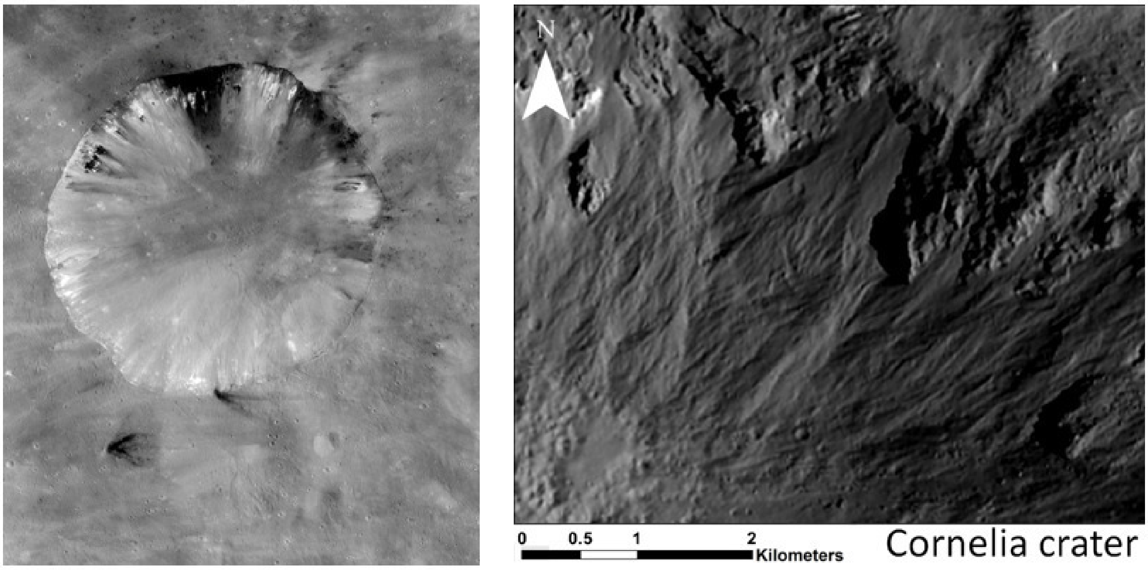

Figure 5.47: Left: Numisia crater on Vesta showing "dark material both on crater walls, and in the material that was ejected by the impact" (NASA/JPL, 2017f). Right: Cutout of Cornelia crater on Vesta showing "long, narrow, sinuous gullies" (NASA/JPL, 2017d). Credit: NASA/JPL-Caltech/UCLA/MPS/DLR/IDA.

The surface of Vesta is heavily cratered, with the most heavily cratered terrains present in the northern hemisphere (Marchi et al., 2012b; Russell et al., 2013) (see Fig. 5.48). Numerous impact craters having different sizes, shapes, ages and morphologies can be seen on the surface (Vincent et al., 2014). There are many more crater chains in the northern hemisphere than in the southern (Carsenty et al., 2014). The oldest impact craters in the northern hemisphere have an age of about 4 Ga (Yingst et al., 2014). Marchi et al. (2012a) showed that the surface is heavily cratered; they catalogued 3457 impact craters with diameters greater than 2 km, 1872 with diameters greater than 4 km, and 12 with diameters greater than 50 km.

The southern hemisphere does not contain as many craters due to the formation of the Rheasilivia and Veneneia basins near the south pole (Marchi et al., 2012b) (see Fig. 5.49 and Fig. 5.50). "The southern hemisphere is dominated by diogenite-rich ejecta, derived from the diogenite-rich lower crust/upper mantle, and the record of smaller impacts has been erased" (Russell et al. (2013), p. 2080). The Veneneia and Rheasilvia basins have diameters of 400 km and 450 km respectively (IAU,

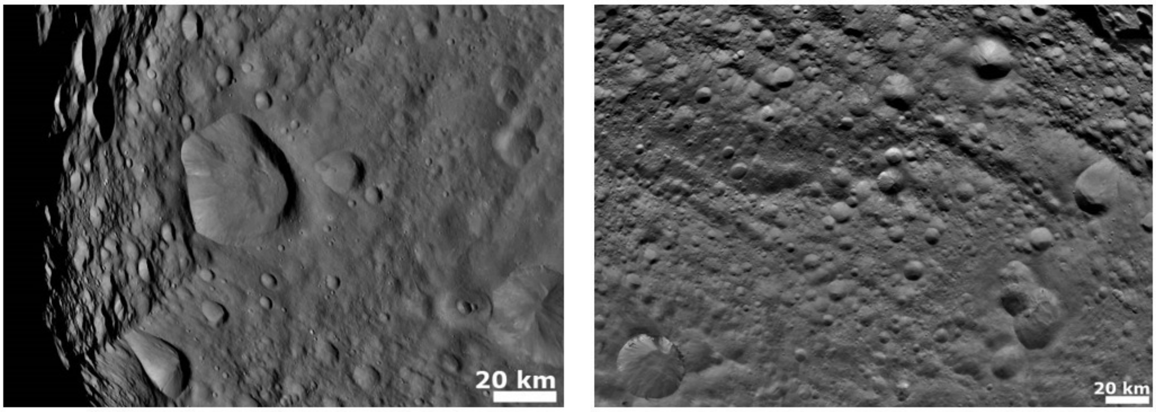

Figure 5.48: Images of Vesta's surface taken by the Dawn spacecraft on 6 August 2011 showing craters including hills and ridges (left) and heavily cratered, old terrain (right) (NASA/JPL, 2017e). Credit: NASA/JPL-Caltech/UCLA/MPS/DLR/IDA.

2017). The older of the two, the Veneneia basin, has a depth of about 12 km while the Rheasilvia basin is about 19 km deep (Schenk et al., 2012b). The central peak of Rheasilvia has a height of 25 km and a width of 180 km (Karimi and Dombard, 2016). The Rheasilvia basin comprises 95% of Vesta's diameter; calculations have shown that about one percent of the satellite's mass was lost due to the impact (NASA Vesta, 2017). Both basins are surrounded by troughs (Buczkowski et al., 2012; Jaumann et al., 2012). Models by de Elía and Di Sisto (2011) showed that the diameter of the impactor that created the 460 km crater was about 40 km or even higher. The age estimations for the two large impact basins by Schmedemann et al. (2014) yield about 3.5 Ga for Rheasilvia and 3.7 Ga for Veneneia.
The formation of the Rheasilvia basin led to the formation of the Divalia fossae at the equator and the formation of the Veneneia crater led to the formation of the Saturnalia fossae in the northern hemisphere (Scully et al., 2014). The Divalia fossa has a length of about 465 km and widths varying from about 22 to 15 km (Buczkowski et al., 2012). The Saturnalia fossa, on the other hand, has an extension of 366 km and widths up to 39 km (Buczkowski et al., 2012). Also, graben and grooves parallel to the Saturnalia Fossa can be seen (Buczkowski et al., 2012).
One of the oldest surface features is Vestalia Terra which is an 80 000 km^2 plateau, older than the Rheasilvia and Veneneia basins (Buczkowski et al., 2014), "with its east-west extent ranging from ~300-430 km and its north-south extent ranging from ~160 to 200 km" (Buczkowski et al. (2014), p. 91).

Most of the impact craters are simple and bowl-shaped (Schenk et al., 2012c) where the transition to complex craters "does not occur till >30 km on Vesta" (Schenk et al., 2016). The transition diameter is at about 28 km on Vesta, but the only crater which shows a classical complex morphology is Rheasilvia (Schenk et al., 2014). Craters having diameters of more than 30 km show "neither simple nor complex" morphologies (Schenk et al., 2014). Schenk et al. (2014) state that "these craters are broadly bowl-shapes with steep inner rimwalls and debris slides but most have a rounded but distinctly noncircular shape" (Schenk et al., 2014). They are also shallower in comparison to simple craters having the same size (Schenk et al., 2014).

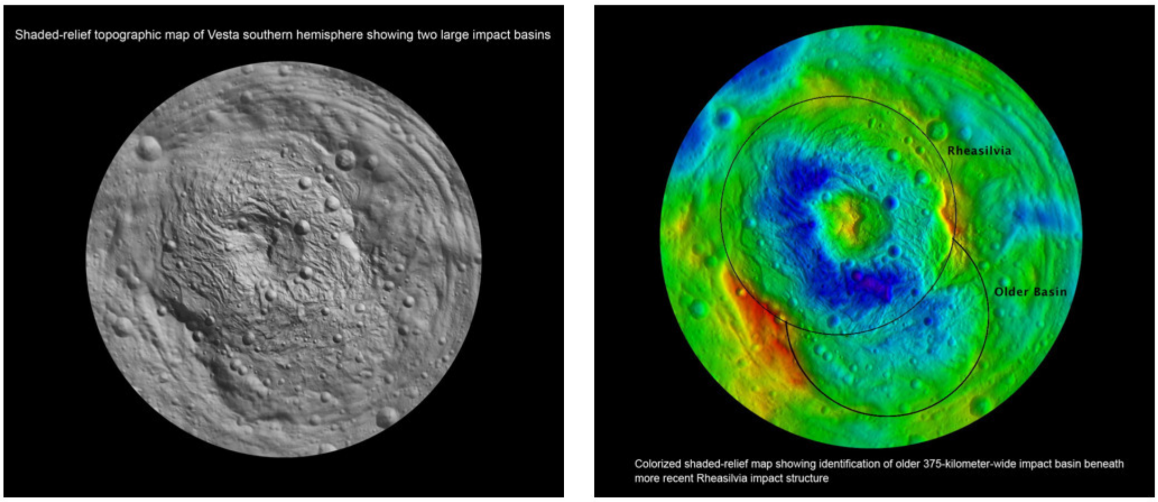

Figure 5.49: Image of Vesta's southern hemisphere showing two large impact basins: The Rheasilvia basin and the Veneneia basin (NASA/JPL, 2017b,c). Credit: NASA/JPL-Caltech/UCLA/MPS/DLR/IDA.

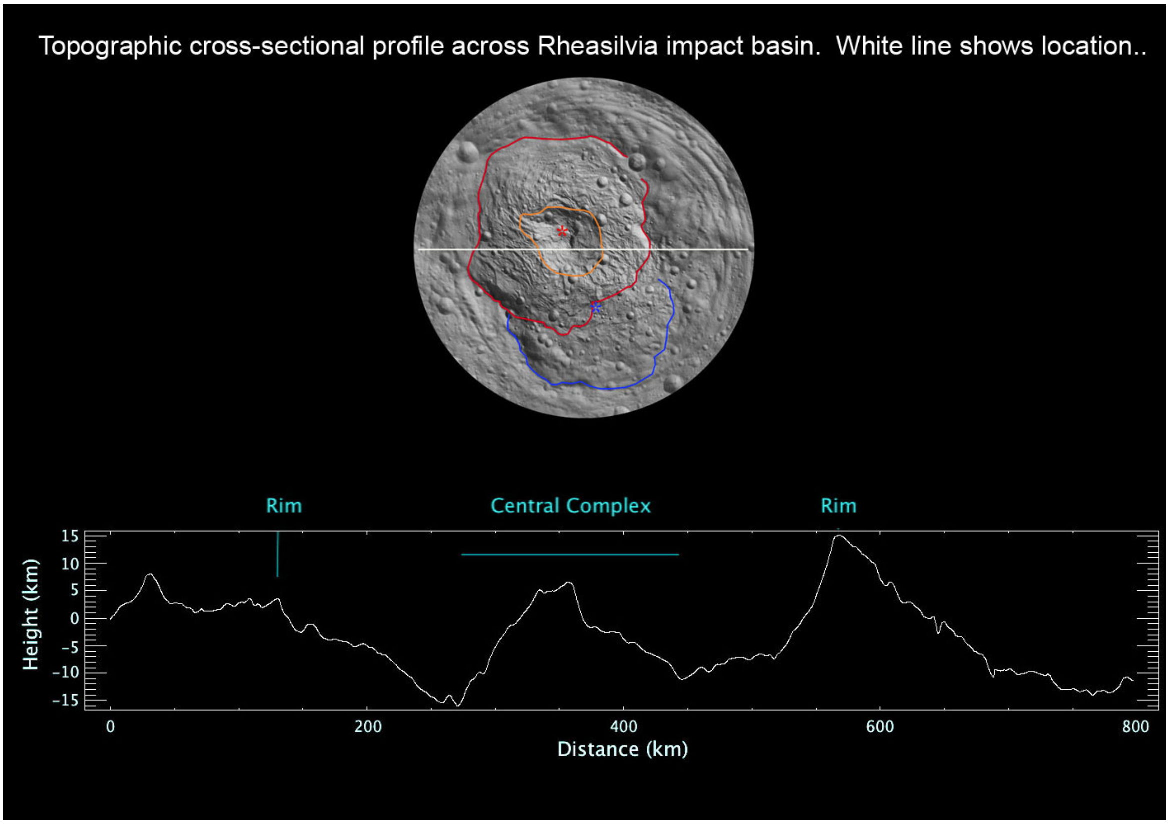

Figure 5.50: Topographic profile across the Rheasilvia impact basin on Vesta (NASA/JPL, 2017a). Credit: NASA/JPL-Caltech/UCLA/MPS/DLR/IDA.

Krohn et al. (2014) detected 2893 asymmetrical craters with diameters from 0.3 to 43 km which "are characterized by a sharp rim on the uphill side and a smooth one on the downhill side" (Krohn et al.

(2014), p. 36) due to their formation on slopes which "prevent the deposition of ejected material in the uphill direction, and slumping material superimposed the deposit of ejecta on the downhill side" (Krohn et al., 2014).

One large, fresh, and probably the best studied impact crater on Vesta is Marcia (see Schenk et al., 2012a,c; Marchi et al., 2014; De Sanctis et al., 2014; Hiesinger et al., 2014b,a; Williams et al., 2014b,a; Ruesch et al., 2014c) which has a diameter of 67.6 km and is located at a latitude of 8.93° and a longitude of 339.55° (IAU, 2017). It has an age of about 60 myr (Marchi et al., 2014). The rim of the crater is not fully circular, its north-south extension is 10 km longer than its east-west extension (De Sanctis et al., 2014). The area in which the Marcia crater is located is rich in H and OH, whereas near the crater itself these elements are not as abundant (De Sanctis et al., 2014; Prettyman et al., 2013). Marcia crater also shows a higher abundance of iron in comparison to its surroundings (Hiesinger et al., 2014a; Prettyman et al., 2013; Yamashita et al., 2013).
Another striking feature is the rayed crater Cornelia which has a diameter of 14.9 km and is located at a latitude of -9.37° and a longitude of 15.57°. Bright and dark material can also be seen here and the crater is not as highly degraded as most of the other craters (Neesemann et al., 2014) (see Fig. 5.47).

As it is believed that the mantle of Vesta consists of olivine, it would have been expected for olivine to be excavated during the two large impact processes on the south pole, but it was not detected in this region. Instead, olivine was found in the northern hemisphere (e.g. Russell et al., 2014b). Crater impact simulations by Jutzi et al. (2013) suggest an excavation depth of between 60 and 100 km at the south pole, whereas the maximum excavation depth in the northern hemisphere due to impacts should only be 20 km (Clenet et al., 2014). Toplis et al. (2012) estimate a crustal thickness of between 15 and 20 km, therefore material of the mantle should be exposed at the south pole.

The first findings of olivine were at the Arruntia and Bellicia craters in the northern hemisphere (Ammannito et al., 2013b; Thangjam et al., 2014). At the Arruntia and Bellicia craters the abundance of olivine is greater than 50% (Ammannito et al., 2013b,a) and "the exposures are located on the slopes of outer/inner crater walls, on the floor of Arruntia, in the ejecta, as well as in nearby fresh small impact craters" (Thangjam et al. (2014), p. 1831). "The olivine rich materials are distributed in an area of 60 km^2 included approximately in the region between 33-53°N and 43-56°E close to the Bellicia crater, whereas in the Arruntia region olivine-rich materials are spread in 40 km^2 region between 28-43°N and 70-83°E" (Palomba et al. (2015), p. 130). "Arruntia and Bellicia are the most olivine-rich regions detected to date" (Palomba et al. (2015), p. 132). At the Arruntia and Bellicia craters, olivine is mixed with howardite, which is in contrast to meteorites where olivine is associated with diogenite (Ammannito et al., 2013b).
Further olivine-rich locations on Vesta have been found (e.g. Ruesch et al., 2014b; Palomba et al., 2015). "Other new and important olivine rich areas are located farther toward the north: in Pomponia there are 35 km^2 of olivine-rich materials distributed around 64-70°N and 114-124°E, in Albana another 20 km^2 between 58-65°N and 40-86°E" (Palomba et al. (2015), p. 130). Over all, Ruesch et al. (2014b) detected olivine in 13 different locations, whereas the abundance in the newly found locations is lower than at the former locations. The impact craters where olivine was found in the

ejecta or crater walls have diameters up to 50 km and “are morphologically fresh and younger than 600-1000 Ma” (Ruesch et al. (2014b), p. 2103). Ruesch et al. (2014b) also found olivine in the ejecta of the Rheasilvia basin but not on the floor or the central mound.

One possible explanation for the absence of olivine in or near the two large impact basins of the south pole is that the crust there is thicker than expected, as suggested by Clenet et al. (2014) which is in contrast to magmaocean crystallization models. Other solutions might be that the upper mantle is composed of orthopyroxene and not of olivine, “that the mantle rocks in Rheasilvia experienced impact melting, so that crystalline olivine is no longer present” (McSween et al. (2013), p. 342) or that the Vestoids contain the missing olivine (McSween et al., 2013). Le Corre et al. (2015) propose that the olivine in the northern hemisphere was delivered by olivine-rich meteorites. Another problem is that concentrations lower than 25 vol.% olivine are difficult to detect (McSween et al., 2013). Ruesch et al. (2014b) point out that “olivine grains are probably fractured, broken, and dispersed in a pyroxene-dark material mixture” (Ruesch et al. (2014b), p. 2100) due to space weathering, making them difficult to detect. Six olivine-rich craters are older than Arruntia and therefore the abundance of olivine at these craters is lower due to space weathering (Ruesch et al., 2014b). As there are two old impact basins near the Arruntia crater named Varronilla and Caesonia, there could be a relationship between these old basins and the occurrence of olivine-rich material (Ruesch et al., 2014b).

6 Studies of Polygonal Impact Craters (PICs) on Saturnian Satellites

6.1 PICs on Rhea

On Rhea 61 of the 128 approved impact craters of the IAU/NASA/USGS Planetary Database were identified as polygonal (see Tab. 6.2), yielding a percentage of about 48%. Around two thirds of them are simple craters.
In the IAU/NASA/USGS Planetary Database there are 48 impact craters listed with unknown diameters which have been measured by the author using the ISIS visualization tool "qview". 24 of these are polygonal (Aanin, Adjua, Agunua, Ameta, Arunaka, Con, Faro, Haik, Haoso, Heller, Iraca, Izanami, Khado, Kumpara, Lowa, Malunga, Mubai, Num, Pan Ku, Pedn, Qat, Tika, Uku, and Xamba) and are marked as (*) in the corresponding table.

Fig. 6.51 shows an example of a PIC on Rhea named Agunua including its marked straight rims. The crater is located at a latitude of 63.3° and a longitude of 66.2° and has a diameter of about 60 km (IAU/NASA/USGS, 2016).

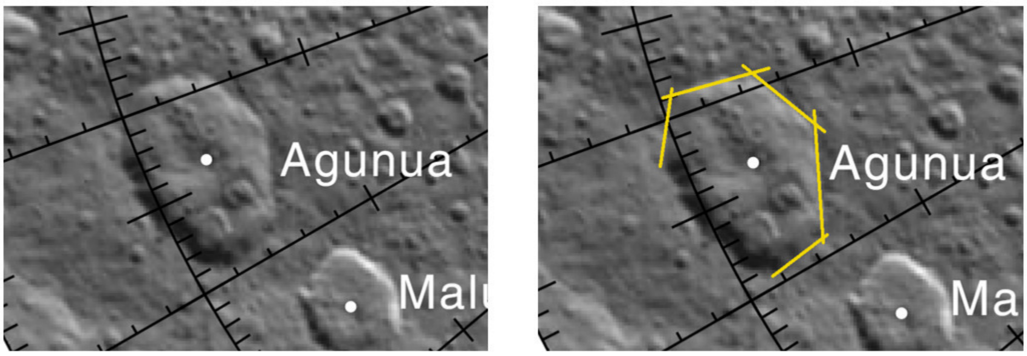

Figure 6.51: PIC Agunua on Rhea which has a diameter of about 60 km and is located at a latitude of 63.3° and a longitude of 66.2° (left), including its marked straight rims (right). Credit: IAU/NASA/USGS (2016).

Nr.	Crater	Diameter (km)	Centre Longitude (°)	Centre Latitude (°)
1	Aananin	52*	34.9	339.9
2	Abassi	87.2	-21.3	146.5
3	Adjua	46*	40.2	118.9
4	Agunua	60*	63.3	66.2
5	Ambat	42.9	-76.4	301.7
6	Ameta	47*	53.3	21.9
7	Amma	31.4	-26.4	282.7
8	Amotken	64.6	0.7	202.7

Nr.	Crater	Diameter (km)	Centre Longitude (°)	Centre Latitude (°)
9	Arunaka	40*	-15.3	22.1
10	Awonawilona	49.8	-37.3	150.3
11	Con	77.5*	-25.8	12.7
12	Dangun	77.5	7.2	208
13	Dotet	40.4	-45.9	204.7
14	Enkai	48.4	38	246.3
15	Faro	63.5*	45.3	114
16	Fatu	88	7.7	176.1
17	Gborogboro	62.5	-12.7	162.2
18	Gucumatz	68.6	37	175.8
19	Haik	75*	-36.6	29.3
20	Haoso	72.5*	8.3	12.5
21	Heller	75*	10.1	315.1
22	Inmar	54.8	-2.3	301.6
23	Iraca	50*	39.4	112.1
24	Itciai	39.2	-17.8	349
25	Izanami	70*	-46.3	313.4
26	Karusakaibo	43.4	-14.2	220.7
27	Khado	44*	41.6	359.1
28	Kuksu	34.6	25.3	288.7
29	Kuma	50	10	277.2
30	Kumpara	49*	9.6	327.1
31	Ligoupup	78.8	-14.5	46.2
32	Lowa	35*	40.9	16.6
33	Maheo	29.8	31.6	281.7
34	Malunga	36*	65.1	56.2
35	Mubai	38*	55.8	20.2
36	Ndu	33.4	-22.4	291.3
37	Nishke	74.2	3.8	49
38	Num	48*	24	92.7
39	Nzame	119.4	9	24.9
40	Obatala	67.2	-1.1	269.7
41	Pachacamac	46.8	-23.4	83.7
42	Pan Ku	41*	65.7	107.7
43	Pedn	36*	46	351.7
44	Pokoh	45.2	-71.7	326.4
45	Pouliuli	59.8	-16.9	284.4
46	Puntan	33	33.9	292.4
47	Purusa	96.7	-21.2	167.8
48	Qat	102.5*	-23.8	351.6
49	Quwai	38.8	19.6	66
50	Samni	101.4	-47.7	90.7

Nr.	Crater	Diameter (km)	Centre Longitude (°)	Centre Latitude (°)
51	Talapas	51.6	-16.7	341.8
52	Tane	82.6	-12.5	57.4
53	Tasheting	60.8	-59	55.5
54	Tika	57*	25.1	84.1
55	Tuwale	59.6	-78	242.4
56	Uku	56*	78.7	95.5
57	Wak	57.8	29.6	194.3
58	Woyengi	43	13.7	294.5
59	Xamba	100*	2.1	349.7
60	Xowalaci	60	2.4	56.3
61	Zicum	76.8	-50.9	111.2

Table 6.2: Identified polygonal impact craters (PICs) on Rhea from the IAU/NASA/USGS Planetary Database. The values for crater diameter, centre latitude, and centre longitude are taken from the IAU/NASA/USGS Planetary Database. Unknown diameters of 24 PICs were measured by the author and are marked as (*).

Table 6.3 shows the values of the measured diameters of 24 non-polygonal impact craters included in the IAU/NASA/USGS Planetary Database. The data of the coordinates was taken from the IAU/NASA/USGS Planetary Database.
The found PICs have two to six straight crater rim segments with a mean number of 2.9. More than two-thirds of the PICs have two or three straight rims while only few are pentagonal or hexagonal. The exact number of straight crater rim segments can be seen in Figure 6.52.

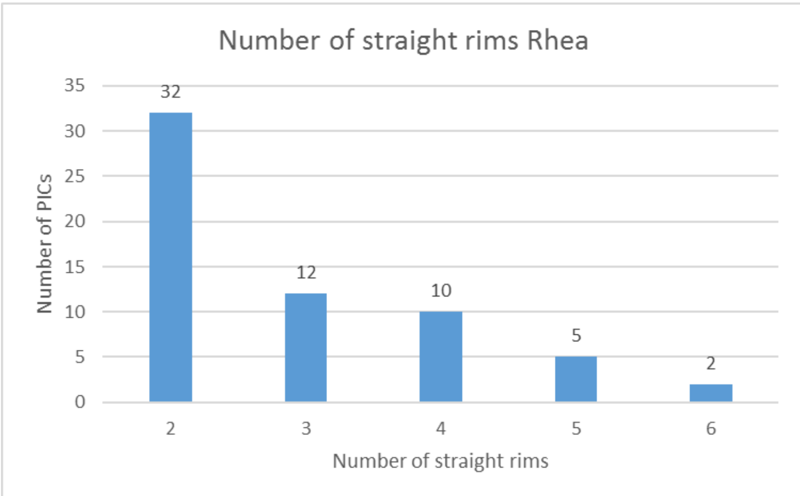

Figure 6.52: There are thirty-two polygonal impact craters (PICs) with two crater rim segments, twelve PICs have three crater rim segments, ten craters have four straight rims, five craters have five straight rims, and two craters have six straight crater rim segments.

The angles between the straight crater rim segments range from 85° to 150° with a mean angle of about 121°.

Nr.	Crater	Diameter (km)	Centre Longitude (°)	Centre Latitude (°)
1	Atum	67.5	-47.1	1.1
2	Bulagat	72.5	-38.2	15.2
3	Bumba	127.5	63.1	50.4
4	Burkhan	32.5	66.8	310.6
5	Djuli	105	-31.2	46.7
6	Ellyay	105	71.4	91.8
7	Izanagi	240	-49.4	310.2
8	Jumo	37	52.8	66.5
9	Karora	55	5.9	20.1
10	Kiho	97.5	-11.1	358.7
11	Leza	75	-21.8	309.2
12	Manoid	35	29.5	8.5
13	Melo	75	-53.2	7.1
14	Ormazd	145	52.5	58.5
15	Sholmo	48	12	346.4
16	Taaroa	52	16.5	95.5
17	Thunupa	49	45.6	21.3
18	Tirawa	390	34.2	151.7
19	Tore	2.85	0	340
20	Torom	48	-72.5	343
21	Whanin	57	66.9	115
22	Wuraka	45	25.1	4
23	Xu	63	55	71.9
24	Yu-Ti	70	50.1	81.5

Table 6.3: Measured diameters for 24 non-polygonal impact craters from the IAU/NASA/USGS Planetary Database. Coordinate data was taken from the database.

The diameters of all approved craters on Rhea are between about 2.9 km and 480.0 km with a mean diameter of about 69.8 km. The diameters of non-polygonal impact craters range from 2.9 km to 480.0 km with an average value of about 80.1 km while the diameters of PICs only range from 29.8 km to 119.4 km with a mean value of about 58.5 km. The diameter range in which PICs are most common is about $7 \times D_{tr}$.

Figure 6.53 shows the distribution of diameters for all approved craters on Rhea. Blue bar sections show impact craters with given diameters while violet bar sections correspond to craters whose diameters were measured by the author. The comparison between the diameters of non-polygonal impact craters (ICs) to polygonal impact craters (PICs) can be seen in Figure 6.54.

To determine whether there are areas with a higher abundance of PICs than their surroundings, a plot showing the distribution of non-polygonal impact craters (ICs) and polygonal impact craters (PICs) on the surface of Rhea has been made (see Fig. 6.55). The black boxes represent the non-polygonal impact craters (ICs) and the red boxes show the polygonal impact craters (PICs) from the database. No significant pattern regarding the distribution between PICs and ICs can be seen.

The distribution of non-polygonal impact craters (blue) and polygonal impact craters (red) underly-

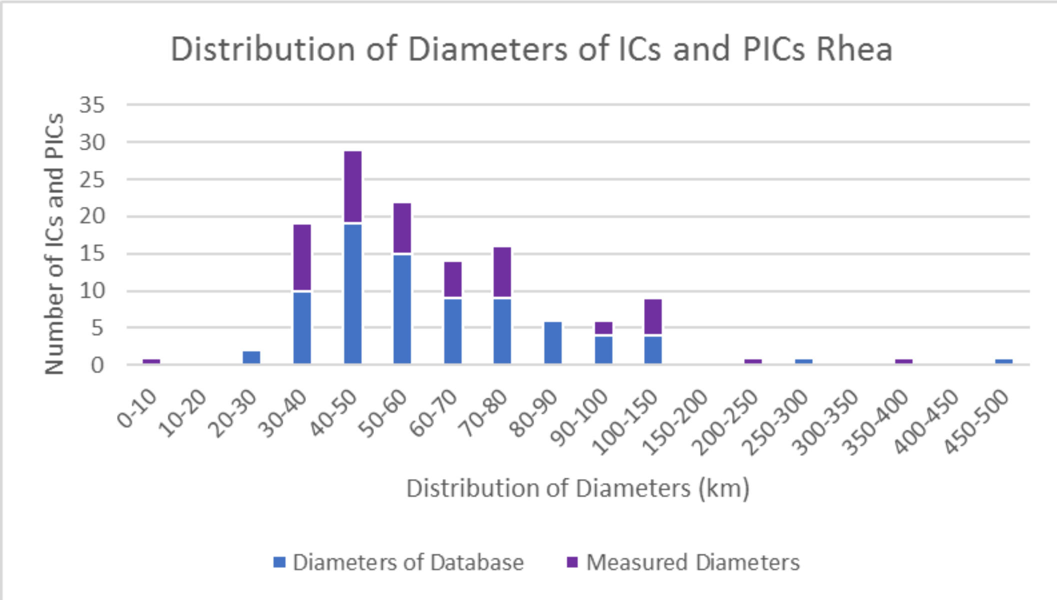

Figure 6.53: Distribution of diameters of all approved craters on Rhea, according to values for diameters from the IAU/NASA/USGS Planetary Database (blue bar sections); missing values (violet bar sections) were measured by the author. The diameters of all approved impact craters on Rhea range between about 2.9 km and 480.0 km, yielding a mean diameter of about 69.8 km.

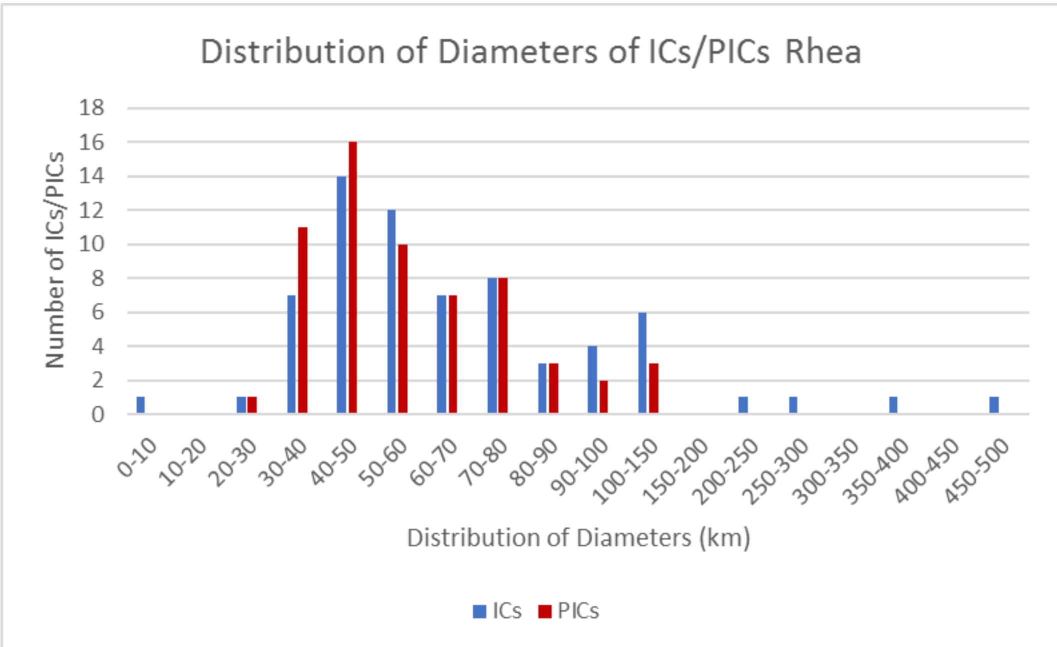

Figure 6.54: Distribution of diameters of non-polygonal impact craters (ICs, blue) and polygonal impact craters (PICs, red) on Rhea. Values for diameters were taken from the IAU/NASA/USGS Planetary Database, missing diameters were calculated by the author. The diameters of ICs are between 2.9 km and 480 km (mean diameter: 80.1 km), while the diameters of PICs only range from 29.8 km to 119.4 km with a mean diameter of about 58.5 km.

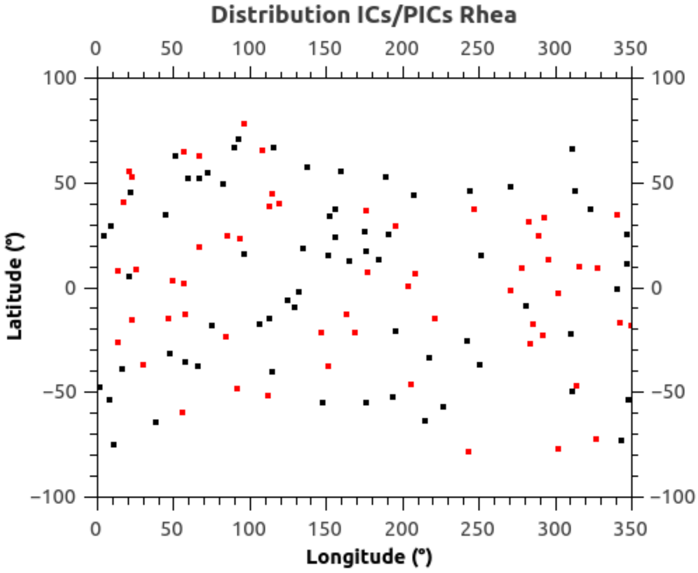

Figure 6.55: Distribution of non-polygonal impact craters (ICs, black boxes) and polygonal impact craters (PICs, red boxes) on the surface of Rhea of all approved craters of the IAU/NASA/USGS Planetary Database.

ing a surface map of the equator and the north and south pole regions can be seen in Figures 6.56 and 6.57.

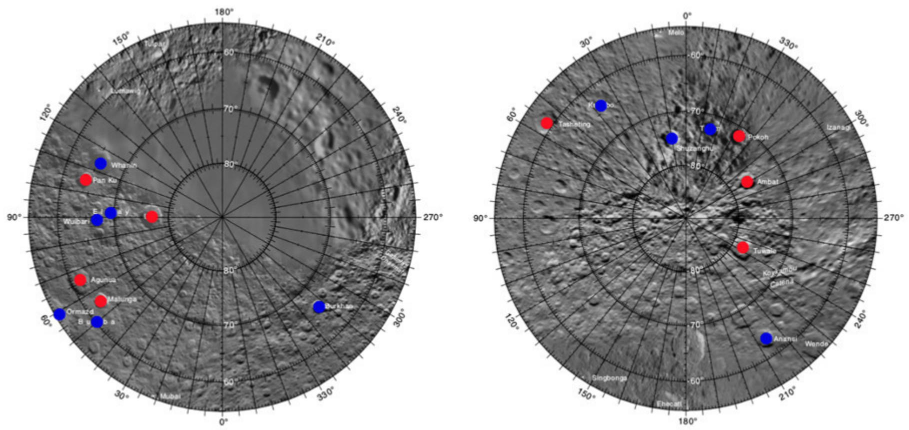

Figure 6.56: Distribution of approved craters of the IAU/NASA/USGS Planetary Database on the north pole (left) and south pole (right) on Rhea. Blue circles represent non-polygonal impact craters (ICs) while red circles show polygonal impact craters (PICs). No concentration of ICs or PICs can be seen.

Also, the relation between the diameter and the number of straight crater rim segments was studied (see Fig. 6.58), but no correlation was found.

Due to the fact that there are many more unapproved impact craters than approved ones, all impact craters between a latitude of -60° to 60° that are large enough to be differentiated whether polygonal

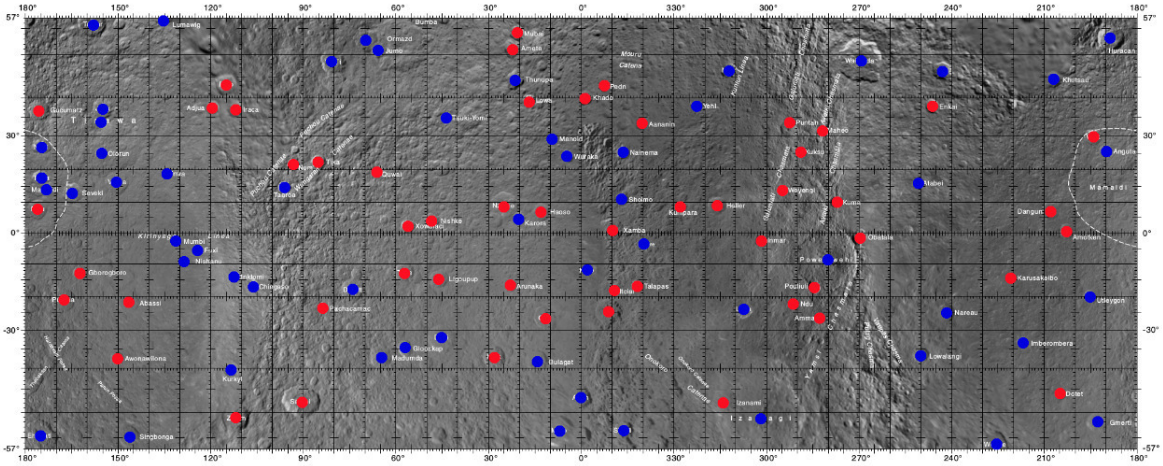

Figure 6.57: Distribution of approved craters from the IAU/NASA/USGS Planetary Database in the equatorial region of Rhea. Blue circles represent non-polygonal impact craters (ICs) while red circles show polygonal impact craters (PICs). No concentration of ICs or PICs can be seen.

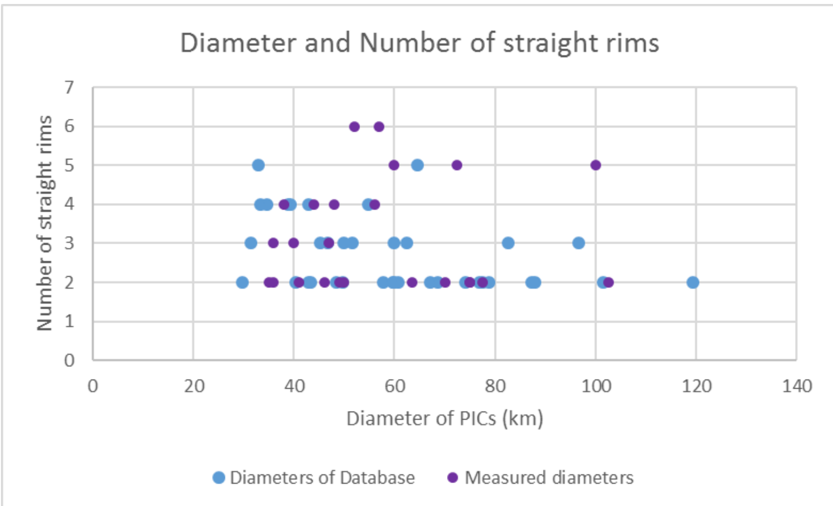

Figure 6.58: Number of straight crater rim segments as a function of the diameter of PICs on Rhea. Blue dots shows craters with diameters from the IAU/NASA/USGS Planetary Database while violet dots show craters whose diameters were measured by the author.

or not were examined to check whether the percentage of polygonality resulting from only approved craters in this study represents the total crater population.

Over all, 86 more PICs and 123 more non-polygonal impact craters were found. Including the former approved PICs and non-polygonal impact craters, this leads to about 44% of impact craters being polygonal. All examined impact craters were marked in the map of the IAU/NASA/USGS Planetary Database (see Fig. 6.59).

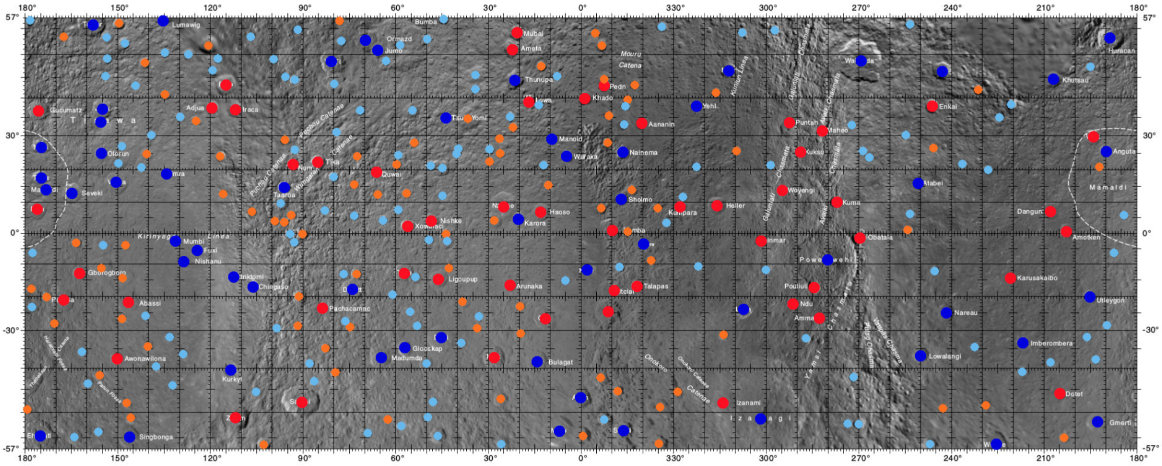

Figure 6.59: Polygonal impact craters (orange, red) and non-polygonal impact craters (light blue, blue) on the surface of Rhea. Red dots show approved PICs and orange dots show additional ones. Blue dots show approved non-polygonal craters and the light blue represents additional non-polygonal craters. Over all, there are 53 approved PICs, 86 unapproved PICs, 57 approved non-polygonal impact craters, and 123 additional unapproved non-polygonal impact craters on Rhea.

6.2 PICs on Dione

On Dione, 43 of the 73 approved impact craters in the IAU/NASA/USGS Planetary Database were considered as polygonal, representing 59%. More than 65% of these are simple impact craters. All found PICs, including their diameters and coordinates, can be seen in Table 6.4. The values for the diameter, centre latitude, and centre longitude are taken from the IAU/NASA/USGS Planetary Database.

Fig. 6.60 shows the PIC Assaracus on Dione which has a diameter of about 60 km and is located at a latitude of 32.65° and a longitude of 8.79°; its marked straight rims are included.

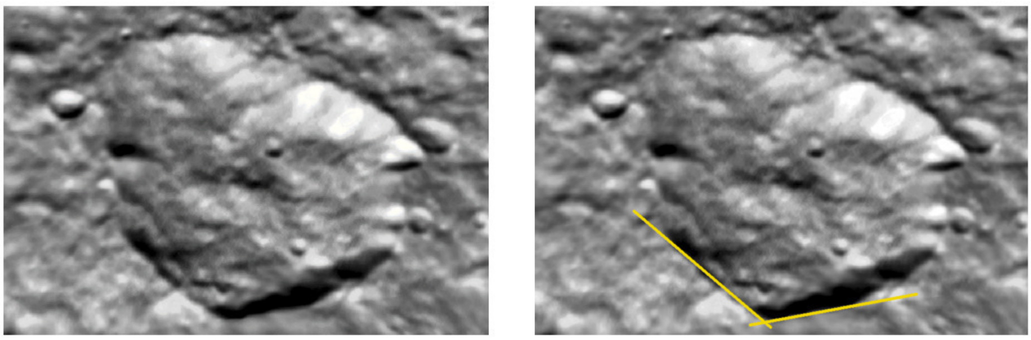

Figure 6.60: PIC Assaracus on Dione which has a diameter of about 60 km and is located at a latitude of 32.65° and a longitude of 8.79° (left), including its marked straight rims (right). Credit: IAU/NASA/USGS (2016).

The number of straight crater rim segments ranges from two to seven with more than half of the craters having two or three straight rim segments, giving a mean number of 3.4. Only a few craters

Nr.	Crater	Diameter (km)	Centre Longitude (°)	Centre Latitude (°)
1	Acestes	108	50.1	243.37
2	Adrastus	38.5	-61.66	46.57
3	Alcander	120	-52.89	295.49
4	Allecto	106	-7.73	224.56
5	Amastrus	62.4	-9.96	237.03
6	Amycus	27.3	-37.52	88.62
7	Anchises	47	-34	65
8	Anna	14.2	-63.38	89.96
9	Antenor	81	-7	11.54
10	Assaracus	60	32.65	8.79
11	Caieta	50	-24.71	79.63
12	Camilla	31.9	-4.36	60.61
13	Catillus	42.2	-2.38	275.3
14	Coras	43	0.39	268.45
15	Cretheus	29	-43.35	88.53
16	Dido	122	-23.97	18.82
17	Entellus	63	-10.93	210.54
18	Euryalus	35	-74.36	0
19	Fadus	47	-35.94	225.18
20	Galaesus	79	46.77	296.25
21	Haemon	65.22	84.33	276.31
22	Halys	35.2	-59.17	53.72
23	Herbesus	58.4	34.68	156.11
24	Ilia	52.4	-0.5	346.27
25	Italus	35.7	-18.47	76.41
26	Lamyrus	61	53.67	255.61
27	Lausus	23.5	34.81	22.76
28	Magus	45.8	18.44	24.35
29	Massicus	39	-35	55.39
30	Mezentius	51	19.16	183
31	Oebalus	35.7	44.47	351.6
32	Pagasus	67	-3	241
33	Prytanis	96	-46.25	287.4
34	Remus	62	-13.58	31.9
35	Ripheus	34	-56.47	36.8
36	Romulus	90.7	-8.15	26.85
37	Sabinus	88	-43.65	186.66
38	Sagaris	53	4.93	104.2
39	Silvius	74	-32.7	332.26
40	Telon	39.7	-16.2	97.2
41	Thymber	27.29	14	309.15
42	Tiburtus	59	29.11	189.73
43	Volcens	74	-13.84	268.51

Table 6.4: Found PICs on Dione of all approved craters of the IAU/NASA/USGS Planetary Database with their diameter, centre latitude, and centre longitude. Values of the diameter, centre latitude, and centre longitude are taken from IAU/NASA/USGS Planetary Database.

are hexagonal or pentagonal. There are fifteen craters that show two straight rim segments, ten PICs have three straight segments, nine craters have four straight segments, five craters have five straight segments, two craters have six straight rims, and two craters have seven straight segments. Figure

6.61 shows the exact number of straight crater rim segments of all the approved craters on Dione.

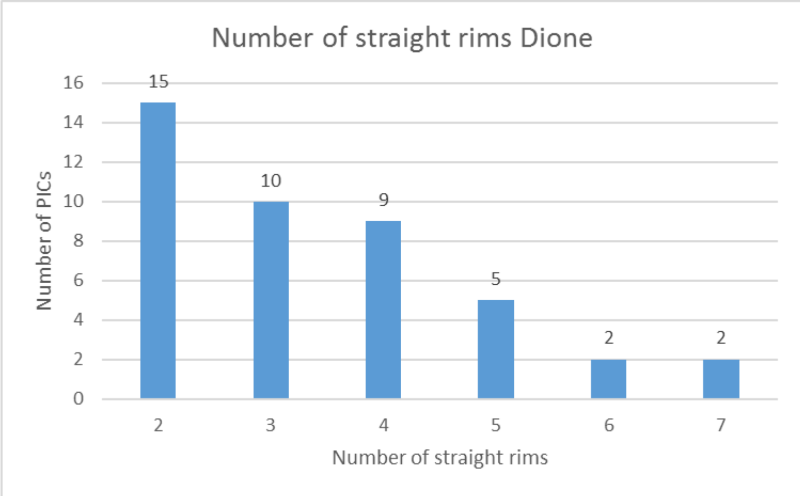

Figure 6.61: Number of straight crater rim segments on Dione. There are fifteen PICs that show two crater rim segments, ten show three crater rim segments, nine show four straight segments, and five show five straight segments. Only two craters have six straight segments and two have seven straight crater rim segments. More than half of the polygonal impact craters on Dione have two or three straight rim segments.

The angle between the straight crater rims ranges from 89° to 148°, giving a mean value of about 124°.

The diameters of all approved craters on Dione have values from 11.9 km to 350 km with a mean diameter of about 63.0 km. The diameters of non-polygonal impact craters on Dione range from 11.9 km to 350 km with a mean diameter of about 70.9 km. The diameters of PICs only, however, lie between 14.2 km and 122 km and the mean diameter is about 57.5 km. Assuming a transition diameter of about 12 km on Dione, the diameter range in which PICs are most common is about $5 \times D_{tr}$. Figure 6.62 shows the distribution of diameters of all approved craters on Dione. The comparison between the diameters of normal impact craters (ICs) to polygonal impact craters (PICs) can be seen in Figure 6.63.

Figure 6.64 shows the distribution of non-polygonal impact craters (black boxes) and polygonal impact craters (red boxes) on the surface of Dione. The coordinates were taken from the Planetary Database. Regarding the distribution of these two crater types on the surface, no significant pattern could be found.

To explore the distribution of non-polygonal impact craters and polygonal impact craters in a better way, a surface map of the north and south pole regions and the equatorial region from the IAU/NASA/USGS Planetary Database was used and all approved craters were marked (see Fig. 6.65 and Fig. 6.66). The blue dots show non-polygonal impact craters and the red dots represent PICs.
Figure 6.67 shows crater size as a function of the number of straight rim segments on Dione. No correlation between the diameter of polygonal impact craters (PICs) and the number of straight crater rim segments was found.

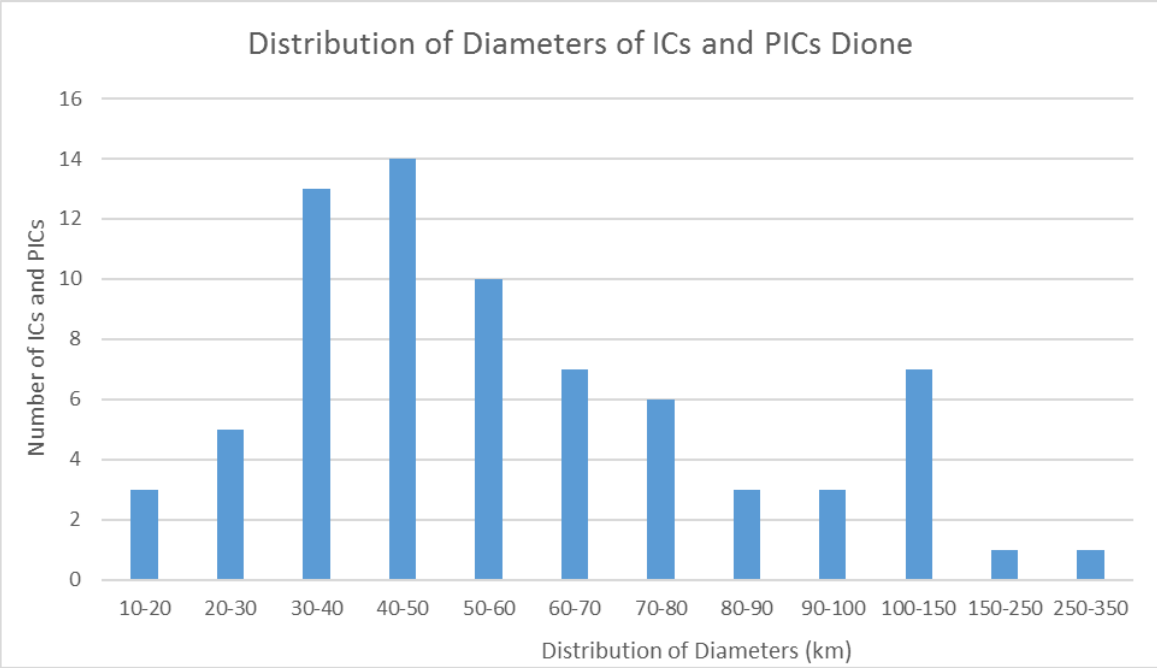

Figure 6.62: Distribution of diameters of all approved craters on Dione, according to values for the diameters from the IAU/NASA/USGS Planetary Database. The diameters of craters range from 11.9 km to 350 km, giving a mean diameter of about 63.0 km.

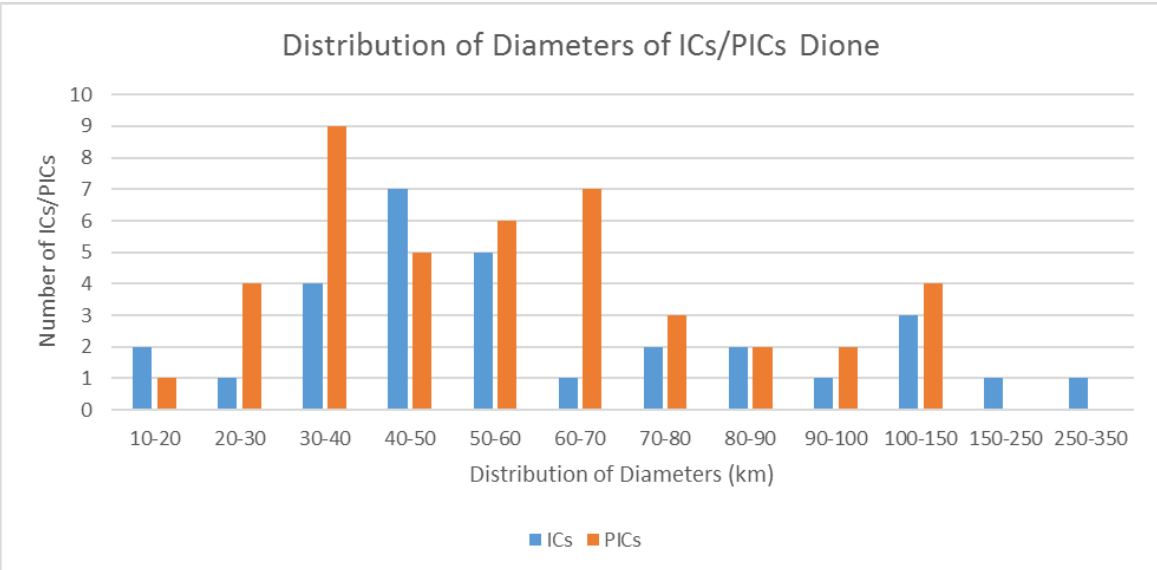

Figure 6.63: Distribution of diameters of non-polygonal impact craters (ICs) and polygonal impact craters (PICs) on Dione. Values for the diameters were taken from the IAU/NASA/USGS Planetary Database. The diameters of ICs range from 11.9 km to 350 km (mean diameter: 70.9 km) while the diameters of PICs only range from 14.2 km to 122 km, giving a mean diameter of about 57.5 km.

As there are many more unapproved impact craters than approved ones, all impact craters between

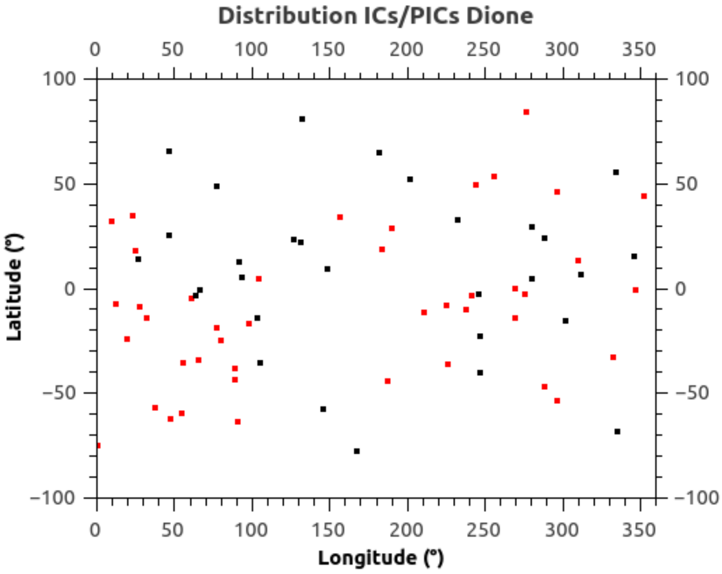

Figure 6.64: Distribution of non-polygonal impact craters (black boxes) and polygonal impact craters (red boxes) on Dione's surface. No significant distribution pattern was found.

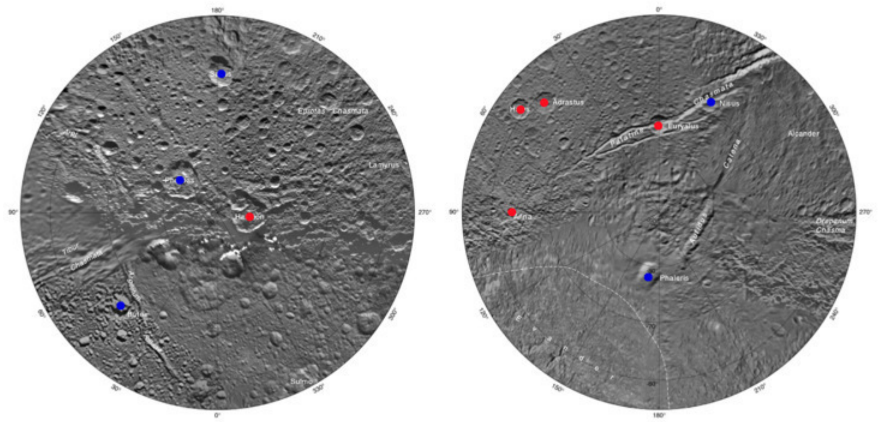

Figure 6.65: Distribution of approved craters of the IAU/NASA/USGS Planetary Database on the north pole (left) and the south pole (right) on Dione. All approved non-polygonal craters (blue circles) and polygonal craters (red circles) were marked.

a latitude from -60° to 60° that are large enough to be differentiated whether polygonal or not were examined to check whether the percentage of polygonality resulting from only approved craters in this study represents the crater population of this body. Over all, 136 more PICs and 146 more non-polygonal impact craters were found. Including the former approved PICs and non-polygonal impact craters, this leads to about 50% of impact craters being polygonal. All examined impact craters were marked on the map of the IAU/NASA/USGS Planetary Database (see Fig. 6.68).

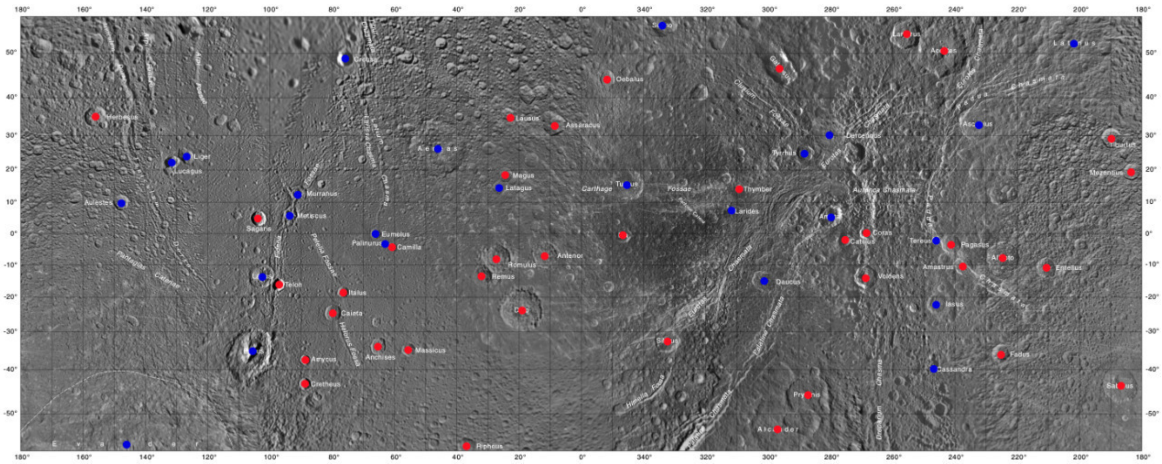

Figure 6.66: Distribution of approved craters of the IAU/NASA/USGS Planetary Database in the equatorial region on Dione. All approved non-polygonal craters (blue circles) and polygonal craters (red circles) were marked.

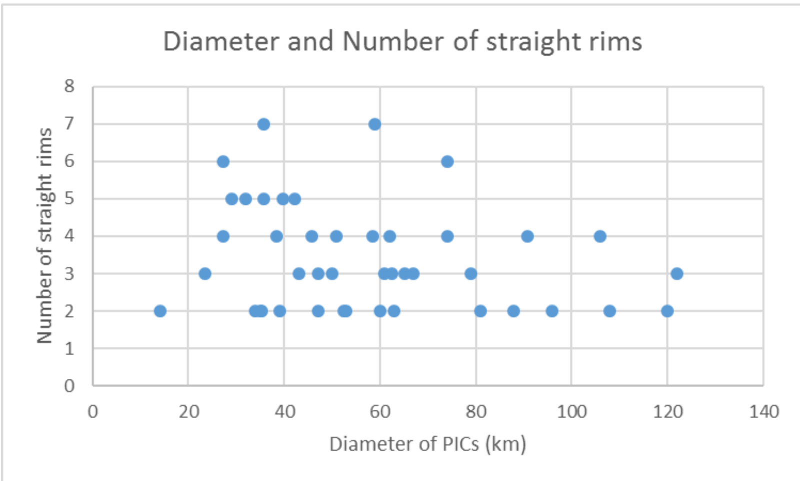

Figure 6.67: Number of straight crater rim segments as a function of crater size on Dione. No correlation between the diameter of polygonal impact craters and the number of straight rims was found.

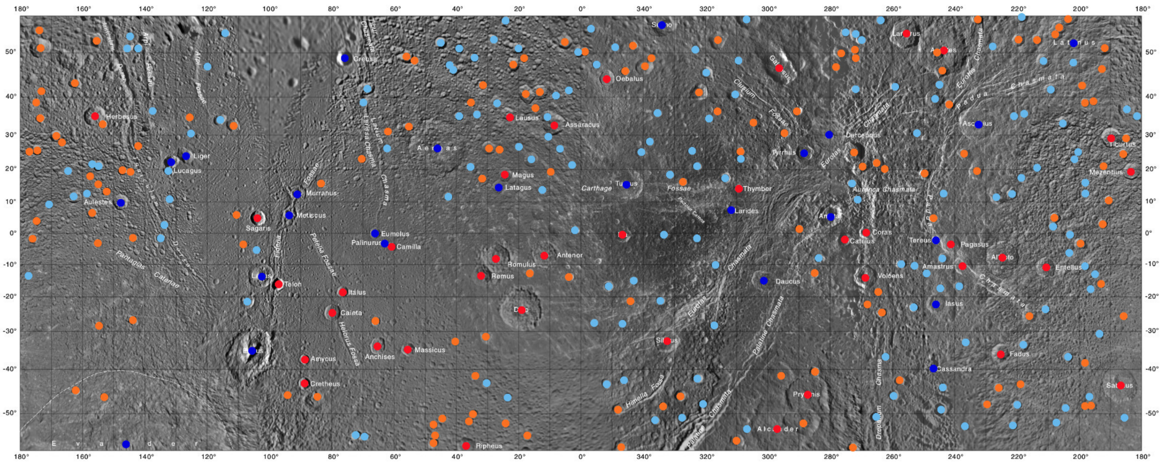

Figure 6.68: Polygonal impact craters (orange, red) and non-polygonal impact craters (light blue, blue) on Dione's surface. Red dots show approved PICs and orange dots mark additional ones while blue dots represent approved non-polygonal craters and the light blue dots show additional non-polygonal craters. Over all, there are 38 approved PICs, 136 unapproved PICs, 25 approved non-polygonal impact craters, and 146 additional unapproved non-polygonal impact craters on Dione.

6.3 PICs on Tethys

On Tethys, 17 impact craters of the 50 approved craters in the IAU/NASA/USGS Planetary Database were identified as polygonal, therefore, about 37% of all approved craters are PICs. More than two thirds of all PICs are simple craters. All found PICs are listed in Table 6.5, including their diameters and coordinates, obtained from the IAU/NASA/USGS Planetary Database.

One example of a PIC on Tethys is the crater Icarius which has a diameter of 54.4 km and is located at a latitude of -5.89° and a longitude of 305.85° (see Fig. 6.69).

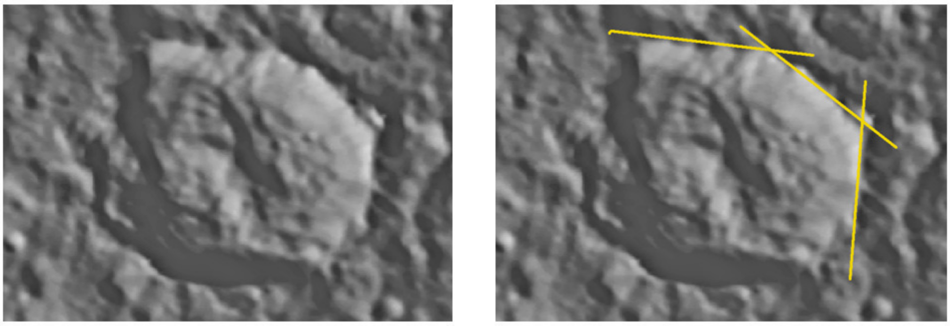

Figure 6.69: PIC Icarius on Tethys which has a diameter of 54.4 km and is located at a latitude of -5.89° and a longitude of 305.85° (left), included are its marked straight rims (right). Credit: IAU/NASA/USGS Planetary Database (2016).

Nr.	Crater	Diameter (km)	Centre Longitude (°)	Centre Latitude (°)
1	Achilles	58.6	0.6	324.38
2	Ajax	88	-28.41	282
3	Alcinous	50	30.31	212.61
4	Antinous	138	-59.89	286.15
5	Arete	13	-4.67	299
6	Euanthes	33	7.86	238.91
7	Eupithes	22.3	18.71	171.21
8	Eurylochus	44.8	-5.07	27.68
9	Eurymachus	38.4	-35.65	65
10	Halius	29.5	44.4	4.96
11	Icarius	54.4	-5.89	305.85
12	Irus	26.5	-27	244.81
13	Leocritus	12.5	21.53	118.66
14	Naubolos	54.5	-72.19	305.18
15	Neleus	37.6	-19.38	25.72
16	Odysseus	445	32.82	128.89
17	Ormenus	39.8	-20.39	43.85

Table 6.5: Found polygonal impact craters (PICs) on Tethys including their diameters, centre latitudes, and centre longitudes. Values for the crater diameters and the coordinates were taken from the IAU/NASA/USGS Planetary Database.

The number of straight rim segments ranges from two to six, with most of the craters having two or three straight rims, giving a mean number of 3.1. More than half of the PICs have two or three straight rims while hexagonal or pentagonal shapes are rare. There are seven craters having two straight rims, four craters having three straight rims, four craters having four rims, one crater having five, and one having six straight crater rim segments (see Fig. 6.70).

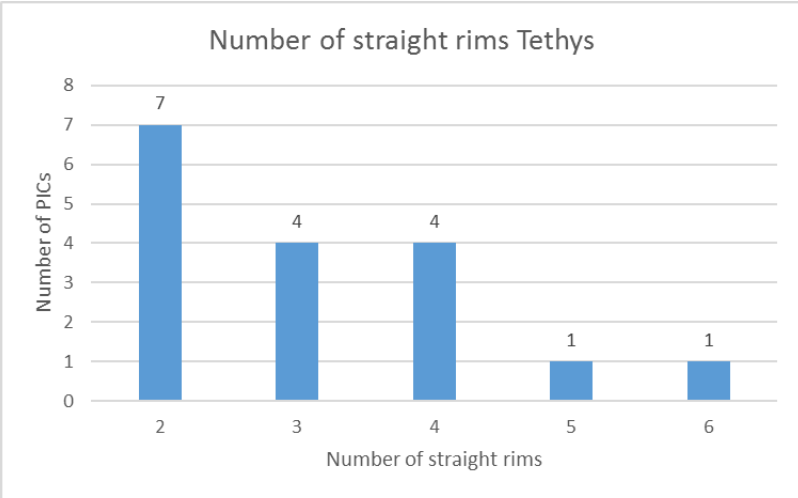

Figure 6.70: Number of straight crater rim segments on Tethys. More than half of the polygonal impact craters (PICs) have two or three straight rims. There are seven PICs that show two crater rim segments, four PICs show three crater rim segments, four PICs show four straight segments, one PIC shows five straight rims, and one crater shows six straight crater rim segments.

The angle between the straight rims is between 97° and 142°, resulting in a mean angle of about 123°.

The diameters of all approved craters on Tethys lie between 11.8 km and 445.0 km with a mean diameter of about 73.5 km. The diameters of non-polygonal impact craters on Tethys range from 11.8 km to 320.0 km which gives a mean diameter of about 75.5 km, while the diameters of PICs are between 12.5 km and 445 km which gives a mean diameter of about 69.8 km. The diameter range in which PICs are most common is about $3 \times D_{tr}$. Figure 6.71 shows the distribution of diameters for all approved craters on Tethys. The comparison between the diameters of non-polygonal craters (ICs) and polygonal impact craters (PICs) can be seen in Figure 6.72.

The distribution of non-polygonal impact craters (black boxes) and polygonal impact craters (red boxes) on the surface of Tethys can be seen in Figure 6.73. No significant pattern or higher abundance of ICs or PICs in an specific area was found.
In order to get a better understanding of the distribution of ICs and PICs, a map of the Planetary Database was used and all approved craters were marked (see Fig. 6.74 and Fig. 6.75). The blue circles show non-polygonal craters while the red circles show PICs.

The crater size of a polygonal impact crater as a function of the number of straight rim segments can be seen in Figure 6.76. No correlation between the diameter of PICs and the number of straight crater rim segments was found.

There are many more unapproved impact craters than approved ones. Therefore, all impact craters

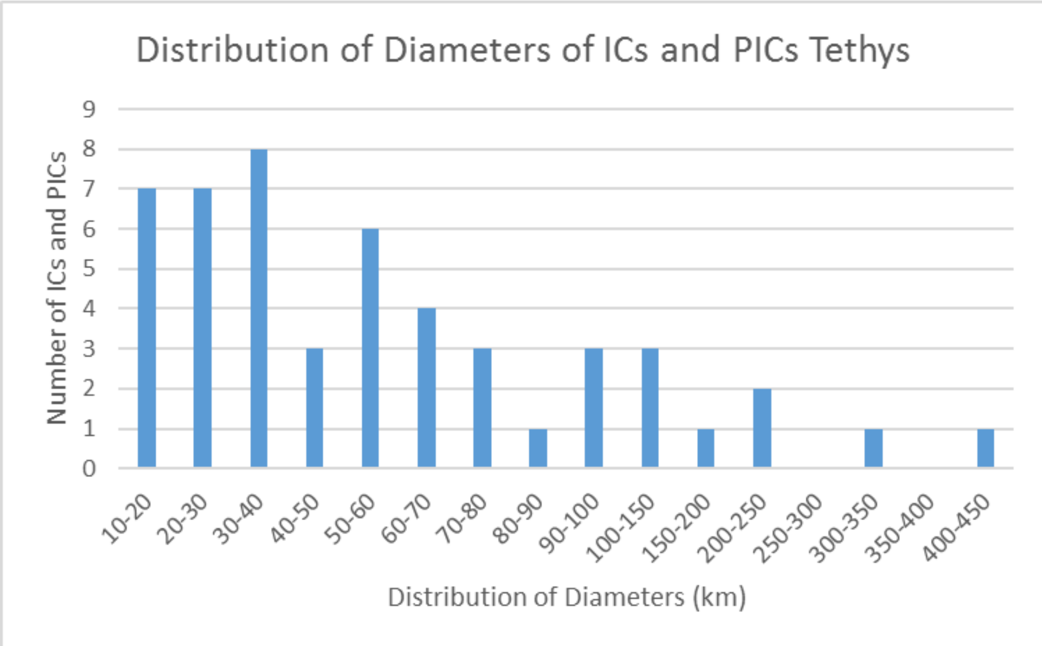

Figure 6.71: Distribution of diameters for all approved craters on Tethys, according to values for the diameters from the IAU/NASA/USGS Planetary Database. The diameters of all approved craters on Tethys range from 11.8 km to 445.0 km.

between a latitude of -60° and 60° which are large enough to be recognised as either polygonal or not were examined to check whether the percentage of PICs resulting from only approved craters in this study represents the total crater population of this body. Over all, 164 more PICs and 144 more non-polygonal impact craters were found and if the former approved PICs and non-polygonal impact craters are included, this leads to about 51% of impact craters being polygonal. All examined impact craters were marked on the map of the IAU/NASA/USGS Planetary Database (see Fig. 6.77).

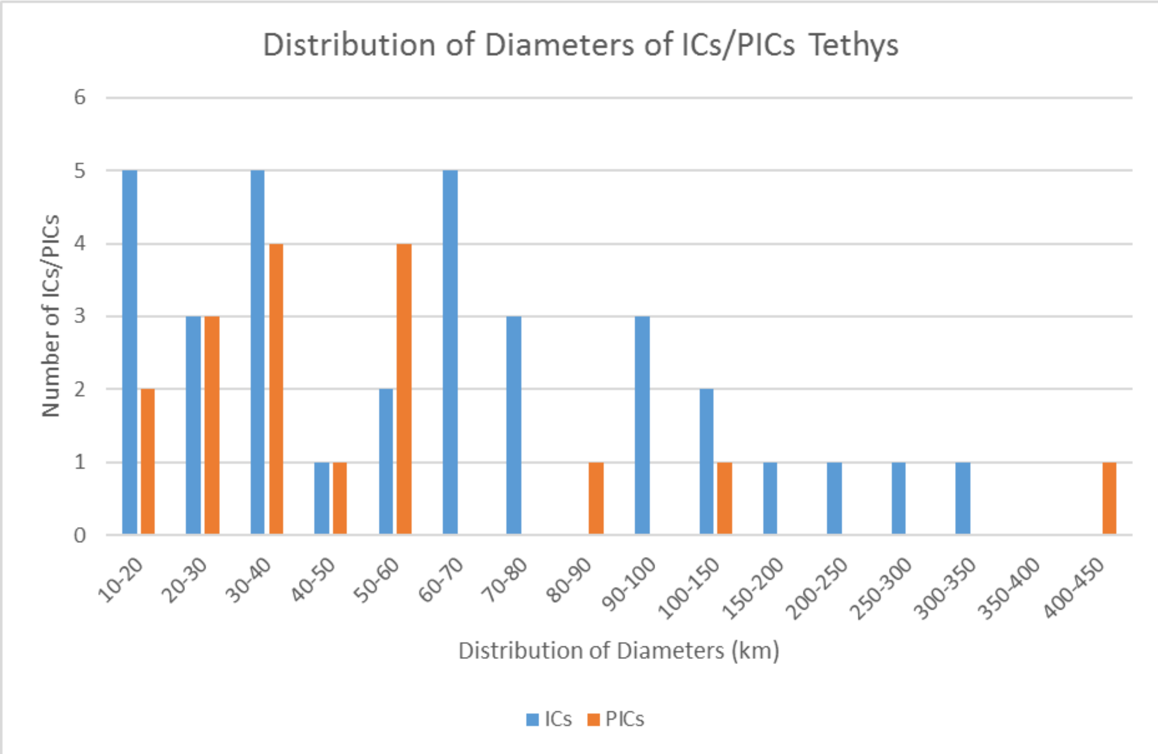

Figure 6.72: Distribution of diameters for non-polygonal impact craters (ICs) and polygonal impact craters (PICs) on Tethys. Values for the diameters were taken from the IAU/NASA/USGS Planetary Database. The diameters of non-polygonal impact craters range from 11.8 km to 320.0 km, the diameters of polygonal impact craters range from 12.5 km to 445 km.

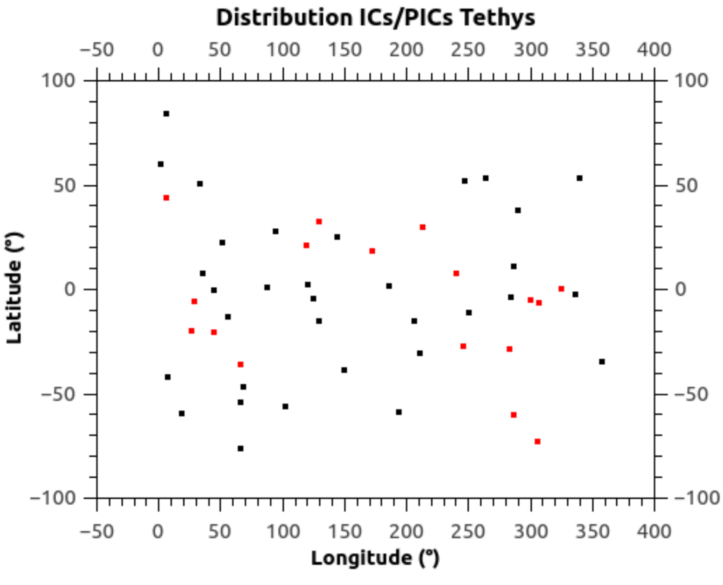

Figure 6.73: Distribution of approved craters of the IAU/NASA/USGS Planetary Database on Tethys. Coordinates were taken from this database. Black boxes show non-polygonal craters while red boxes show polygonal impact craters. No significant pattern concerning the distribution was found.

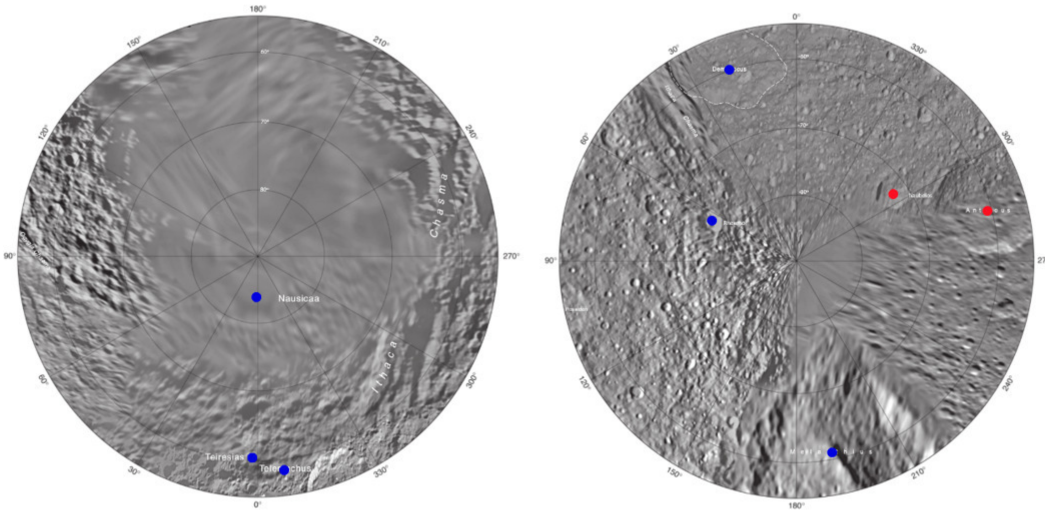

Figure 6.74: Distribution of approved craters from the IAU/NASA/USGS Planetary Database on the north pole (left) and south pole (right) of Tethys. Blue circles show non-polygonal impact craters while red circles show polygonal impact craters. No significant pattern was found.

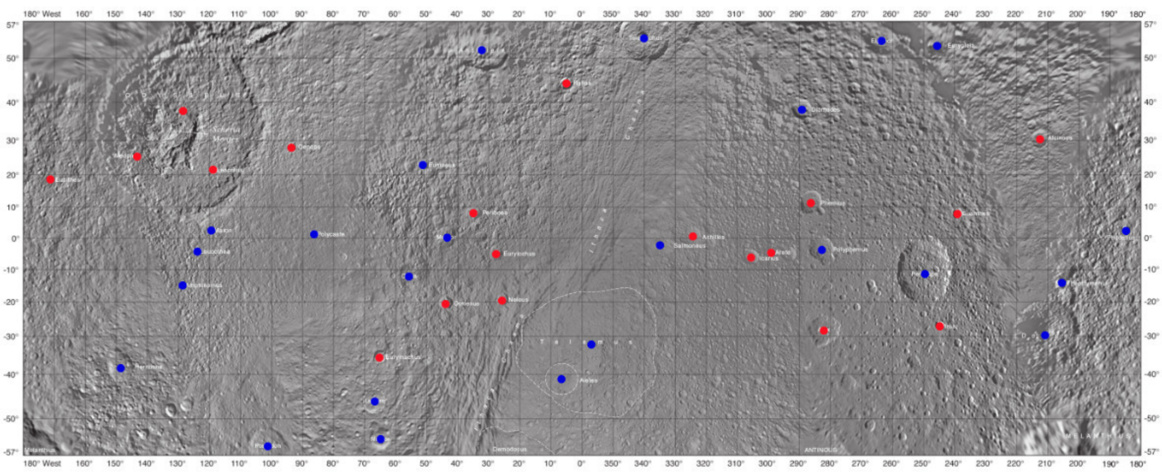

Figure 6.75: Distribution of approved craters from the IAU/NASA/USGS Planetary Database in the equatorial region of Tethys. Blue circles show non-polygonal impact craters while red circles show polygonal impact craters. Regarding the distribution of these two crater types no significant pattern was determined.

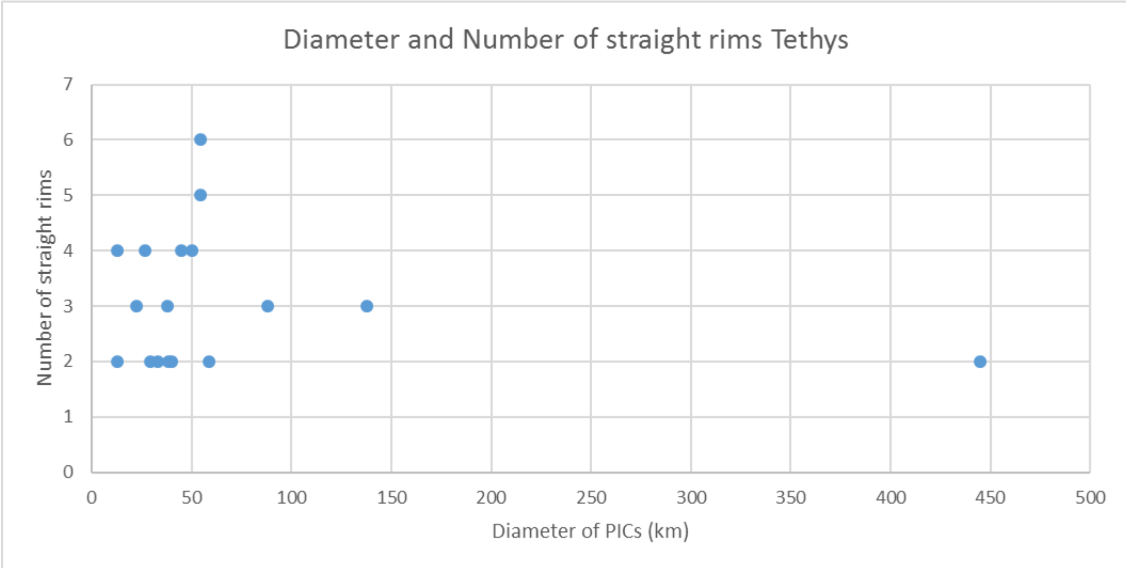

Figure 6.76: Number of straight crater rim segments as a function of crater size on Tethys. No correlation between the number of straight segments and the diameter of polygonal impact craters can be seen on Tethys.

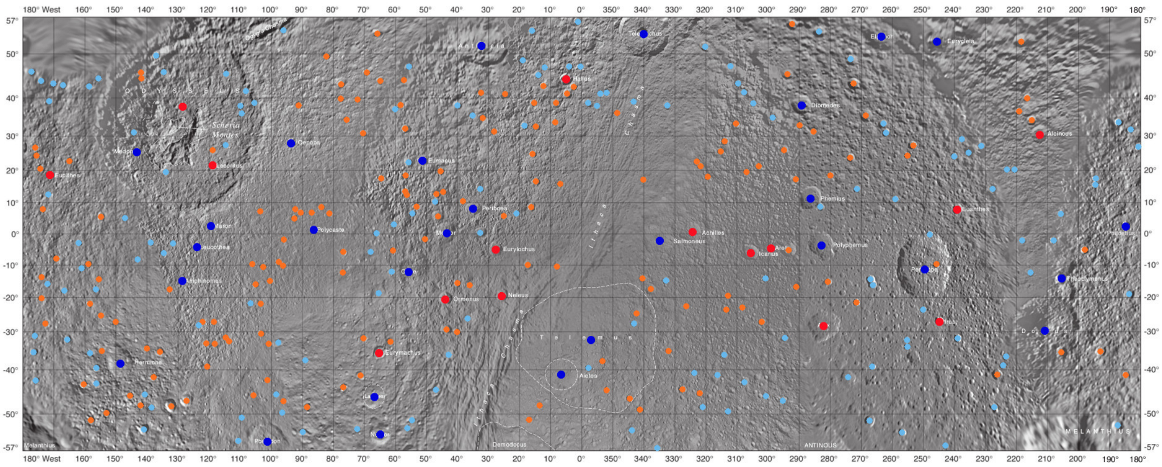

Figure 6.77: Polygonal impact craters (orange, red) and non-polygonal impact craters (light blue, blue) on the surface of Tethys. Red dots show approved PICs and orange dots show additional ones while blue dots mark approved non-polygonal craters and light blue dots mark additional non-polygonal craters. Over all, on Tethys there are 15 approved PICs, 164 unapproved PICs, 27 approved non-polygonal impact craters, and 144 additional unapproved non-polygonal impact craters.

7 Studies of Polygonal Impact Craters (PICs) on Asteroid Belt Objects

7.1 PICs on Ceres

On Ceres, there are 63 PICs out of 90 approved craters which works out at about 70%. Most of these are simple craters. All found PICs, including their diameters and coordinates, can be seen in Table 7.6. The values for the diameters, centre latitude, and centre longitude are adapted from the IAU/NASA/USGS Planetary Database.

One example of a PIC on Ceres, crater Fejokoo, has a diameter of 68 km and is located at a latitude of 29.15° and a longitude of 312.11° (see Fig. 7.78).

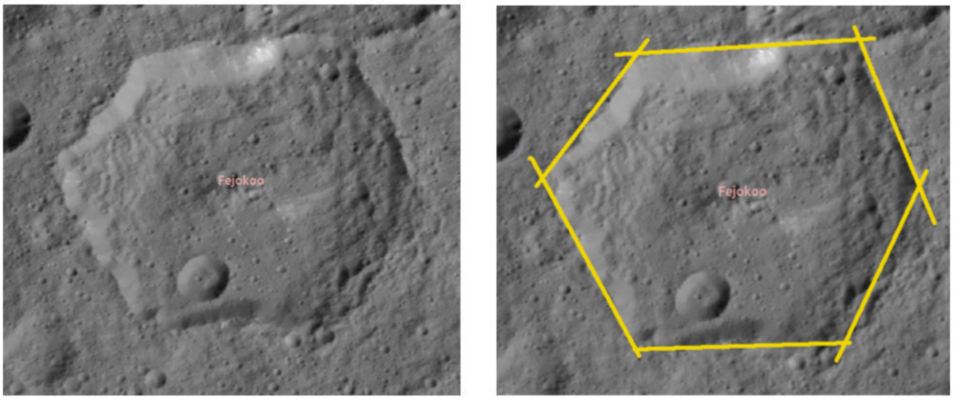

Figure 7.78: Polygonal impact crater Fejokoo on Ceres which has a diameter of 68 km and is located at a latitude of 29.15° and a longitude of 312.11° (left); included are its marked straight crater rim segments (right). Credit: IAU/NASA/USGS Planetary Database (2016).

Nr.	Crater	Diameter (km)	Centre Longitude (°)	Centre Latitude (°)
1	Abellio	32	33.2	293.09
2	Achita	40	25.82	65.96
3	Annona	60	-48.14	8.43
4	Anura	37	-13.92	11.79
5	Azacca	49.91	-6.66	218.4
6	Belun	36.04	-33.71	356.25
7	Besua	17	-42.35	300.21
8	Bonsu	31	1.74	93.21
9	Braciaca	8	-22.77	84.37
10	Cacaguat	13.6	-1.19	143.61
11	Chaminuka	122	-58.58	131.2

Nr.	Crater	Diameter (km)	Centre Longitude (°)	Centre Latitude (°)
12	Coniraya	135	39.9	65.73
13	Consus	64	-20.7	200.5
14	Cozobi	24	45.33	287.31
15	Dada	12	58.63	336.76
16	Dantu	126	24.3	138.23
17	Darzamat	92	-44.21	76.4
18	Doliku	15	-40.79	5.88
19	Ernutet	53.4	52.93	45.52
20	Ezinu	116	43.24	195.7
21	Fejokoo	68	29.15	312.11
22	Gaue	80	30.81	86.16
23	Hamori	60	-60.86	79.44
24	Hatipowa	40	-16.08	357.71
25	Haulani	34	5.8	10.77
26	Homshuk	70	11.23	94.06
27	Ialonus	16.5	48.15	168.53
28	Inamahari	68	14.13	89.22
29	Insitor	26	-10.71	124.87
30	Jaja	22	52.09	125.27
31	Jarimba	69	-24.08	21.25
32	Jarovit	66	67.9	284.74
33	Juling	20	-35.9	168.48
34	Kaikara	72	42.82	222.43
35	Kerwan	280	-10.77	123.99
36	Kiriamma	18.7	50.32	126.33
37	Kirnis	115	4.9	264.3
38	Kondos	44	-19.34	17.31
39	Kupalo	26	-39.44	173.2
40	Liber	23	42.56	37.8
41	Lociyo	37.8	-6.53	228.83
42	Lono	20	-36.61	304.37
43	Meanderi	103	-40.8	194.19
44	Messor	40	49.93	233.73
45	Nawish	77	18.28	193.79
46	Nepen	26.4	6.19	220.54
47	Ninsar	40	30.3	263.26
48	Oltagon	28	-25.95	37.96
49	Oxo	10	42.21	359.6
50	Piuku	31	-15.37	36.99
51	Razeka	38.38	-3.21	61.63
52	Rao	12	8.1	119.01
53	Roskva	22	58.9	333.02

Nr.	Crater	Diameter (km)	Centre Longitude (°)	Centre Latitude (°)
54	Shakaema	47	-3.66	33.93
55	Sintana	58	-48.07	46.2
56	Tafakula	34	-19.82	88.59
57	Tahu	25	-6.59	44.79
58	Takel	22	50.76	280.48
59	Tawals	8.8	-39.06	238.02
60	Tibong	36	-29.82	352.2
61	Tupo	36	-32.35	88.38
62	Victa	32	36.23	301.04
63	Xochipilli	22.7	56.66	93.21

Table 7.6: Found polygonal impact craters on Ceres from all approved craters of the IAU/NASA/USGS Planetary Database. Values for crater diameter, centre longitude, and centre latitude were taken from this database.

The number of straight rims ranges from two to seven, more than half of all PICs have two or three straight segments, resulting in a mean number of about 3.5. Only a few craters are hexagonal or pentagonal. There are nineteen craters that have two straight rims, fifteen craters that have three straight rims, sixteen craters that have four straight rims, eight craters that have five straight rims, two craters that have six straight rims, and three craters that have seven straight rims (see Fig. 7.79).

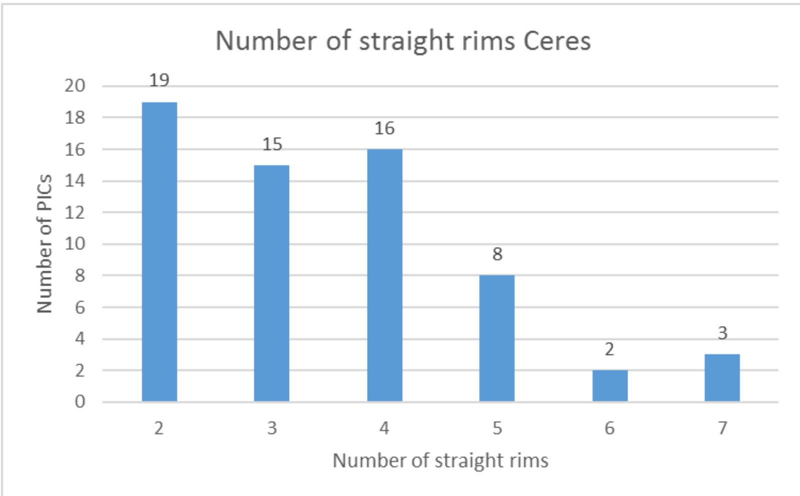

Figure 7.79: Number of straight crater rim segments on Ceres. There are nineteen craters having two straight rims, fifteen craters having three straight rims, sixteen craters having four straight rims, eight craters having five straight rims, two craters having six straight rims, and three craters having seven straight rims.

Due to the lack of high resolution maps for Ceres' polar regions and because of projection effects for the angle between the straight rims to be calculated only PICs between a centre latitude of 60° and -60° were taken into account. The angle between the straight rims ranges from about 107° to 159°, resulting in a mean angle of about 133°.

The diameters of all approved craters on Ceres range from 0.4 km to 280.0 km with a mean diameter of about 58.5 km. The diameters of non-polygonal impact craters on Ceres range from 0.4 to 260 km (mean diameter: 79.9 km) while the diameters of PICs are between 8 km to 280 km which gives a mean diameter of about 49.4 km. The size range in which PICs are most common is about $4 \times D_{tr}$. Figure 7.80 shows the distribution of diameters for all approved craters on Ceres. The comparison between the diameters of non-polygonal craters (ICs) and polygonal impact craters (PICs) can be seen in Figure 7.81.

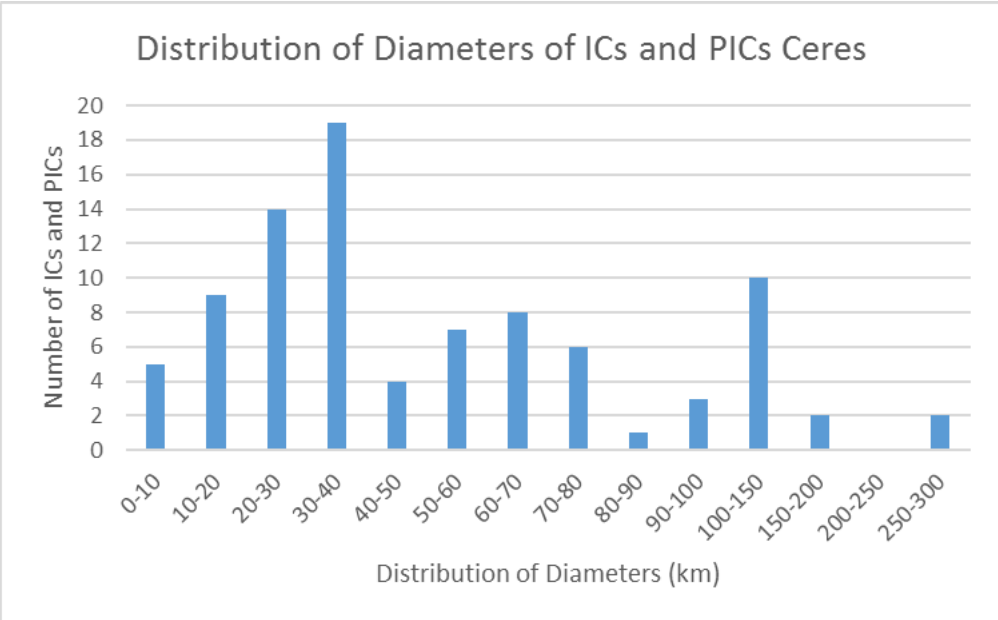

Figure 7.80: Distribution of diameters for all approved craters on Ceres, according to values for the diameters from the IAU/NASA/USGS Planetary Database. The diameters of all approved craters range from 0.4 km to 280.0 km, giving a mean diameter of about 58.5 km.

The distribution of all approved non-polygonal impact craters (black boxes) and polygonal impact craters (red boxes) can be seen in Figure 7.82. The values for the coordinates were taken from the IAU/NASA/USGS Planetary Database and, for a better comparison, non-polygonal impact craters (blue circles) and polygonal impact craters (red circles) were marked on a surface map from this database (see Fig. 7.83).

To study a possible correlation between the size of a PIC and the number of straight rims, crater diameter as a function of the number of straight rim segments was plotted (see Fig. 7.84). No significant correlation between these two characteristics of PICs was found.

Due to the fact that there are many more unapproved impact craters than approved ones, all impact craters between a centre latitude of -60° and 60° that are large enough to be recognised as polygonal

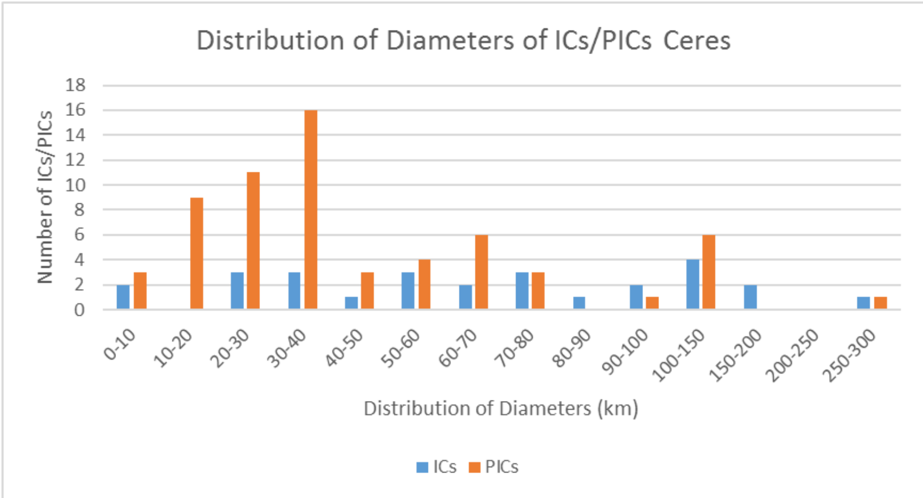

Figure 7.81: Distributon of diameters for non-polygonal impact craters (ICs) and polygonal impact craters (PICs) on Ceres. Values for the diameters were taken from the IAU/NASA/USGS Planetary Database. The diameters of ICs range from 0.4 km to 260 km (mean diameter: 79.9 km) while the diameters of PICs range from 8 km to 280 km, yielding a mean diameter of about 49.4 km.

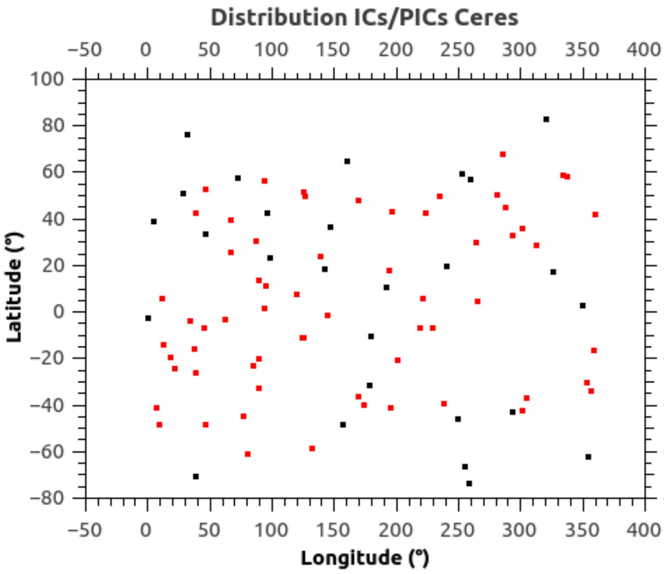

Figure 7.82: Distribution of approved craters of the IAU/NASA/USGS Planetary Database on Ceres' surface. Black boxes show non-polygonal impact craters while red boxes represent polygonal impact craters. No significant pattern concerning the distribution of PICs was found. Coordinate data was taken from the IAU/NASA/USGS Planetary Database.

or not were examined to check whether the percentage of PICs resulting from only approved craters in this study represents the total crater population of this body. Over all, 342 more PICs and 233 more non-polygonal impact craters were found and if the former approved PICs and non-polygonal impact craters are included, this leads to about 61% of impact craters being polygonal. All examined impact craters were marked in the map of the IAU/NASA/USGS Planetary Database (see Fig. 7.85).

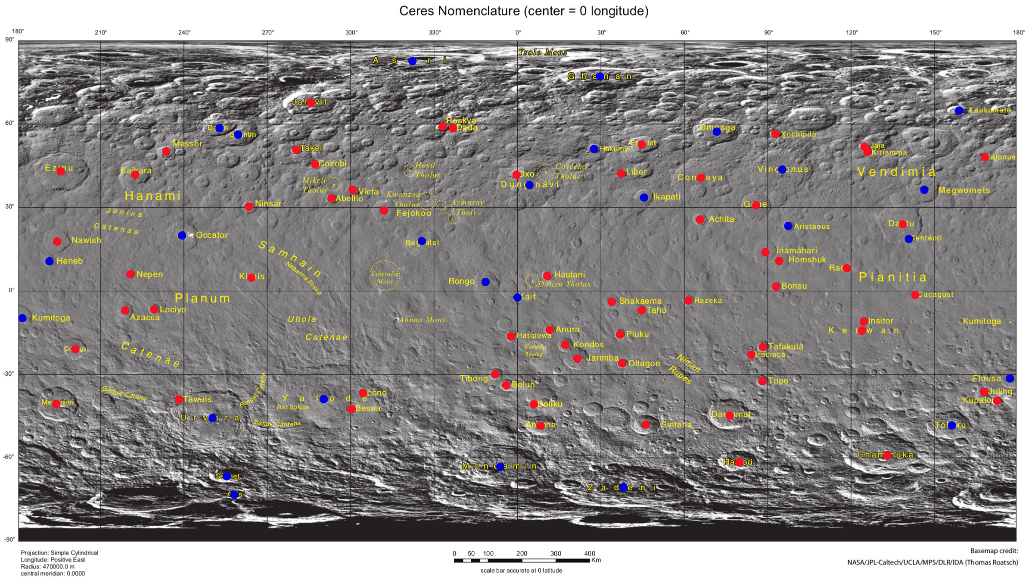

Figure 7.83: Distribution of approved craters of the IAU/NASA/USGS Planetary Database on the surface of Ceres. Non-polygonal impact craters (blue circles) and polygonal impact craters (red circles) have been marked on the image taken from the IAU/NASA/USGS Planetary Database.

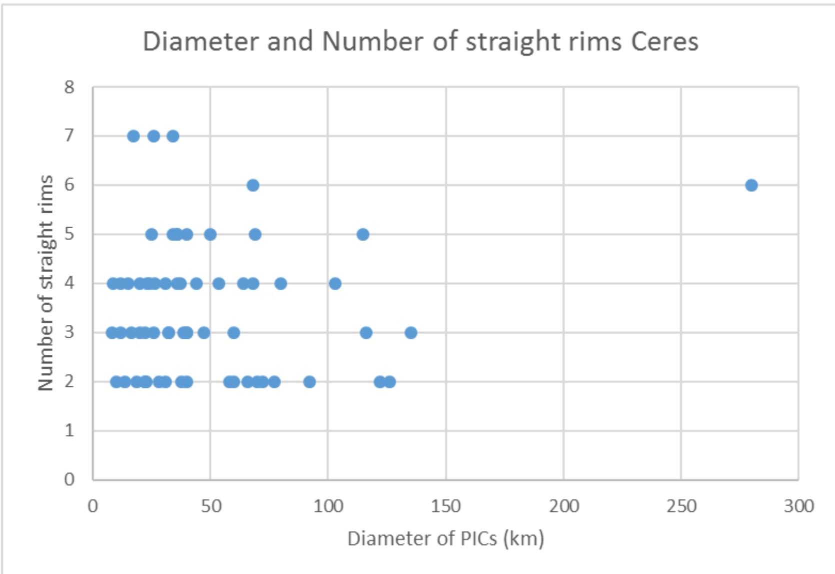

Figure 7.84: Number of straight crater rim segments as a function of crater size on Ceres. No correlation between the crater size and the number of straight rims was found.

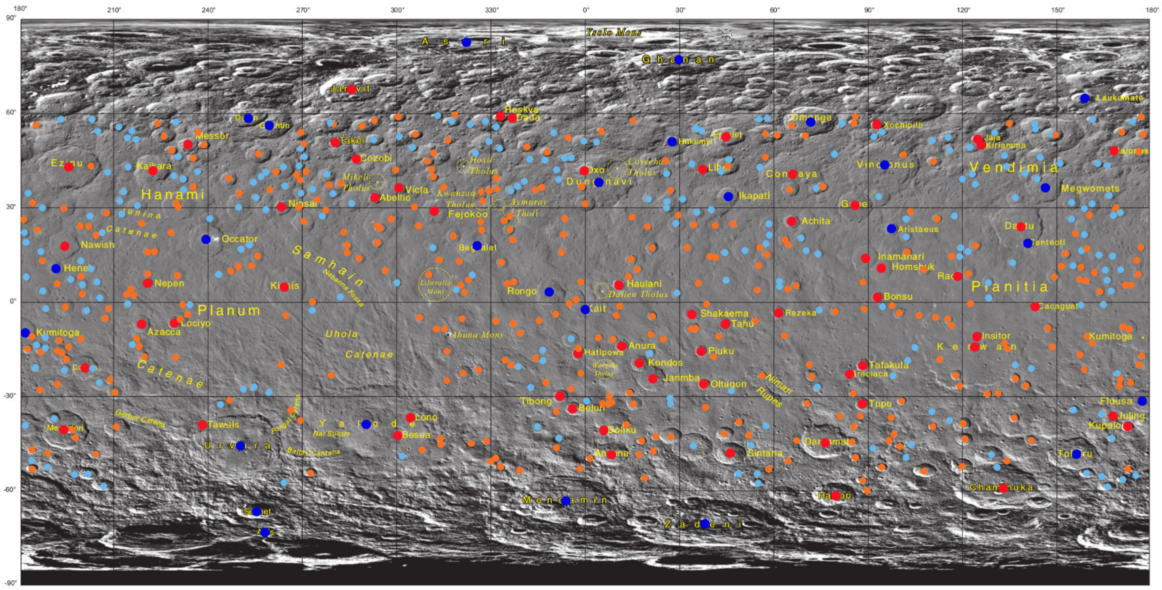

Figure 7.85: Polygonal impact craters (orange, red) and non-polygonal impact craters (light blue, blue) on the surface of Ceres. Red dots show approved PICs and orange dots show additional ones while blue dots show approved non-polygonal craters and light blue dots show additional non-polygonal craters. Over all, on Ceres there are 61 approved PICs, 342 unapproved PICs, 20 approved non-polygonal impact craters and 233 unapproved non-polygonal impact craters.

7.2 PICs on Vesta

On Vesta there are 50 PICs out of 90 approved craters in the IAU/NASA/USGS Planetary Database which results in about 56% of all approved craters being polygonal. All of the PICs on Vesta are simple craters and are listed in Table 7.7, including their diameters and coordinates adapted from the IAU/NASA/USGS Planetary Database.

One example of a PIC on Vesta is crater Canuleia which has a diameter of 11.32 km and is located at a latitude of -33.62° and a longitude of 84.52°. This crater can be seen in Fig. 7.86 including its marked straight rims.

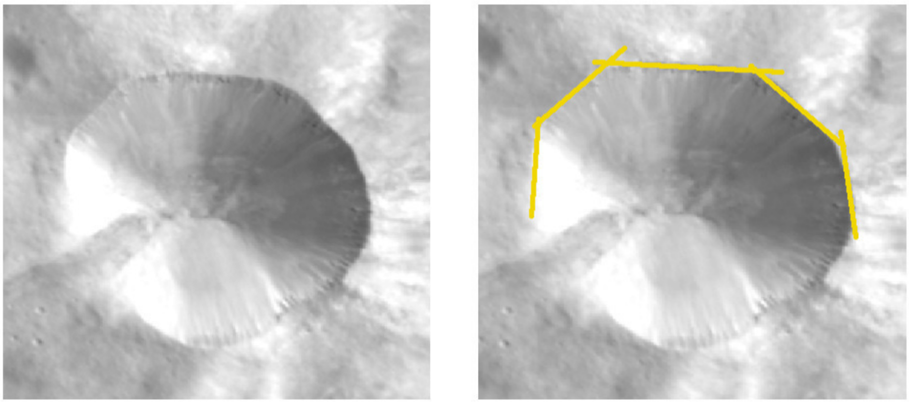

Figure 7.86: Polygonal impact crater Canuleia on Vesta which has a diameter of 11.3 km and is located at a latitude of -33.62° and a longitude of 84.52° (left), included are its marked straight crater rim segments (right). Credit: IAU/NASA/USGS Planetary Database (2016).

Nr.	Crater	Diameter (km)	Centre Longitude (°)	Centre Latitude (°)
1	Aconia	19	7.54	151.37
2	Aelia	4.34	-14.26	290.8
3	Albia	5.79	-27.85	78.85
4	Aquilia	36.82	-49.41	190.88
5	Arruntia	10.49	39.44	221.59
6	Bellicia	41.68	37.73	197.76
7	Canuleia	11.32	-33.62	84.52
8	Caparronia	53.2	35.71	317.03
9	Coelia	14.06	-1.14	239.82
10	Cornelia	14.9	-9.37	15.57
11	Cossinia	15.72	0.63	178.96
12	Domna	13.53	-11.11	225.93
13	Drusilla	20.34	-15.05	51.22
14	Eumachia	25.78	0.14	317.06
15	Eutropia	21.09	22.4	255.01
16	Fabia	11.62	15.53	55.76
17	Fausta	3.14	-25.44	99.76

Nr.	Crater	Diameter (km)	Centre Longitude (°)	Centre Latitude (°)
18	Floronia	18.54	36.23	94.06
19	Fonteia	20.61	-53.25	291.41
20	Fulvia	16.73	-26.13	292.65
21	Galeria	21.77	-29.82	18.38
22	Gegania	22.33	4.05	210.77
23	Graecina	11.93	-37.45	237.01
24	Helena	22.06	-41.51	272.55
25	Herennia	22.33	-72.42	10.33
26	Hortensia	29.45	-46.85	165.38
27	Laelia	8.89	-46.82	290.45
28	Laurentia	11.48	-28.15	92.8
29	Lepida	42.9	16.74	96.76
30	Longina	17.65	36.96	20.65
31	Mamilia	35.67	48.39	82.09
32	Minervina	18.34	16.85	199.29
33	Numisia	29.94	-7.48	37.25
34	Oppia	36.67	-7.89	99.08
35	Paulina	18.13	10.92	133.11
36	Perpennia	21.36	-23.03	258.75
37	Pinaria	41.76	-29.54	181.63
38	Placidia	14.75	19.24	281.38
39	Publicia	15.79	14.53	234.36
40	Rubria	10.27	-7.32	168.34
41	Rufillia	15.79	-12.92	288.71
42	Scantia	18.61	29.63	64.65
43	Sextilia	19.48	-39	295.93
44	Sossia	8.11	-36.78	75.76
45	Tarpeia	40.29	-69.47	179.3
46	Torquata	34.73	46.45	143.78
47	Tuccia	11.65	-39.86	346.81
48	Urbinia	24.25	-29.88	66.26
49	Vettenia	18.89	4.8	229.31
50	Vibidia	7.1	-26.96	10.3

Table 7.7: Found polygonal impact craters on Vesta including their diameters, centre longitudes, and centre latitudes. The values for the diameters, centre latitudes, and centre longitudes are adapted from the IAU/NASA/USGS Planetary Database.

The number of straight rims ranges from two to seven with more than two thirds of all PICs having two, three, or four straight rims, leading to a mean number of 3.2 straight rims. Only a few PICs are pentagonal or hexagonal. There are nineteen PICs having two straight rims, thirteen PICs having three straight rims, eleven PICs having four straight rims, six PICs having five straight rims and one

PIC having seven straight rims (see Fig. 7.87).

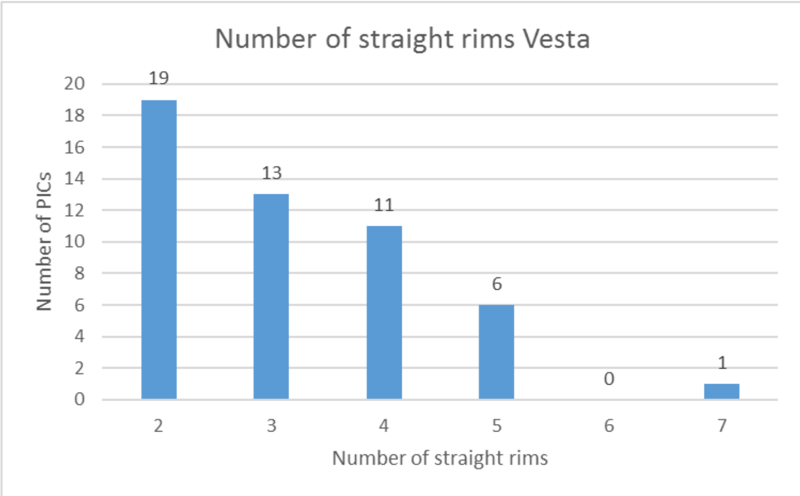

Figure 7.87: Number of straight crater rim segments on Vesta. More than two thirds of all PICs have two, three, or four straight rims whereas only a few are pentagonal or hexagonal. There are nineteen PICs that show two crater rim segments, thirteen show three straight rims, eleven show four straight rims, six show five straight rims and only one crater shows seven straight rims.

Due to uncertainties concerning the measurement of the angles between the straight rims in the polar regions and the lack of high resolution images of these regions, in order to calculate the mean angle only PICs between a centre latitude of 60° and -60° were taken into account. For the angle between the straight rims values from 84° to 159° were measured with a mean angle of 134°.

The diameters of all approved craters on Vesta range from 0.6 km to 450 km with a mean diameter of about 34.7 km. The diameters of non-polygonal impact craters on Vesta lie between 0.6 km and 450 km (mean diameter: 52.3 km) while the diameters of PICs only range from 3.1 km to 53.2 km, resulting in a mean diameter of about 20.6 km. The diameter range in which PICs on Vesta are most common is about $0.7 \times D_{tr}$. The distribution of diameters for all approved craters on Vesta can be seen in Figure 7.88, while Figure 7.89 shows the comparison between the diameters of non-polygonal craters (ICs) and polygonal impact craters (PICs).

The distribution of non-polygonal impact craters (black squares) and PICs (red squares) on the surface of Vesta can be in Figure 7.90 where the values for the coordinates were taken from the IAU/NASA/USGS Planetary Database. To get a better overview of the distribution of these two crater types, non-polygonal impact craters (blue circles) and PICs (red circles) were marked on a surface map of Vesta from the IAU/NASA/USGS Planetary Database (see Fig. 7.91). No significant pattern was found regarding the distribution of these two crater types.

To examine the number of straight rims and the size of the polygonal impact crater, a plot was made (see Fig. 7.92) which shows no correlation between these two characteristics of PICs.

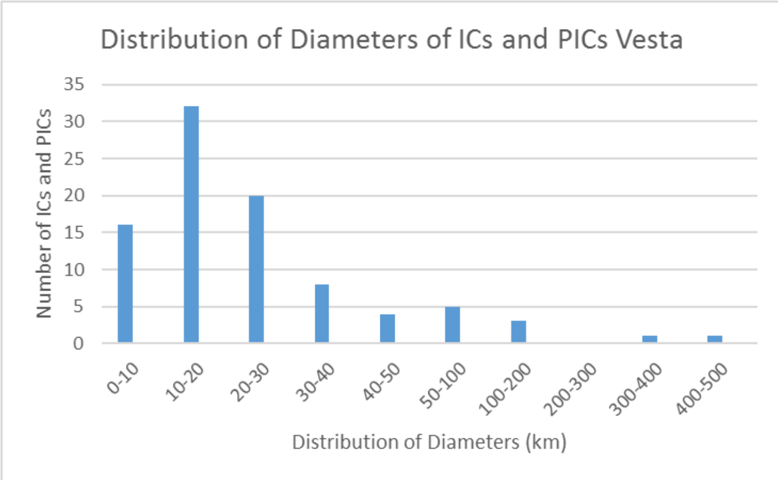

Figure 7.88: Distribution of diameters for all approved craters on Vesta, according to values for the diameters from the IAU/NASA/USGS Planetary Database. The diameters of the craters range from 0.6 km to 450.0 km, yielding a mean diameter of about 34.7 km.

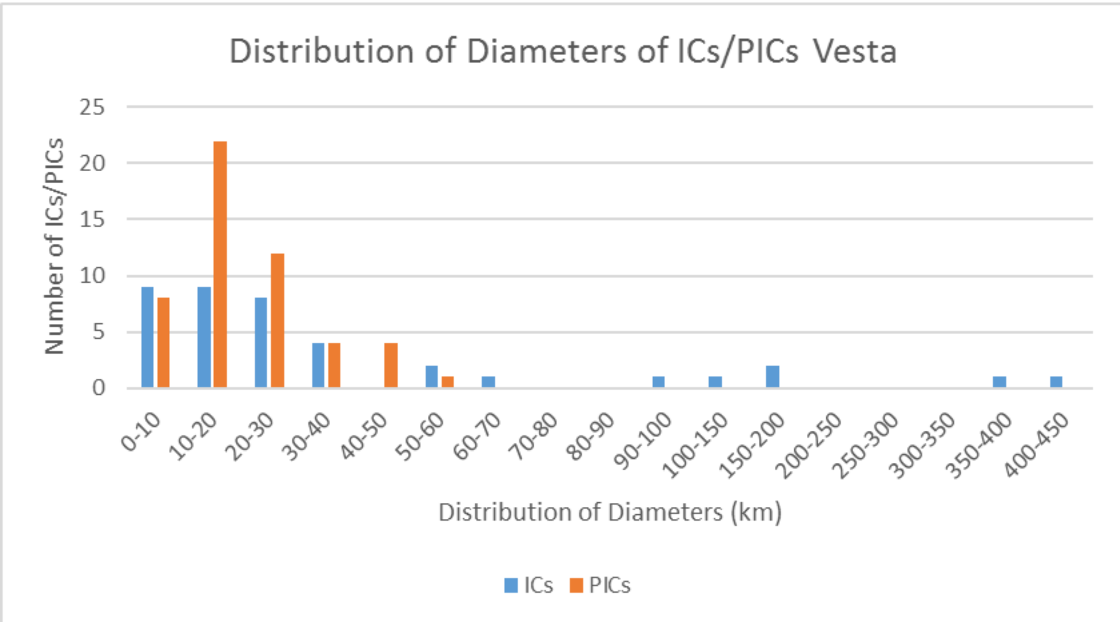

Figure 7.89: Distribution of diameters for non-polygonal impact craters (ICs) and polygonal impact craters (PICs) on Vesta. Values for the diameters were taken from the IAU/NASA/USGS Planetary Database. The diameters of ICs range from 0.6 km to 450.0 km (mean diameter: 52.3 km), while the diameters of PICs only range from 3.1 km to 53.2 km, yielding a mean diameter of about 20.6 km.

As there are many more unapproved impact craters than approved ones, all impact craters between a latitude of -60° and 60° large enough to be recognised as polygonal or not were examined to check whether the percentage of polygonality resulting from only approved craters in this study represents the total crater population of this body. Over all, 151 more PICs and 134 more non-polygonal impact craters were found and, including the former approved PICs and non-polygonal impact craters, this

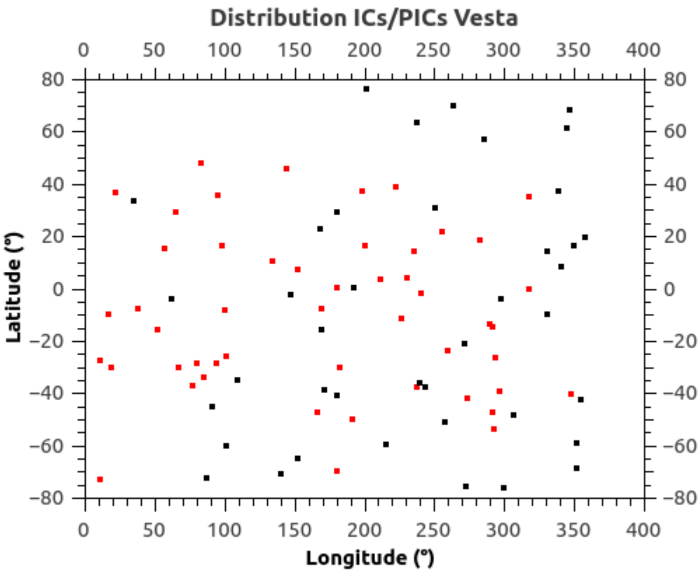

Figure 7.90: Distribution of approved craters from the IAU/NASA/USGS Planetary Database for the surface of Vesta. Black squares show non-polygonal impact craters and red squares show polygonal impact craters. The values for the coordinates were taken from the IAU/NASA/USGS Planetary Database. No significant pattern was found concerning the distribution of non-polygonal impact craters or PICs.

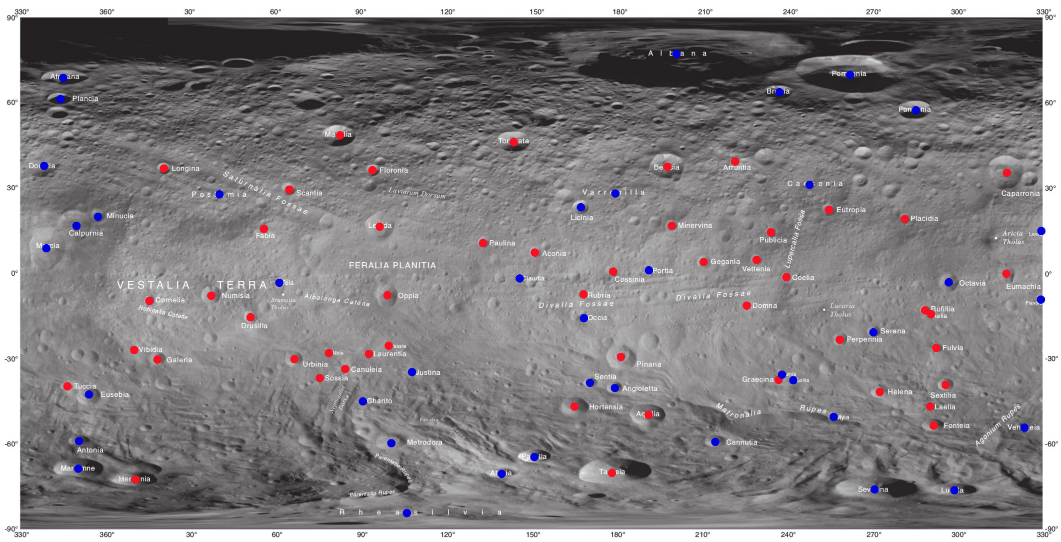

Figure 7.91: Non-polygonal impact craters (blue circles) and polygonal impact craters (red circles) marked on a surface map from the IAU/NASA/USGS Planetary Database. No significant pattern was found concerning the distribution of non-polygonal impact craters and PICs.

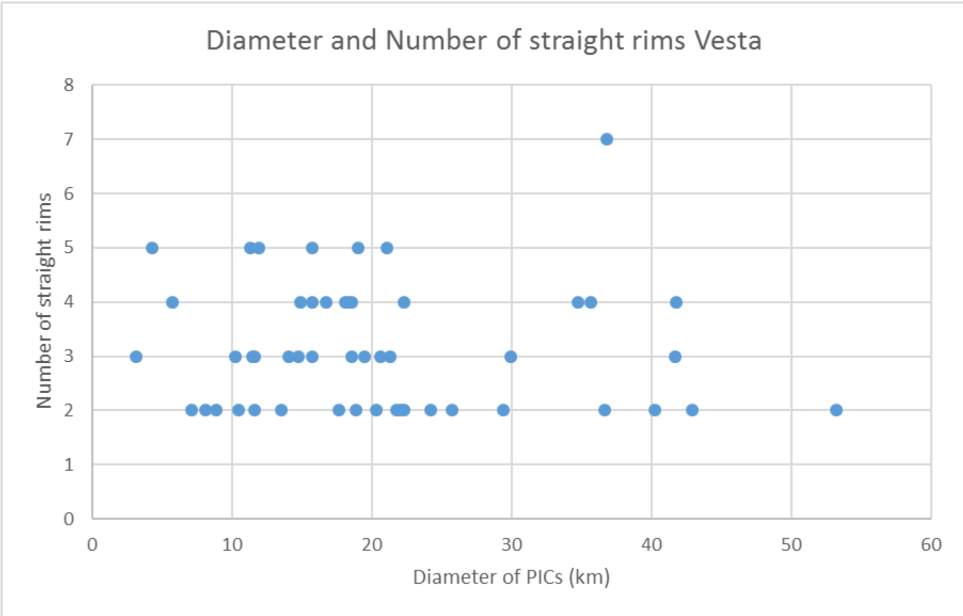

Figure 7.92: Number of straight crater rim segments as a function of crater size on Vesta. Values for diameters were taken from the IAU/NASA/USGS Planetary Database. No correlation between crater size and polygonality was found for PICs on Vesta.

leads to about 55% of impact craters being polygonal. All examined impact craters were marked on the map of the IAU/NASA/USGS Planetary Database (see Fig. 7.93).

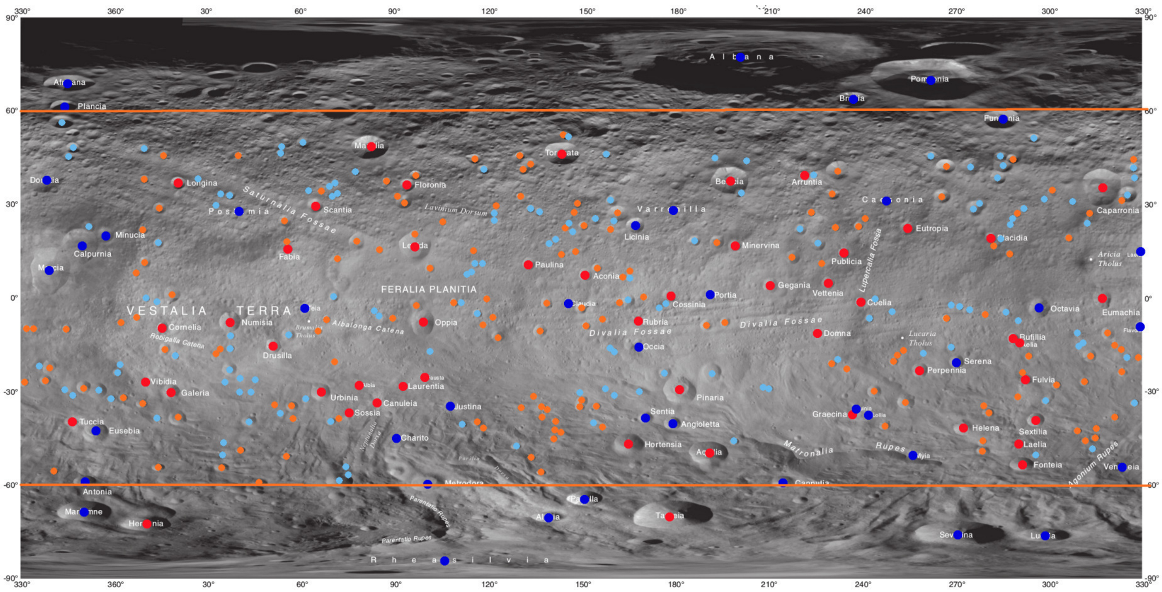

Figure 7.93: Polygonal impact craters (orange, red) and non-polygonal impact craters (light blue, blue) on Vesta's surface. Red dots show approved PICs and orange dots show additional PICs while blue dots show approved non-polygonal craters and light blue dots show additional non-polygonal craters. Over all, on Vesta there are 48 approved PICs, 151 unapproved PICs, 29 approved non-polygonal impact craters and 134 unapproved non-polygonal impact craters.

8 Discussion

In total 431 approved impact craters on Rhea, Dione, Tethys, Ceres, and Vesta from the Planetary Database were studied, and 234 of these were classified as PICs, most of them with two or three straight crater rim segments; only a few craters were hexagonal or pentagonal. Figure 8.94 shows a comparison of the number of straight rim segments for Rhea (red), Dione (blue), Tethys (green), Ceres (violet), and Vesta (yellow).

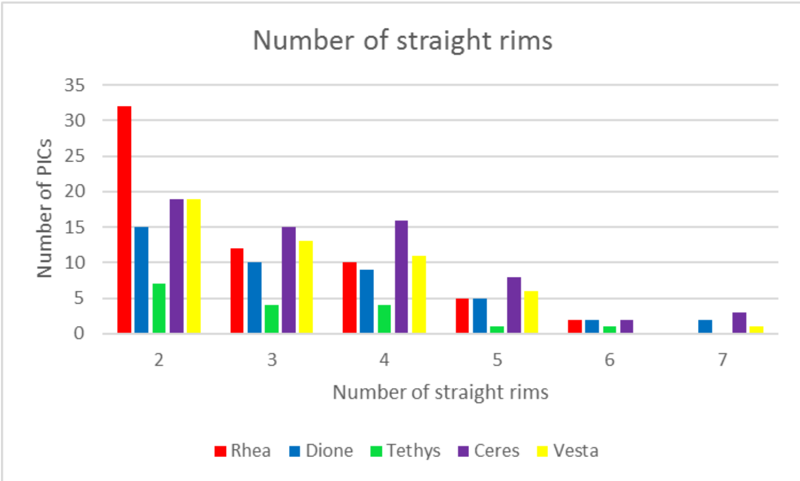

Figure 8.94: Number of straight crater rim segments of Rhea (red), Dione (blue), Tethys (green), Ceres (violet), and Vesta (yellow). Most of the craters have two or three straight crater rims, only a few craters are hexagonal or pentagonal.

The mean number of straight crater rims which is between 2.9 and 3.5 for Rhea, Dione, Tethys, Ceres, and Vesta accords well with previous studies from Weihs (2012) who gave a mean number of 2.5 for PICs on Mercury. Also, the mean angle between the straight crater rim segments which lies in a range from 121° to 134° for the studied minor objects is nearly equal to Weihs et al. (2015) who gave 112°. For a comparison of the percentage of PICs on the studied objects, the mean number of straight crater rim segments and the mean angle see Table 8.8.

Object	# Craters	# PICs	% of PICs	Straight rims	Mean angle (°)
Rhea	128	61	48	2.9	121
Dione	73	43	59	3.4	124
Tethys	50	17	34	3.1	123
Ceres	90	63	70	3.5	133
Vesta	90	50	56	3.2	134

Table 8.8: Number of all approved impact craters and identified PICs, percentage of PICs, mean number of straight crater rim segments and mean angle for the studied objects Rhea, Dione, Tethys, Ceres, and Vesta.

Also, the preferred size distribution of PICs, meaning that they favour small to midsized diameters, as suggested by studies of PICs on Mercury, Venus, Mars, and the Moon (e.g. Weihs et al., 2015; Aittola et al., 2007; Öhman et al., 2008; Öhman et al., 2010) was approved on all objects. This is true even on Dione where Beddingfield et al. (2016) mention that they did not find such a relation. Regarding a correlation between the favoured size range and the transition diameter between simple to complex impact craters, it was found that Rhea yields about $7 \times D_{tr}$, Dione yields about $5 \times D_{tr}$, Tethys yields about $4.5 \times D_{tr}$, Ceres yields $4 \times D_{tr}$ and Vesta yields about $0.7 \times D_{tr}$. The values for Dione, Tethys and Ceres accord well with studies by Öhman (2009) who yields 3-4 $\times D_{tr}$ for Venus, 2-5 $\times D_{tr}$ for Mars and 1.3-3 $\times D_{tr}$ for the Moon. The results for Rhea and Vesta are a bit higher or lower, respectively.

No correlation between the size of the polygonal craters and the number of straight crater rim segments as Otto et al. (2016) suggest on Ceres where they stated that they observed "fewer edges with decreasing crater size" was found. This relation could not be seen either on Ceres or on any other studied object.

A large number of PICs was found in this study and the percentage of PICs found is much higher than was previously studied on PICs on Mercury, Venus, Mars, and the Moon. On the terrestrial planets and the Moon about 10-25% of the studied craters were polygonal (Weihs et al., 2015; Aittola et al., 2010; Öhman et al., 2008; Öhman et al., 2010), whereas on the studied Saturnian satellites and asteroids the percentage lies between 40% and 60%. A comparison of the results of previous studies, the percentage of PICs and their mean angles can be seen in Table 8.9.

Object	Craters	PICs	% of PICs	Mean angle (°)
Mercury	291	33	11	112
Venus	550	121	22	-
Moon (10°W-40°E, 10°N-50°S)	656	167	25	-
Mars (Greater Hellas region, Argyre region)	-	1575	16	-
Rhea	128	61	48	121
Dione	73	43	59	124
Tethys	50	17	34	123
Ceres	90	63	70	133
Vesta	90	50	56	134

Table 8.9: Number of examined impact craters (ICs), polygonal impact craters (PICs), percentage of PICs and the angles between the straight rims of previous studies of the terrestrial planets and the Moon by Weihs et al. (2015); Aittola et al. (2010); Öhman et al. (2008); Öhman et al. (2010), and the objects of this study.

Otto et al. (2016) detected 258 PICs on Ceres having a mean diameter of 21 km which is in contrast to this study which found 403 PICs on Ceres, whereas the mean diameter of all approved craters that were classified as PICs yields 49.4 km. Unfortunately, Otto et al. (2016) did not mention which definition they used for a PIC and in which size range they studied impact craters and, therefore, these two studies could not be compared in a fruitful way.

One explanation why the percentage of PICs on Rhea, Dione, Tethys, Ceres, and Vesta is higher than it is on the terrestrial planets and the Moon, could be the different surface compositions of these objects (Neidhart et al., 2017b). Most of the minor bodies' surfaces consist mostly of water ice which has a much lesser density than basalt; the crust is thinner as well. One exception is Vesta whose surface, like those of the terrestrial planets and the Moon, is also composed of basalt, but with 54% of impact craters being PICs, it has a much higher percentage of PICs than the terrestrial planets and the Moon. Table 8.10 shows the comparison of the percentage of PICs, the surface density, and the primary surface composition of all bodies on which PICs were studied in detail. The percentage of PICs of the terrestrial planets and the Moon are from Weihs et al. (2015); Aittola et al. (2010); Öhman et al. (2008) and Öhman et al. (2010), the percentages of PICs for the other objects are from this study. Values for the surface densities were taken from Schön (1983); Planetary Society (2012); Baratoux et al. (2014); Lide (2005); Park et al. (2016) and Raymond et al. (2013).

Object	PIC (%)	Surface density (kg/m^3)	Surface composition
Mercury	11	2960	Basalt
Venus	22	2960	Basalt
Moon	25	2550	Basalt
Mars	16	3100-3300	Basalt
Rhea	44	916.7	Water ice
Dione	50	916.7	Water ice
Tethys	51	916.7	Water ice
Ceres	61	1680-1950	Water ice, hydrated minerals
Vesta	54	2800-3100	Basalt

Table 8.10: Comparison of percentages of PICs, surface density, and primary surface composition of Mercury, Venus, Mars, and the Moon (Weihs et al., 2015; Aittola et al., 2010; Öhman et al., 2008; Öhman et al., 2010), and the objects of this study. Values for the surface densities were taken from Schön (1983); Planetary Society (2012); Baratoux et al. (2014); Lide (2005); Park et al. (2016) and Raymond et al. (2013).

For a definite answer, however, why the percentage of PICs on Rhea, Dione, Tethys, Ceres, and Vesta is higher than on the terrestrial planets and the Moon, a greater understanding of the PIC formation process, which is still unclear, is necessary (Neidhart et al., 2017a). Further studies, especially cratering experiments in fractured terrain, and simulations might help to achieve a better knowledge of the exact formation processes which lead to the formation of these special craters, thus providing a good tool with which to localize weakness zones in the crust, even if these are not visible due to the lack of faults and fractures on the surface and the composition of planetary surfaces.

9 Conclusion

The striking shape of polygonal impact craters has attracted the attention of scientists since the 18^{th} century. Now, detailed surface images enable the study of their abundances and characteristics. Although there are several studies of PICs on the terrestrial planets and the Moon, there exist only a few such studies on the satellites and asteroids. The Cassini and Dawn missions have provided images of surfaces with an appropriate resolution to study them. Therefore, the aim of this master's thesis was to acquire more information about PICs on the Saturnian satellites Rhea, Dione, and Tethys, and the asteroids Ceres and Vesta.

The study proves that a large number of polygonal impact craters exist on Rhea, Dione, Tethys, Ceres, and Vesta and that these craters are also common on icy satellites and asteroids. In total 431 approved craters in the IAU/NASA/USGS Planetary Database were examined and 234 of them were classified as polygonal. They mostly have two or three straight crater rim segments and only few are pentagonal or hexagonal. The mean value for the number of straight crater rim segments and the mean angles between them are in accordance with previous studies. The previous assumption that PICs favour small to midsized diameters was also confirmed. Furthermore, due to the fact that there are many more unapproved than approved impact craters on these objects, unapproved craters were also studied, in which 879 out of 1659 craters were considered polygonal .

The percentage of PICs on the studied objects is a great deal higher than on the terrestrial planets and the Moon. One possible explanation for this could be due to the different surface composition of these objects in comparison to the terrestrial planets and the Moon, but for definite answers further understanding of the formation process of PICs, which is still unclear, is necessary.

Further research, especially cratering experiments and simulations, might help to get a deeper understanding of the exact formation processes. As PICs form due to fractures they could be a good tool for acquiring information about weakness zones in the crust, even if they are not visible due to the lack of faults and fractures on the surface.

Abstract in English

A polygonal impact crater (PIC) is a crater that does not have a full circular shape in plane view but consists of straight crater rim segments. PICs are a common phenomenon throughout our Solar System and exist on all bodies that have a cratered surface. Previous studies have shown that PICs make up about 10-25 % of craters on Mercury, Venus, Mars, and the Moon. Although there were several studies on PICs on the terrestrial planets and the Moon, there have been only a few investigations of PICs on other satellites and asteroids, even though surface maps exist of Rhea, Dione, Tethys, Ceres, and Vesta with an appropriate resolution.

In this study, all approved impact craters on Rhea, Dione, Tethys, Ceres, and Vesta were analysed using images from the IAU/NASA/USGS Planetary Database. Craters were defined as polygonal if they consisted of at least two straight crater rim segments and a discernable angle. The straight crater rim segments were marked, the angles between them were measured, and statistics were performed regarding their number of straight rims, diameters, and distribution. The results were then compared to previous studies. On Rhea, the unknown diameters of 48 craters were measured. In total, 431 impact craters were examined and 234 of these were classified as polygonal. On Rhea about 48% of the approved craters are polygonal, on Dione 59%, on Tethys 34%, on Ceres 70%, and on Vesta 56%. The mean number of straight rims yields 2.9 for Rhea, 3.4 for Dione, 3.1 for Tethys, 3.5 for Ceres, and 3.2 for Vesta, which results in most of the PICs having two or three straight rim segments with only a few PICs being hexagonal or pentagonal. Due to the lack of high resolution maps for the polar regions of Ceres and Vesta and because of projection effects for the calculation of the angles between the straight segments, only PICs between a centre latitude of 60° and -60° on these asteroids were considered. The mean angle between the straight rims yields 121° for Rhea, 124° for Dione, 123° for Tethys, 133° for Ceres and 134° for Vesta. Since there are many more unapproved craters than approved ones on these bodies, the percentage of PICs between a latitude of 60° and -60° was determined, yielding about 44% for Rhea, 50% for Dione, 51% for Tethys, 61% for Ceres and 55% for Vesta.

The results regarding the mean number of straight rims and the angles between them accord well with previous studies; the assumption that PICs seem to favour small to midsized diameters has also been proved. The study shows that a large number of polygonal impact craters exist on Rhea, Dione, Tethys, Ceres, and Vesta, yet it is still unclear why the percentage of PICs on these bodies is much higher than for terrestrial planets and the Moon. One possible solution could be the different compositions of the surfaces of these bodies in comparison to the terrestrial planets, however, for definite answers to this question further understanding of the formation process of PICs, which is still unclear, is necessary.

Abstract in German

Unter einem polygonalen Einschlagskrater (PIC) versteht man einen Krater, der in Draufsicht nicht vollständig rund erscheint, sondern aus geraden Kraterwandsegmenten besteht. PICs sind ein häufiges Phänomen in unserem Sonnensystem und existieren auf allen Himmelskörpern, die eine gekraterte Oberfläche aufweisen. Frühere Untersuchungen haben gezeigt, dass der Anteil an PICs auf Merkur, Venus, Mars und dem Mond rund 10-25 % beträgt. Obwohl es zahlreiche Untersuchungen zu PICs auf den terrestrischen Planeten und dem Mond gibt, existieren nur wenige Studien zu PICs auf anderen Monden und Asteroiden, trotz des Vorhandenseins von Oberflächenaufnahmen von Rhea, Dione, Tethys, Ceres und Vesta, die eine entsprechende Auflösung haben.

In der vorliegenden Arbeit wurden alle bestätigten Einschlagskrater auf Rhea, Dione, Tethys, Ceres und Vesta untersucht, wobei Aufnahmen der planetaren IAU/NASA/USGS Datenbank verwendet wurden. Ein Krater wurde als polygonal klassifiziert, wenn er aus mindestens zwei geraden Kraterwandsegmenten besteht, die einen klar erkennbaren Winkel einschließen. Die geraden Segmente wurden markiert, der eingeschlossene Winkel gemessen und statistische Untersuchungen bezüglich der Anzahl an geraden Segmenten, des Kraterdurchmessers und der Kraterverteilung wurden durchgeführt. Die Ergebnisse wurden mit denen früherer Studien verglichen. Auf Rhea wurden die unbekannten Durchmesser von 48 Kratern ermittelt. Insgesamt wurden 431 Krater untersucht und 234 davon als polygonal klassifiziert. Auf Rhea sind 48 % der bestätigten Krater polygonal, auf Dione 59 %, auf Tethys 34 %, auf Ceres 70 % und auf Vesta 56 %. Die durchschnittliche Anzahl an geraden Segmenten ergibt 2.9 für Rhea, 3.4 für Dione, 3.1 für Tethys, 3.5 für Ceres und 3.2 für Vesta, das heißt, dass die meisten PICs zwei oder drei gerade Segmente aufweisen und nur wenige PICs hexagonal oder pentagonal sind. Da für Ceres und Vesta keine hochaufgelösten Aufnahmen der Polargebiete vorhanden sind und um Projektionseffekte auszuschließen, wurde für die Berechnung der Winkel zwischen den geraden Segmenten nur PICs zwischen Breitengraden von 60° und -60° berücksichtigt. Der durchschnittliche Winkel zwischen den geraden Segmenten ergibt 121° für Rhea, 124° für Dione, 123° für Tethys, 133° für Ceres und 134° für Vesta. Da es viel mehr unbestätigte als bestätigte Krater auf den untersuchten Himmelskörpern gibt, wurde auch der Prozentanteil an PICs zwischen Breitengraden von -60° bis 60° bestimmt, was zu 44 % für Rhea, 50 % für Dione, 51 % für Tethys, 61 % für Ceres und 55 % für Vesta führt.

Die Ergebnisse zur Durchschnittsanzahl an geraden Segmenten und deren Winkel sind in guter Übereinstimmung zu früheren Untersuchungen und auch die Vermutung, dass Polygonalität häufiger bei kleineren und mittelgroßen Kratern vorzufinden ist, wurde bestätigt. Die Arbeit zeigt, dass es eine hohe Anzahl an polygonalen Einschlagskratern auf Rhea, Dione, Tethys, Ceres und Vesta gibt, jedoch ist unklar, wieso der Prozentanteil an PICs auf diesen Himmelskörpern um einiges höher ist als auf den terrestrischen Planeten und dem Mond. Eine mögliche Erklärung könnte die unterschiedliche Oberflächenzusammensetzung dieser Himmelskörper im Vergleich zu der von terrestrischen Planeten und dem Mond sein, aber für eine endgültige Antwort zu dieser Frage ist ein besseres Verständnis der genauen Entstehungsprozesse von PICs, die bis jetzt unklar sind, notwendig.

Appendix

Table 9.11 showing all approved impact craters on Rhea from the IAU/NASA/USGS Planetary Database, including their diameters and coordinates. Unknown diameters of impact craters were measured by the author and are marked as (*).

Nr.	Crater	Diameter (km)	Centre Longitude (°)	Centre Latitude (°)
1	Aananin	52*	34.9	339.9
2	Abassi	87.2	-21.3	146.5
3	Adjua	46*	40.2	118.9
4	Agunua	60*	63.3	66.2
5	Ambat	42.9	-76.4	301.7
6	Ameta	47*	53.3	21.9
7	Amma	31.4	-26.4	282.7
8	Amotken	64.6	0.7	202.7
9	Anansi	49	-63	213.6
10	Anguta	46.7	25.7	190
11	Arunaka	40*	-15.3	22.1
12	Atabei	30.4	16	250.7
13	Atum	67.5*	-47.1	1.1
14	Awonawilona	49.8	-37.3	150.3
15	Bulagat	72.5*	-38.2	15.2
16	Bumba	127.5*	63.1	50.4
17	Burkhan	32.5*	66.8	310.6
18	Chingaso	47.8	-17.1	106
19	Con	77.5*	-25.8	12.7
20	Dangun	77.5	7.2	208
21	Djuli	105*	-31.2	46.7
22	Dohitt	93.4	-18	74.1
23	Dotet	40.4	-45.9	204.7
24	Ehecatl	93.6	-54.7	175.6
25	Ellyay	105*	71.4	91.8
26	Enkai	48.4	38	246.3
27	Faro	63.5*	45.3	114
28	Fatu	88	7.7	176.1
29	Fuxi	47.2	-5.5	124.2
30	Gborogboro	62.5	-12.7	162.2
31	Glooskap	63.2	-35	57.2
32	Gmerti	57.2	-52	192.6
33	Gucumatz	68.6	37	175.8
34	Haik	75*	-36.6	29.3

Nr.	Crater	Diameter (km)	Centre Longitude (°)	Centre Latitude (°)
35	Haoso	72.5*	8.3	12.5
36	Heller	75*	10.1	315.1
37	Huracan	71.2	53.2	188.5
38	Imberombera	47.2	-33.3	216.7
39	Imra	28	19	134.2
40	Inktomi	47.2	-14.1	112.1
41	Inmar	54.8	-2.3	301.6
42	Iraca	50*	39.4	112.1
43	Itciai	39.2	-17.8	349
44	Izanagi	240*	-49.4	310.2
45	Izanami	70*	-46.3	313.4
46	Jumo	37*	52.8	66.5
47	Juok	73.8	37.6	155
48	Kanobo	75.8	-63.8	37.4
49	Karora	55*	5.9	20.1
50	Karusakaibo	43.4	-14.2	220.7
51	Khado	44*	41.6	359.1
52	Khutsau	52.4	44.5	206.9
53	Kiho	97.5*	-11.1	358.7
54	Kuksu	34.6	25.3	288.7
55	Kuma	50	10	277.2
56	Kumpara	49*	9.6	327.1
57	Kurkyl	57.1	-39.9	113.7
58	Leza	75*	-21.8	309.2
59	Ligoupup	78.8	-14.5	46.2
60	Lowa	35*	40.9	16.6
61	Lowalangi	53	-36.5	250
62	Luli	52.4	46.5	243.1
63	Lumawig	49.8	58	136.5
64	Madumda	82.6	-36.9	64.8
65	Maheo	29.8	31.6	281.7
66	Malunga	36*	65.1	56.2
67	Mamaldi	480	14	184
68	Manoid	35*	29.5	8.5
69	Mbir	46	46.6	311.9
70	Melo	75*	-53.2	7.1
71	Mubai	38*	55.8	20.2
72	Mumbi	67.2	-1.9	131.2
73	Nainema	53.8	25.5	346.4
74	Napi	55.8	26.9	174.8
75	Nareau	73.6	-24.9	241.9
76	Ndu	33.4	-22.4	291.3

Nr.	Crater	Diameter (km)	Centre Longitude (°)	Centre Latitude (°)
77	Nishanu	103.4	-9	129
78	Nishke	74.2	3.8	49
79	Num	48*	24	92.7
80	Nzame	119.4	9	24.9
81	Obatala	67.2	-1.1	269.7
82	Olorun	58.4	24.7	155.4
83	Ormazd	145*	52.5	58.5
84	Pachacamac	46.8	-23.4	83.7
85	Pan Ku	41*	65.7	107.7
86	Pedn	36*	46	351.7
87	Pokoh	45.2	-71.7	326.4
88	Pouliuli	59.8	-16.9	284.4
89	Powehiwehi	271.2	-8.2	280.4
90	Puntan	33	33.9	292.4
91	Purusa	96.7	-21.2	167.8
92	Qat	102.5*	-23.8	351.6
93	Quwai	38.8	19.6	66
94	Samni	101.4	-47.7	90.7
95	Seveki	89.1	12.9	164.7
96	Shedi	47.6	-53.5	346.8
97	Sholmo	48*	12	346.4
98	Shuzanghu	47.8	-74.9	10.3
99	Singbonga	60.8	-54.8	146.9
100	Taaroa	52*	16.5	95.5
101	Talapas	51.6	-16.7	341.8
102	Tane	82.6	-12.5	57.4
103	Tasheting	60.8	-59	55.5
104	Tawa	62.2	17.9	175.2
105	Thunupa	49*	45.6	21.3
106	Tika	57*	25.1	84.1
107	Tirawa	390*	34.2	151.7
108	Tore	2.85*	0	340
109	Torom	48*	-72.5	343
110	Tsuki-Yomi	35	35	43.8
111	Tulpar	70.4	56.1	158.6
112	Tuwale	59.6	-78	242.4
113	Uku	56*	78.7	95.5
114	Utleygon	58.2	-20.1	194.9
115	Vatea	96.6	16	150.4
116	Wak	57.8	29.6	194.3
117	Wakonda	123	48.6	269.7
118	Wende	83	-56.3	226.4

Nr.	Crater	Diameter (km)	Centre Longitude (°)	Centre Latitude (°)
119	Whanin	57*	66.9	115
120	Woyengi	43	13.7	294.5
121	Wulbari	33	67	88.9
122	Wuraka	45*	25.1	4
123	Xamba	100*	2.1	349.7
124	Xowalaci	60	2.4	56.3
125	Xu	63*	55	71.9
126	Yehl	36.8	38	322.4
127	Yu-Ti	70*	50.1	81.5
128	Zicum	76.8	-50.9	111.2

Table 9.11: All approved impact craters on Rhea, including their diameters and coordinates. Missing diameters of craters in the IAU/NASA/USGS Planetary Database were measured by the author and are marked as (*).

Table 9.12 shows all identified PICs on Rhea from the Planetary Database, including their diameters and coordinates. Craters whose diameters were measured by the author are marked as (*).

Nr.	Crater	Diameter (km)	Centre Longitude (°)	Centre Latitude (°)
1	Aananin	52*	34.9	339.9
2	Abassi	87.2	-21.3	146.5
3	Adjua	46*	40.2	118.9
4	Agunua	60*	63.3	66.2
5	Ambat	42.9	-76.4	301.7
6	Ameta	47*	53.3	21.9
7	Amma	31.4	-26.4	282.7
8	Amotken	64.6	0.7	202.7
9	Arunaka	40*	-15.3	22.1
10	Awonawilona	49.8	-37.3	150.3
11	Con	77.5*	-25.8	12.7
12	Dangun	77.5	7.2	208
13	Dotet	40.4	-45.9	204.7
14	Enkai	48.4	38	246.3
15	Faro	63.5*	45.3	114
16	Fatu	88	7.7	176.1
17	Gborogboro	62.5	-12.7	162.2
18	Gucumatz	68.6	37	175.8
19	Haik	75*	-36.6	29.3
20	Haoso	72.5*	8.3	12.5
21	Heller	75*	10.1	315.1
22	Inmar	54.8	-2.3	301.6
23	Iraca	50*	39.4	112.1

Nr.	Crater	Diameter (km)	Centre Longitude (°)	Centre Latitude (°)
24	Itciai	39.2	-17.8	349
25	Izanami	70*	-46.3	313.4
26	Karusakaibo	43.4	-14.2	220.7
27	Khado	44*	41.6	359.1
28	Kuksu	34.6	25.3	288.7
29	Kuma	50	10	277.2
30	Kumpara	49*	9.6	327.1
31	Ligoupup	78.8	-14.5	46.2
32	Lowa	35*	40.9	16.6
33	Maheo	29.8	31.6	281.7
34	Malunga	36*	65.1	56.2
35	Mubai	38*	55.8	20.2
36	Ndu	33.4	-22.4	291.3
37	Nishke	74.2	3.8	49
38	Num	48*	24	92.7
39	Nzame	119.4	9	24.9
40	Obatala	67.2	-1.1	269.7
41	Pachacamac	46.8	-23.4	83.7
42	Pan Ku	41*	65.7	107.7
43	Pedn	36*	46	351.7
44	Pokoh	45.2	-71.7	326.4
45	Pouliuli	59.8	-16.9	284.4
46	Puntan	33	33.9	292.4
47	Purusa	96.7	-21.2	167.8
48	Qat	102.5*	-23.8	351.6
49	Quwai	38.8	19.6	66
50	Samni	101.4	-47.7	90.7
51	Talapas	51.6	-16.7	341.8
52	Tane	82.6	-12.5	57.4
53	Tasheting	60.8	-59	55.5
54	Tika	57*	25.1	84.1
55	Tuwale	59.6	-78	242.4
56	Uku	56*	78.7	95.5
57	Wak	57.8	29.6	194.3
58	Woyengi	43	13.7	294.5
59	Xamba	100*	2.1	349.7
60	Xowalaci	60	2.4	56.3
61	Zicum	76.8	-50.9	111.2

Table 9.12: Identified polygonal impact craters on Rhea from the IAU/NASA/USGS Planetary Database. The values for crater diameter, centre latitude, and centre longitude are taken from the IAU/NASA/USGS Planetary Database. Unknown diameters of 24 PICs were measured by the author and are marked as (*).

Table 9.13 showing all approved impact craters on Dione from the IAU/NASA/USGS Planetary Database, including their diameters and coordinates.

Nr.	Crater	Diameter (km)	Centre Longitude (°)	Centre Latitude (°)
1	Acestes	108	50.1	243.37
2	Adrastus	38.5	-61.66	46.57
3	Aeneas	161	25.89	46.27
4	Alcander	120	-52.89	295.49
5	Allecto	106	-7.73	224.56
6	Amastrus	62.4	-9.96	237.03
7	Amata	76	5.17	279.81
8	Amycus	27.3	-37.52	88.62
9	Anchises	47	-34	65
10	Anna	14.2	-63.38	89.96
11	Antenor	81	-7	11.54
12	Ascanius	98	33.43	232.18
13	Assaracus	60	32.65	8.79
14	Aulestes	50	9.9	147.73
15	Butes	35	65.72	46.4
16	Caieta	50	-24.71	79.63
17	Camilla	31.9	-4.36	60.61
18	Cassandra	13	-39.84	246.22
19	Catillus	42.2	-2.38	275.3
20	Coras	43	0.39	268.45
21	Cretheus	29	-43.35	88.53
22	Creusa	36.2	49.19	76.32
23	Daucus	80	-15.38	301.14
24	Dercennus	86.2	29.75	279.93
25	Dido	122	-23.97	18.82
26	Entellus	63	-10.93	210.54
27	Erulus	120	-35	104.76
28	Eumelus	35.1	-0.1	65.96
29	Euryalus	35	-74.36	0
30	Evander	350	-57	145
31	Fadus	47	-35.94	225.18
32	Galaesus	79	46.77	296.25
33	Haemon	65.22	84.33	276.31
34	Halys	35.2	-59.17	53.72
35	Herbesus	58.4	34.68	156.11
36	Iasus	54	-22.13	245.92
37	Ilia	52.4	-0.5	346.27
38	Italus	35.7	-18.47	76.41
39	Lagus	77	-13.56	102.95

Nr.	Crater	Diameter (km)	Centre Longitude (°)	Centre Latitude (°)
40	Lamyrus	61	53.67	255.61
41	Larides	29	7.17	311.42
42	Latagus	41	14.65	26.46
43	Latinus	130	52.19	201
44	Lausus	23.5	34.81	22.76
45	Liger	53	24	126.63
46	Lucagus	45.7	22.15	131.25
47	Magus	45.8	18.44	24.35
48	Massicus	39	-35	55.39
49	Metiscus	43.8	6	93.29
50	Mezentius	51	19.16	183
51	Murranus	56.8	12.82	90.73
52	Nisus	35	-68.18	335
53	Oebalus	35.7	44.47	351.6
54	Pagasus	67	-3	241
55	Palinurus	11.9	-3.3	63
56	Phaleris	44	-77.4	166.58
57	Phorbas	69.3	81.2	131.29
58	Prytanis	96	-46.25	287.4
59	Remus	62	-13.58	31.9
60	Ripheus	34	-56.47	36.8
61	Romulus	90.7	-8.15	26.85
62	Sabinus	88	-43.65	186.66
63	Sagaris	53	4.93	104.2
64	Salius	44	65.09	181.73
65	Silvius	74	-32.7	332.26
66	Sulmo	56	55.92	333.5
67	Telon	39.7	-16.2	97.2
68	Tereus	45	-2.6	245
69	Thymber	27.29	14	309.15
70	Tiburtus	59	29.11	189.73
71	Turnus	101	15.59	345.31
72	Tyrrhus	49.1	24.7	287.9
73	Volcens	74	-13.84	268.51

Table 9.13: All approved impact craters on Dione, including their diameters and coordinates, according to the IAU/NASA/USGS Planetary Database.

Table 9.14 showing all identified PICs on Dione from the IAU/NASA/USGS Planetary Database, including their diameters and coordinates.

Nr.	Crater	Diameter (km)	Centre Longitude (°)	Centre Latitude (°)
1	Acestes	108	50.1	243.37
2	Adrastus	38.5	-61.66	46.57
3	Alcander	120	-52.89	295.49
4	Allecto	106	-7.73	224.56
5	Amastrus	62.4	-9.96	237.03
6	Amycus	27.3	-37.52	88.62
7	Anchises	47	-34	65
8	Anna	14.2	-63.38	89.96
9	Antenor	81	-7	11.54
10	Assaracus	60	32.65	8.79
11	Caieta	50	-24.71	79.63
12	Camilla	31.9	-4.36	60.61
13	Catillus	42.2	-2.38	275.3
14	Coras	43	0.39	268.45
15	Cretheus	29	-43.35	88.53
16	Dido	122	-23.97	18.82
17	Entellus	63	-10.93	210.54
18	Euryalus	35	-74.36	0
19	Fadus	47	-35.94	225.18
20	Galaesus	79	46.77	296.25
21	Haemon	65.22	84.33	276.31
22	Halys	35.2	-59.17	53.72
23	Herbesus	58.4	34.68	156.11
24	Ilia	52.4	-0.5	346.27
25	Italus	35.7	-18.47	76.41
26	Lamyrus	61	53.67	255.61
27	Lausus	23.5	34.81	22.76
28	Magus	45.8	18.44	24.35
29	Massicus	39	-35	55.39
30	Mezentius	51	19.16	183
31	Oebalus	35.7	44.47	351.6
32	Pagasus	67	-3	241
33	Prytanis	96	-46.25	287.4
34	Remus	62	-13.58	31.9
35	Ripheus	34	-56.47	36.8
36	Romulus	90.7	-8.15	26.85
37	Sabinus	88	-43.65	186.66
38	Sagaris	53	4.93	104.2
39	Silvius	74	-32.7	332.26
40	Telon	39.7	-16.2	97.2
41	Thymber	27.29	14	309.15

Nr.	Crater	Diameter (km)	Centre Longitude (°)	Centre Latitude (°)
42	Tiburtus	59	29.11	189.73
43	Volcens	74	-13.84	268.51

Table 9.14: Found PICs on Dione of all approved craters on the IAU/NASA/USGS Planetary Database with their diameters, centre latitudes, and centre longitudes. Values for the diameters and coordinates are taken from the IAU/NASA/USGS Planetary Database.

Table 9.15 showing all approved impact craters on Tethys from the IAU/NASA/USGS Planetary Database, including their diameters and coordinates.

Nr.	Crater	Diameter (km)	Centre Longitude (°)	Centre Latitude (°)
1	Achilles	58.6	0.6	324.38
2	Aietes	91	-41.44	6.23
3	Ajax	88	-28.41	282
4	Alcinous	50	30.31	212.61
5	Amphinomus	13.6	-14.87	128.7
6	Anticleia	100.7	51.31	32.37
7	Antinous	138	-59.89	286.15
8	Arete	13	-4.67	299
9	Circe	79	-12.6	54.66
10	Demodocus	125	-59.37	18.21
11	Diomedes	48.57	38.12	289.42
12	Dolius	190	-30.15	210.33
13	Elpenor	60	53.43	263.69
14	Euanthes	33	7.86	238.91
15	Eumaeus	30	23.1	51.12
16	Eupithes	22.3	18.71	171.21
17	Eurycleia	31	52.54	246.5
18	Eurylochus	44.8	-5.07	27.68
19	Eurymachus	38.4	-35.65	65
20	Halius	29.5	44.4	4.96
21	Hermione	68.2	-38.4	148.69
22	Icarius	54.4	-5.89	305.85
23	Irus	26.5	-27	244.81
24	Laertes	51.13	-46.36	67.46
25	Leocritus	12.5	21.53	118.66
26	Leucothea	13.8	-4.26	123.84
27	Maron	11.8	2.52	119.33
28	Medon	18.7	25.5	143.31
29	Melanthius	250	-58.5	192.61
30	Mentor	62	0.25	44.16

Nr.	Crater	Diameter (km)	Centre Longitude (°)	Centre Latitude (°)
31	Naubolos	54.5	-72.19	305.18
32	Nausicaa	69	84.4	5
33	Neleus	37.6	-19.38	25.72
34	Nestor	38.2	-54	64.81
35	Odysseus	445	32.82	128.89
36	Oenops	25.7	28.13	93.44
37	Ormenus	39.8	-20.39	43.85
38	Penelope	207.5	-10.83	249.22
39	Periboea	51	8	34.86
40	Phemius	75.9	11.32	286.22
41	Philoetius	28.3	2.32	184.71
42	Polycaste	23	1.38	86.41
43	Polyphemus	73	-3.48	282.98
44	Poseidon	63	-55.71	101.3
45	Rhexenor	38	-75.63	65.22
46	Salmoneus	93	-1.77	335.18
47	Teiresias	14.5	60.39	0.83
48	Telemachus	92	54	339.38
49	Telemus	320	-34.53	356.89
50	Theoclymenus	34.3	-14.43	205.63

Table 9.15: All approved impact craters on Tethys from the IAU/NASA/USGS Planetary Database, including their diameters and coordinates.

Table 9.16 showing all identified PICs on Tethys from the IAU/NASA/USGS Planetary Database, including their diameters and coordinates.

Nr.	Crater	Diameter (km)	Centre Longitude (°)	Centre Latitude (°)
1	Achilles	58.6	0.6	324.38
2	Ajax	88	-28.41	282
3	Alcinous	50	30.31	212.61
4	Antinous	138	-59.89	286.15
5	Arete	13	-4.67	299
6	Euanthes	33	7.86	238.91
7	Eupithes	22.3	18.71	171.21
8	Eurylochus	44.8	-5.07	27.68
9	Eurymachus	38.4	-35.65	65
10	Halius	29.5	44.4	4.96
11	Icarius	54.4	-5.89	305.85
12	Irus	26.5	-27	244.81
13	Leocritus	12.5	21.53	118.66
14	Naubolos	54.5	-72.19	305.18

Nr.	Crater	Diameter (km)	Centre Longitude (°)	Centre Latitude (°)
15	Neleus	37.6	-19.38	25.72
16	Odysseus	445	32.82	128.89
17	Ormenus	39.8	-20.39	43.85

Table 9.16: Found polygonal impact craters on Tethys, including their diameters, centre latitudes, and centre longitudes. Values for the crater diameters, the centre longitudes, and the centre latitudes have been obtained from the IAU/NASA/USGS Planetary Database.

Table 9.17 showing all approved impact craters on Ceres from the IAU/NASA/USGS Planetary Database, including their diameters and coordinates.

Nr.	Crater	Diameter (km)	Centre Longitude (°)	Centre Latitude (°)
1	Abellio	32	33.2	293.09
2	Achita	40	25.82	65.96
3	Annona	60	-48.14	8.43
4	Anura	37	-13.92	11.79
5	Aristaeus	35.8	23.43	97.68
6	Asari	56	82.88	319.53
7	Attis	22	-73.1	257.55
8	Azacca	49.91	-6.66	218.4
9	Bagbalel	102	17.71	325.35
10	Belun	36.04	-33.71	356.25
11	Besua	17	-42.35	300.21
12	Bonsu	31	1.74	93.21
13	Braciaca	8	-22.77	84.37
14	Cacaguat	13.6	-1.19	143.61
15	Centeotl	6	18.95	141.22
16	Chaminuka	122	-58.58	131.2
17	Coniraya	135	39.9	65.73
18	Consus	64	-20.7	200.5
19	Cozobi	24	45.33	287.31
20	Dada	12	58.63	336.76
21	Dantu	126	24.3	138.23
22	Darzamat	92	-44.21	76.4
23	Datan	60	59.5	252.31
24	Doliku	15	-40.79	5.88
25	Duginavi	155	39.2	4.29
26	Ernutet	53.4	52.93	45.52
27	Ezinu	116	43.24	195.7
28	Fejokoo	68	29.15	312.11
29	Fluusa	60	-31.31	178.22

Nr.	Crater	Diameter (km)	Centre Longitude (°)	Centre Latitude (°)
30	Gaue	80	30.81	86.16
31	Geshtin	80	57	258.81
32	Ghanan	68	76.51	30.8
33	Hakumyi	29.2	51.42	27.75
34	Hamori	60	-60.86	79.44
35	Hatipowa	40	-16.08	357.71
36	Haulani	34	5.8	10.77
37	Heneb	39	10.87	191.04
38	Homshuk	70	11.23	94.06
39	Ialonus	16.5	48.15	168.53
40	Ikapati	50	33.84	45.61
41	Inamahari	68	14.13	89.22
42	Insitor	26	-10.71	124.87
43	Jaja	22	52.09	125.27
44	Jarimba	69	-24.08	21.25
45	Jarovit	66	67.9	284.74
46	Juling	20	-35.9	168.48
47	Kaikara	72	42.82	222.43
48	Kait	0.4	-2.1	0
49	Kerwan	280	-10.77	123.99
50	Kiriamma	18.7	50.32	126.33
51	Kirnis	115	4.9	264.3
52	Kondos	44	-19.34	17.31
53	Kumitoga	96	-10.09	178.83
54	Kupalo	26	-39.44	173.2
55	Laukumate	29.7	65.03	159.42
56	Liber	23	42.56	37.8
57	Lociyo	37.8	-6.53	228.83
58	Lono	20	-36.61	304.37
59	Meanderi	103	-40.8	194.19
60	Megwomets	78.7	36.54	146.22
61	Messor	40	49.93	233.73
62	Mondamin	126	-62.24	354
63	Nawish	77	18.28	193.79
64	Nepen	26.4	6.19	220.54
65	Ninsar	40	30.3	263.26
66	Occator	92	19.82	239.33
67	Oltagon	28	-25.95	37.96
68	Omonga	77	58.03	71.67
69	Oxo	10	42.21	359.6
70	Piuku	31	-15.37	36.99
71	Rao	12	8.1	119.01

Nr.	Crater	Diameter (km)	Centre Longitude (°)	Centre Latitude (°)
72	Razeka	38.38	-3.21	61.63
73	Rongo	68	3.21	348.71
74	Roskva	22	58.9	333.02
75	Sekhet	40	-66.42	255.05
76	Shakaema	47	-3.66	33.93
77	Sintana	58	-48.07	46.2
78	Tafakula	34	-19.82	88.59
79	Tahu	25	-6.59	44.79
80	Takel	22	50.76	280.48
81	Tawals	8.8	-39.06	238.02
82	Tibong	36	-29.82	352.2
83	Toharu	86	-48.32	155.95
84	Tupo	36	-32.35	88.38
85	Urvara	170	-45.66	249.24
86	Victa	32	36.23	301.04
87	Vinotonus	140	43.02	95.12
88	Xochipilli	22.7	56.66	93.21
89	Yalode	260	-42.58	292.48
90	Zadeni	129.28	-70.36	38.34

Table 9.17: All approved impact craters on Ceres from the IAU/NASA/USGS Planetary Database, including their diameters and coordinates.

Table 9.18 showing all identified PICs on Ceres from the IAU/NASA/USGS Planetary Database, including their diameters and coordinates.

Nr.	Crater	Diameter (km)	Centre Longitude (°)	Centre Latitude (°)
1	Abellio	32	33.2	293.09
2	Achita	40	25.82	65.96
3	Annona	60	-48.14	8.43
4	Anura	37	-13.92	11.79
5	Azacca	49.91	-6.66	218.4
6	Belun	36.04	-33.71	356.25
7	Besua	17	-42.35	300.21
8	Bonsu	31	1.74	93.21
9	Braciaca	8	-22.77	84.37
10	Cacaguat	13.6	-1.19	143.61
11	Chaminuka	122	-58.58	131.2
12	Coniraya	135	39.9	65.73
13	Consus	64	-20.7	200.5
14	Cozobi	24	45.33	287.31
15	Dada	12	58.63	336.76

Nr.	Crater	Diameter (km)	Centre Longitude (°)	Centre Latitude (°)
16	Dantu	126	24.3	138.23
17	Darzamat	92	-44.21	76.4
18	Doliku	15	-40.79	5.88
19	Ernutet	53.4	52.93	45.52
20	Ezinu	116	43.24	195.7
21	Fejokoo	68	29.15	312.11
22	Gaue	80	30.81	86.16
23	Hamori	60	-60.86	79.44
24	Hatipowa	40	-16.08	357.71
25	Haulani	34	5.8	10.77
26	Homshuk	70	11.23	94.06
27	Ialonus	16.5	48.15	168.53
28	Inamahari	68	14.13	89.22
29	Insitor	26	-10.71	124.87
30	Jaja	22	52.09	125.27
31	Jarimba	69	-24.08	21.25
32	Jarovit	66	67.9	284.74
33	Juling	20	-35.9	168.48
34	Kaikara	72	42.82	222.43
35	Kerwan	280	-10.77	123.99
36	Kiriamma	18.7	50.32	126.33
37	Kirnis	115	4.9	264.3
38	Kondos	44	-19.34	17.31
39	Kupalo	26	-39.44	173.2
40	Liber	23	42.56	37.8
41	Lociyo	37.8	-6.53	228.83
42	Lono	20	-36.61	304.37
43	Meanderi	103	-40.8	194.19
44	Messor	40	49.93	233.73
45	Nawish	77	18.28	193.79
46	Nepen	26.4	6.19	220.54
47	Ninsar	40	30.3	263.26
48	Oltagon	28	-25.95	37.96
49	Oxo	10	42.21	359.6
50	Piuku	31	-15.37	36.99
51	Razeka	38.38	-3.21	61.63
52	Rao	12	8.1	119.01
53	Roskva	22	58.9	333.02
54	Shakaema	47	-3.66	33.93
55	Sintana	58	-48.07	46.2
56	Tafakula	34	-19.82	88.59
57	Tahu	25	-6.59	44.79

Nr.	Crater	Diameter (km)	Centre Longitude (°)	Centre Latitude (°)
58	Takel	22	50.76	280.48
59	Tawals	8.8	-39.06	238.02
60	Tibong	36	-29.82	352.2
61	Tupo	36	-32.35	88.38
62	Victa	32	36.23	301.04
63	Xochipilli	22.7	56.66	93.21

Table 9.18: Found polygonal impact craters on Ceres of all the approved craters on the IAU/NASA/USGS Planetary Database. Values for crater diameter, centre longitude, and centre latitude are taken from the IAU/NASA/USGS Planetary Database.

Table 9.19 showing all approved impact craters on Vesta from the IAU/NASA/USGS Planetary Database, including their diameters and coordinates.

Nr.	Crater	Diameter (km)	Centre Longitude (°)	Centre Latitude (°)
1	Aconia	19	7.54	151.37
2	Aelia	4.34	-14.26	290.8
3	Africana	25.43	68.99	345.87
4	Albana	90.86	76.61	200.69
5	Albia	5.79	-27.85	78.85
6	Alypia	15.17	-70.22	139.22
7	Angioletta	18.42	-40.16	179.25
8	Antonia	16.75	-58.7	350.78
9	Aquilia	36.82	-49.41	190.88
10	Arruntia	10.49	39.44	221.59
11	Bellicia	41.68	37.73	197.76
12	Bruttia	20.68	63.81	237.09
13	Caesonia	104.23	31.2	249.93
14	Calpurnia	50.19	16.72	349.1
15	Cannutia	17.97	-58.93	214.73
16	Canuleia	11.32	-33.62	84.52
17	Caparronia	53.2	35.71	317.03
18	Charito	6.55	-44.8	90.71
19	Claudia	0.57	-1.65	146
20	Coelia	14.06	-1.14	239.82
21	Cornelia	14.9	-9.37	15.57
22	Cossinia	15.72	0.63	178.96
23	Domitia	32.99	37.62	337.96
24	Domna	13.53	-11.11	225.93
25	Drusilla	20.34	-15.05	51.22
26	Eumachia	25.78	0.14	317.06

Nr.	Crater	Diameter (km)	Centre Longitude (°)	Centre Latitude (°)
27	Eusebia	23.44	-42.04	354.31
28	Eutropia	21.09	22.4	255.01
29	Fabia	11.62	15.53	55.76
30	Fausta	3.14	-25.44	99.76
31	Flavola	2.87	-9.16	329.56
32	Floronia	18.54	36.23	94.06
33	Fonteia	20.61	-53.25	291.41
34	Fulvia	16.73	-26.13	292.65
35	Fundania	29.23	57.62	285.02
36	Galeria	21.77	-29.82	18.38
37	Gegania	22.33	4.05	210.77
38	Graecina	11.93	-37.45	237.01
39	Helena	22.06	-41.51	272.55
40	Herennia	22.33	-72.42	10.33
41	Hortensia	29.45	-46.85	165.38
42	Iuinia	3.03	-35.58	238.22
43	Justina	7.62	-34.41	107.88
44	Laelia	8.89	-46.82	290.45
45	Laeta	1.37	14.9	329.9
46	Laurentia	11.48	-28.15	92.8
47	Lepida	42.9	16.74	96.76
48	Licinia	24.05	23.34	167.35
49	Lollia	4.9	-37.36	242.33
50	Longina	17.65	36.96	20.65
51	Lucilla	19.3	-75.96	299.12
52	Mamilia	35.67	48.39	82.09
53	Marcia	67.6	8.98	339.55
54	Mariamne	30.33	-68.44	350.73
55	Metrodora	23.99	-59.43	100.54
56	Minervina	18.34	16.85	199.29
57	Minucia	23.15	20.2	357.2
58	Myia	2.59	-50.53	256.34
59	Numisia	29.94	-7.48	37.25
60	Occia	7.34	-15.47	168.48
61	Octavia	30.62	-3.3	297.21
62	Oppia	36.67	-7.89	99.08
63	Paculla	22.34	-64.22	151.15
64	Paulina	18.13	10.92	133.11
65	Perpennia	21.36	-23.03	258.75
66	Pinaria	41.76	-29.54	181.63
67	Placidia	14.75	19.24	281.38
68	Plancia	18.48	61.56	343.91

Nr.	Crater	Diameter (km)	Centre Longitude (°)	Centre Latitude (°)
69	Pomponia	59.07	70.2	262.58
70	Portia	11.44	0.91	191.17
71	Postumia	195.89	33.84	33.77
72	Publicia	15.79	14.53	234.36
73	Rheasilvia	450	-71.95	86.3
74	Rubria	10.27	-7.32	168.34
75	Rufillia	15.79	-12.92	288.71
76	Scantia	18.61	29.63	64.65
77	Sentia	16.54	-38.39	170.75
78	Serena	18.47	-20.43	270.71
79	Severina	34.74	-75.41	271.55
80	Sextilia	19.48	-39	295.93
81	Sossia	8.11	-36.78	75.76
82	Tarpeia	40.29	-69.47	179.3
83	Teia	6.69	-3.44	61.06
84	Torquata	34.73	46.45	143.78
85	Tuccia	11.65	-39.86	346.81
86	Urbinia	24.25	-29.88	66.26
87	Varronilla	158.45	29.62	179.58
88	Veneneia	400	-47.93	305.68
89	Vettenia	18.89	4.8	229.31
90	Vibidia	7.1	-26.96	10.3

Table 9.19: All approved impact craters on Vesta from the IAU/NASA/USGS Planetary Database, including their diameters and coordinates. Values for the diameters and coordinates are taken from the IAU/NASA/USGS Planetary Database.

Table 9.20 showing all identified PICs on Vesta from the IAU/NASA/USGS Planetary Database.

Nr.	Crater	Diameter (km)	Centre Longitude (°)	Centre Latitude (°)
1	Aconia	19	7.54	151.37
2	Aelia	4.34	-14.26	290.8
3	Albia	5.79	-27.85	78.85
4	Aquilia	36.82	-49.41	190.88
5	Arruntia	10.49	39.44	221.59
6	Bellicia	41.68	37.73	197.76
7	Canuleia	11.32	-33.62	84.52
8	Caparronia	53.2	35.71	317.03
9	Coelia	14.06	-1.14	239.82
10	Cornelia	14.9	-9.37	15.57
11	Cossinia	15.72	0.63	178.96
12	Domna	13.53	-11.11	225.93

Nr.	Crater	Diameter (km)	Centre Longitude (°)	Centre Latitude (°)
13	Drusilla	20.34	-15.05	51.22
14	Eumachia	25.78	0.14	317.06
15	Eutropia	21.09	22.4	255.01
16	Fabia	11.62	15.53	55.76
17	Fausta	3.14	-25.44	99.76
18	Floronia	18.54	36.23	94.06
19	Fonteia	20.61	-53.25	291.41
20	Fulvia	16.73	-26.13	292.65
21	Galeria	21.77	-29.82	18.38
22	Gegania	22.33	4.05	210.77
23	Graecina	11.93	-37.45	237.01
24	Helena	22.06	-41.51	272.55
25	Herennia	22.33	-72.42	10.33
26	Hortensia	29.45	-46.85	165.38
27	Laelia	8.89	-46.82	290.45
28	Laurentia	11.48	-28.15	92.8
29	Lepida	42.9	16.74	96.76
30	Longina	17.65	36.96	20.65
31	Mamilia	35.67	48.39	82.09
32	Minervina	18.34	16.85	199.29
33	Numisia	29.94	-7.48	37.25
34	Oppia	36.67	-7.89	99.08
35	Paulina	18.13	10.92	133.11
36	Perpennia	21.36	-23.03	258.75
37	Pinaria	41.76	-29.54	181.63
38	Placidia	14.75	19.24	281.38
39	Publicia	15.79	14.53	234.36
40	Rubria	10.27	-7.32	168.34
41	Rufillia	15.79	-12.92	288.71
42	Scantia	18.61	29.63	64.65
43	Sextilia	19.48	-39	295.93
44	Sossia	8.11	-36.78	75.76
45	Tarpeia	40.29	-69.47	179.3
46	Torquata	34.73	46.45	143.78
47	Tuccia	11.65	-39.86	346.81
48	Urbinia	24.25	-29.88	66.26
49	Vettenia	18.89	4.8	229.31
50	Vibidia	7.1	-26.96	10.3

Table 9.20: Found polygonal impact craters on Vesta including their diameters, centre longitudes, and centre latitudes. The values for the diameters and coordinates are adapted from the IAU/NASA/USGS Planetary Database.

References

A. Abels. Investigation of impact structures in Finland (Söderfjärden, Lumparn, Lappajärvi) by digital integration of multidisciplinary geodata. January 2003.

J. E. M. Adler and J. W. Salisbury. Circularity of Lunar Craters. *Icarus*, 10:37–52, January 1969. doi: 10.1016/0019-1035(69)90006-2.

M. Aittola, T. Öhman, J. J. Leitner, and J. Raitala. The Characteristics of Polygonal Impact Craters on Venus. *Earth Moon and Planets*, 101:41–53, October 2007. doi: 10.1007/s11038-007-9148-4.

M. Aittola, T. Öhman, J. J. Leitner, V.-P. Kostama, and J. Raitala. The structural control of venusian polygonal impact craters. *Icarus*, 205:356–363, February 2010. doi: 10.1016/j.icarus.2009.08.004.

E. Ammannito, M. C. De Sanctis, F. Capaccioni, M. Teresa Capria, F. Carraro, J.-P. Combe, S. Fonte, A. Frigeri, S. P. Joy, A. Longobardo, G. Magni, S. Marchi, T. B. McCord, L. A. McFadden, H. Y. McSween, E. Palomba, C. M. Pieters, C. A. Polanskey, C. A. Raymond, J. M. Sunshine, F. Tosi, F. Zambon, and C. T. Russell. Vestan lithologies mapped by the visual and infrared spectrometer on Dawn. *Meteoritics and Planetary Science*, 48:2185–2198, November 2013a. doi: 10.1111/maps.12192.

E. Ammannito, M. C. De Sanctis, E. Palomba, A. Longobardo, D. W. Mittlefehldt, H. Y. McSween, S. Marchi, M. T. Capria, F. Capaccioni, A. Frigeri, C. M. Pieters, O. Ruesch, F. Tosi, F. Zambon, F. Carraro, S. Fonte, H. Hiesinger, G. Magni, L. A. McFadden, C. A. Raymond, C. T. Russell, and J. M. Sunshine. Olivine in an unexpected location on Vesta's surface. *Nature*, 504:122–125, December 2013b. doi: 10.1038/nature12665.

E. Ammannito, M. C. De Sanctis, J.-P. Combe, A. Frigeri, R. Jaumann, A. Longobardo, H. Y. McSween, E. Palomba, F. Tosi, C. A. Raymond, and C. T. Russell. Compositional variations in the Vestan Rheasilvia basin. *Icarus*, 259:194–202, October 2015. doi: 10.1016/j.icarus.2015.05.017.

J. D. Anderson and G. Schubert. Rhea's gravitational field and interior structure inferred from archival data files of the 2005 Cassini flyby. *Physics of the Earth and Planetary Interiors*, 178: 176–182, February 2010. doi: 10.1016/j.pepi.2009.09.003.

APOD. Astronomy Picture of the Day - 12 October 2005. Cratered Cliffs of Ice on Saturn's Tethys. `https://apod.nasa.gov/apod/ap051012.html`, 2005. Accessed: 2017-07-26.

APOD. Astronomy Picture of the Day - 30 May 2006. Ancient Craters on Saturn's Rhea. `https://apod.nasa.gov/apod/ap060530.html`, 2006. Accessed: 2017-07-25.

APOD. Astronomy Picture of the Day - 24 June 2008. Ithaca Chasma: The Great Rift on Saturn's Tethys. `https://apod.nasa.gov/apod/ap080624.html`, 2008. Accessed: 2017-07-26.

APOD. Astronomy Picture of the Day - 14 May 2015. Dwarf Planet, Bright Spot. `https://apod.nasa.gov/apod/ap150514.html`, 2015. Accessed: 2017-07-28.

S. W. Asmar, F. Nimmo, P. C. Thomas, and B. G. Bills. A Shape Model For Rhea and Implications for its Gravity Coefficients and Internal Structure. In *Lunar and Planetary Science Conference*, volume 40 of *Lunar and Planetary Science Conference*, page 2219, March 2009.

D. Baratoux, H. Samuel, C. Michaut, M. J. Toplis, M. Monnereau, M. Wieczorek, R. Garcia, and K. Kurita. Petrological constraints on the density of the Martian crust. *Journal of Geophysical Research (Planets)*, 119:1707–1727, July 2014. doi: 10.1002/2014JE004642.

A. T. Basilevsky and J. W. Head. The surface of Venus. *Reports on Progress in Physics*, 66:1699–1734, October 2003. doi: 10.1088/0034-4885/66/10/R04.

A. T. Basilevsky and J. W. Head. Impact craters on regional plains on Venus: Age relations with wrinkle ridges and implications for the geological evolution of Venus. *Journal of Geophysical Research (Planets)*, 111:E03006, March 2006. doi: 10.1029/2005JE002473.

C. B. Beddingfield, D. M. Burr, and L. T. Tran. Polygonal impact craters on Dione: Evidence for tectonic structures outside the wispy terrain. *Icarus*, 274:163–194, August 2016. doi: 10.1016/j.icarus.2016.03.020.

M. Beuthe. East-west faults due to planetary contraction. *Icarus*, 209:795–817, October 2010. doi: 10.1016/j.icarus.2010.04.019.

M. T. Bland. Predicted crater morphologies on Ceres: Probing internal structure and evolution. *Icarus*, 226:510–521, September 2013. doi: 10.1016/j.icarus.2013.05.037.

M. T. Bland, C. A. Raymond, P. M. Schenk, R. R. Fu, T. Kneissl, J. H. Pasckert, H. Hiesinger, F. Preusker, R. S. Park, S. Marchi, S. D. King, J. C. Castillo-Rogez, and C. T. Russell. Composition and structure of the shallow subsurface of Ceres revealed by crater morphology. *Nature Geoscience*, 9:538–542, July 2016. doi: 10.1038/ngeo2743.

T. J. Bowling. Crustal Stripping by Large Impacts on Asteroid 1 Ceres. In *79th Annual Meeting of the Meteoritical Society*, volume 1921 of *LPI Contributions*, page 6524, August 2016.

T. J. Bowling, F. J. Ciesla, S. Marchi, T. M. Davison, J. C. Castillo-Rogez, M. C. De Sanctis, C. A. Raymond, and C. T. Russell. Impact Induced Heating of Occator Crater on Asteroid 1 Ceres. In *Lunar and Planetary Science Conference*, volume 47 of *Lunar and Planetary Science Conference*, page 2268, March 2016.

D. L. Buczkowski, D. Y. Wyrick, K. A. Iyer, E. G. Kahn, J. E. C. Scully, A. Nathues, R. W. Gaskell, T. Roatsch, F. Preusker, P. M. Schenk, L. Le Corre, V. Reddy, R. A. Yingst, S. Mest, D. A. Williams, W. B. Garry, O. S. Barnouin, R. Jaumann, C. A. Raymond, and C. T. Russell. Large-scale troughs on Vesta: A signature of planetary tectonics. *Geophysics Research Letters*, 39:L18205, September 2012. doi: 10.1029/2012GL052959.

D. L. Buczkowski, D. Y. Wyrick, M. Toplis, R. A. Yingst, D. A. Williams, W. B. Garry, S. Mest, T. Kneissl, J. E. C. Scully, A. Nathues, M. C. De Sanctis, L. LeCorre, V. Reddy, M. Hoffmann, E. Ammannito, A. Frigeri, F. Tosi, F. Preusker, T. Roatsch, C. A. Raymond, R. Jaumann, C. M. Pieters, and C. T. Russell. The unique geomorphology and physical properties of the Vestalia Terra plateau. *Icarus*, 244:89–103, December 2014. doi: 10.1016/j.icarus.2014.03.035.

D. L. Buczkowski, P. M. Schenk, J. E. C. Scully, K. Otto, I. von der Gathen, D. A. Williams, S. C. Mest, R. Park, F. Preusker, R. Jaumann, T. Roatsch, T. Platz, A. Nathues, M. Hoffmann, M. Schaefer, S. Marchi, M. C. De Sanctis, C. A. Raymond, and C. T. Russell. Linear Structures on Ceres: Morphology, Orientation, and Possible Formation Mechanisms. In *Lunar and Planetary Science Conference*, volume 47 of *Lunar and Planetary Science Conference*, page 1262, March 2016.

B. J. Buratti, J. A. Mosher, and T. V. Johnson. Albedo and color maps of the Saturnian satellites. *Icarus*, 87:339–357, October 1990. doi: 10.1016/0019-1035(90)90138-Y.

B. J. Buratti, S. P. Faulk, J. A. Mosher, R. N. Clark, R. H. Brown, K. H. Baines, and P. D. Nicholson. A Search for Activity on Mimas, Tethys, and Dione with the Cassini Visual and Infrared Mapping Spectrometer. In *Lunar and Planetary Science Conference*, volume 41 of *Lunar and Planetary Science Conference*, page 1389, March 2010.

P. K. Byrne, P. M. Schenk, and P. J. McGovern. Tectonic Mapping of Rift Zones on Rhea, Tethys, and Dione. In *Lunar and Planetary Science Conference*, volume 46 of *Lunar and Planetary Science Conference*, page 2251, March 2015.

U. Carsenty, S. Schroeder, D. Buczkowski, R. Jaumann, C. Russell, and C. Raymond. The crater chains of Vesta — the global view. In K. Muinonen, A. Penttilä, M. Granvik, A. Virkki, G. Fedorets, O. Wilkman, and T. Kohout, editors, *Asteroids, Comets, Meteors 2014*, July 2014.

J. C. Castillo. Expected Constraints on Rhea's Interior from Cassini. In S. Mackwell and E. Stansbery, editors, *36th Annual Lunar and Planetary Science Conference*, volume 36 of *Lunar and Planetary Science Conference*, March 2005.

M. J. Cintala, C. A. Wood, S. U. Grenander, M. E. Dibner-Dunlap, T. A. Mutch, and J. W. Head. Mercury Crater Analyses: An Automated Data Gathering and Handling System. In C. H. Simonds and R. B. Merrill, editors, *Comparisons of Mercury and the Moon*, volume 262 of *LPI Contributions*, page 5, 1976.

R. N. Clark, J. M. Curchin, R. Jaumann, D. P. Cruikshank, R. H. Brown, T. M. Hoefen, K. Stephan, J. M. Moore, B. J. Buratti, K. H. Baines, P. D. Nicholson, and R. M. Nelson. Compositional mapping of Saturn's satellite Dione with Cassini VIMS and implications of dark material in the Saturn system. *Icarus*, 193:372–386, February 2008. doi: 10.1016/j.icarus.2007.08.035.

H. Clenet, M. Jutzi, J.-A. Barrat, E. I. Asphaug, W. Benz, and P. Gillet. A deep crust-mantle boundary in the asteroid 4 Vesta. *Nature*, 511:303–306, July 2014. doi: 10.1038/nature13499.

E. A. Cloutis, M. R. M. Izawa, L. Pompilio, V. Reddy, H. Hiesinger, A. Nathues, P. Mann, L. Le Corre, E. Palomba, and J. F. Bell. Spectral reflectance properties of HED meteorites + CM2 carbonaceous chondrites: Comparison to HED grain size and compositional variations and implications for the nature of low-albedo features on Asteroid 4 Vesta. *Icarus*, 223:850–877, April 2013. doi: 10.1016/j.icarus.2013.02.003.

J.-P. Combe, T. B. McCord, L. A. McFadden, S. Ieva, F. Tosi, A. Longobardo, A. Frigeri, M. C. De Sanctis, E. Ammannito, O. Ruesch, E. Palomba, M. Fulchignoni, C. A. Raymond, and C. T.

Russell. Composition of the northern regions of Vesta analyzed by the Dawn mission. *Icarus*, 259: 53–71, October 2015. doi: 10.1016/j.icarus.2015.04.026.

J.-P. Combe, T. B. McCord, F. Tosi, A. Raponi, M. C. De Sanctis, E. Ammannito, C. A. Raymond, and C. T. Russell. Detection of H2O-Rich Materials on Ceres by the Dawn Mission. In *Lunar and Planetary Science Conference*, volume 47 of *Lunar and Planetary Science Conference*, page 1820, March 2016.

D. Crown, A. Yingst, S. Mest, T. Platz, H. Sizemore, D. Berman, D. Williams, T. Roatsch, F. Preusker, A. Nathues, M. Hoffman, M. Schäfer, C. Raymond, and C. Russell. Geological Mapping of the Ac-H-14 Yalode Quadrangle of Ceres from NASA's Dawn Mission. In *EGU General Assembly Conference Abstracts*, volume 18 of *EGU General Assembly Conference Abstracts*, page 9445, April 2016.

L. Czechowski. Thermal history and large scale differentiation of the Saturn's satellite Rhea. *Acta Geophysica*, 60:1192–1212, August 2012. doi: 10.2478/s11600-012-0041-9.

R. T. Daly and P. H. Schultz. Delivering a projectile component to the vestan regolith. *Icarus*, 264: 9–19, January 2016. doi: 10.1016/j.icarus.2015.08.034.

G. C. de Elía and R. P. Di Sisto. Impactor flux and cratering on Ceres and Vesta: implications for the early solar system. *Astronomy and Astrophysics*, 534:A129, October 2011. doi: 10.1051/0004-6361/201117543.

M. De Sanctis, E. Ammannito, A. Frigeri, F. Tosi, F. Zambon, C. Raymond, and C. Russell. Mineralogy of the Marcia crater on Vesta. In K. Muinonen, A. Penttilä, M. Granvik, A. Virkki, G. Fedorets, O. Wilkman, and T. Kohout, editors, *Asteroids, Comets, Meteors 2014*, July 2014.

M. C. De Sanctis, E. Ammannito, M. T. Capria, F. Tosi, F. Capaccioni, F. Zambon, F. Carraro, S. Fonte, A. Frigeri, R. Jaumann, G. Magni, S. Marchi, T. B. McCord, L. A. McFadden, H. Y. McSween, D. W. Mittlefehldt, A. Nathues, E. Palomba, C. M. Pieters, C. A. Raymond, C. T. Russell, M. J. Toplis, and D. Turrini. Spectroscopic Characterization of Mineralogy and Its Diversity Across Vesta. *Science*, 336:697, May 2012. doi: 10.1126/science.1219270.

M. C. De Sanctis, E. Ammannito, M. Ciarniello, A. Raponi, F. G. Carrozzo, A. Frigeri, A. Longobardo, E. Palomba, F. Tosi, F. Zambon, S. Fonte, M. Formisano, M. Giardino, G. Magni, F. Capaccioni, M. T. Capria, S. Marchi, C. M. Pieters, B. Ehlmann, and T. McCord. One Year of Observations of Dawn at Ceres: Composition as seen by VIR. In *EGU General Assembly Conference Abstracts*, volume 18 of *EGU General Assembly Conference Abstracts*, page 11994, April 2016a.

M. C. De Sanctis, A. Raponi, E. Ammannito, M. Ciarniello, M. J. Toplis, H. Y. McSween, J. C. Castillo-Rogez, B. L. Ehlmann, F. G. Carrozzo, S. Marchi, F. Tosi, F. Zambon, F. Capaccioni, M. T. Capria, S. Fonte, M. Formisano, A. Frigeri, M. Giardino, A. Longobardo, G. Magni, E. Palomba, L. A. McFadden, C. M. Pieters, R. Jaumann, P. Schenk, R. Mugnuolo, C. A. Raymond, and C. T. Russell. Bright carbonate deposits as evidence of aqueous alteration on (1) Ceres. *Nature*, 536: 54–57, August 2016b. doi: 10.1038/nature18290.

M. C. De Sanctis, E. Ammannito, H. Y. McSween, A. Raponi, S. Marchi, F. Capaccioni, M. T. Capria, F. G. Carrozzo, M. Ciarniello, S. Fonte, M. Formisano, A. Frigeri, M. Giardino, A. Longobardo, G. Magni, L. A. McFadden, E. Palomba, C. M. Pieters, F. Tosi, F. Zambon, C. A. Raymond, and C. T. Russell. Localized aliphatic organic material on the surface of Ceres. *Science*, 355:719–722, February 2017. doi: 10.1126/science.aaj2305.

T. Denk, G. Neukum, P. Helfenstein, P. C. Thomas, E. P. Turtle, A. S. McEwen, T. Roatsch, J. Veverka, T. V. Johnson, J. E. Perry, W. M. Owen, R. J. Wagner, C. C. Porco, and Cassini Iss Team. The First Six Months of Iapetus Observations by the Cassini ISS Camera. In S. Mackwell and E. Stansbery, editors, *36th Annual Lunar and Planetary Science Conference*, volume 36 of *Lunar and Planetary Science Conference*, March 2005.

DLR. “Wispy Streaks” on Saturn’s moon Rhea. `http://www.dlr.de/en/desktopdefault.aspx/tabid-2763/1904_read-2342/gallery-1/51_read-2/`, 2017. Accessed: 2017-07-25.

A. J. Dombard and P. M. Schenk. The Giant Cue Ball: Efficient Relaxation of Ceres’ Craters. In *Lunar and Planetary Science Conference*, volume 44 of *Lunar and Planetary Science Conference*, page 1798, March 2013.

D. T. Eppler, D. Nummedal, and R. Ehrlich. Fourier analysis of planimetric lunar crater shape - Possible guide to impact history and lunar geology. In D. J. Roddy, R. O. Pepin, and R. B. Merrill, editors, *Impact and Explosion Cratering: Planetary and Terrestrial Implications*, pages 511–526, 1977.

D. T. Eppler, R. Ehrlich, D. Nummedal, and P. H. Schultz. Sources of shape variation in lunar impact craters: Fourier shape analysis. *Geological Society of America Bulletin*, 94(2):274–291, 1983.

A. I. Ermakov, M. T. Zuber, D. E. Smith, C. A. Raymond, G. Balmino, R. R. Fu, and B. A. Ivanov. Constraints on Vesta’s interior structure using gravity and shape models from the Dawn mission. *Icarus*, 240:146–160, September 2014. doi: 10.1016/j.icarus.2014.05.015.

F. P. Fanale and J. R. Salvail. The water regime of asteroid (1) Ceres. *Icarus*, 82:97–110, November 1989. doi: 10.1016/0019-1035(89)90026-2.

G. Faure and T.M. Mensing. *Introduction to Planetary Science: The Geological Perspective*. Springer Netherlands, 2007. ISBN 9781402055447.

G. Fielder. *Structure of the Moon’s Surface*. Pergamon Press, 1961. ISBN 978-0080095080.

G. Filacchione, F. Capaccioni, M. Ciarniello, R. N. Clark, J. N. Cuzzi, P. D. Nicholson, D. P. Cruikshank, M. M. Hedman, B. J. Buratti, J. I. Lunine, L. A. Soderblom, F. Tosi, P. Cerroni, R. H. Brown, T. B. McCord, R. Jaumann, K. Stephan, K. H. Baines, and E. Flamini. Saturn’s icy satellites and rings investigated by Cassini-VIMS: III - Radial compositional variability. *Icarus*, 220:1064–1096, August 2012. doi: 10.1016/j.icarus.2012.06.040.

C. V. Fulmer and W. A. Roberts. Rock induration and crater shape. *Icarus*, 2:452–465, 1963. doi: 10.1016/0019-1035(63)90073-3.

J. B. Garvin, S. E. H. Sakimoto, and J. J. Frawley. Craters on Mars: Global Geometric Properties from Gridded MOLA Topography. In A. L. Albee and H. H. Kieffer, editors, *Sixth International Conference on Mars*, July 2003.

R. W. Gaskell. SPC Shape and Topography of Vesta from DAWN Imaging Data. In *AAS/Division for Planetary Sciences Meeting Abstracts*, volume 44 of *AAS/Division for Planetary Sciences Meeting Abstracts*, page 209.03, October 2012.

D. E. Gault, W. L. Quaide, and V. R. Oberbeck. Impact cratering mechanics and structures. In R. Greeley and P. H. Schultz, editors, *A Primer in Lunar Geology*, July 1974.

B. Giese, R. Wagner, G. Neukum, P. Helfenstein, and C. C. Porco. Topographic Features of Ithaca Chasma, Tethys. In S. Mackwell and E. Stansbery, editors, *37th Annual Lunar and Planetary Science Conference*, volume 37 of *Lunar and Planetary Science Conference*, March 2006.

B. Giese, R. Wagner, G. Neukum, P. Helfenstein, and P. C. Thomas. Tethys: Lithospheric thickness and heat flux from flexurally supported topography at Ithaca Chasma. *Geophysics Research Letters*, 34:L21203, November 2007. doi: 10.1029/2007GL031467.

P. Helfenstein, P. C. Thomas, J. Veverka, S. Squyres, J. A. Rathbun, T. Denk, G. Neukum, T. Roatsch, R. Wagner, J. Perry, E. Turtle, A. S. McEwen, T. V. Johnson, C. Porco, and Cassini ISS Team. Geological Features and Terrains on Enceladus as seen by Cassini ISS. In *AAS/Division for Planetary Sciences Meeting Abstracts #37*, volume 37 of *Bulletin of the American Astronomical Society*, page 701, August 2005.

A. R. Hendrix and C. J. Hansen. An Overview of Cassini UVIS Icy Satellite Results So Far. In S. Mackwell and E. Stansbery, editors, *36th Annual Lunar and Planetary Science Conference*, volume 36 of *Lunar and Planetary Science Conference*, March 2005.

R. R. Herrick and R. J. Phillips. Implications of a global survey of venusian impact craters. *Icarus*, 111:387–416, October 1994. doi: 10.1006/icar.1994.1152.

R. R. Herrick, V. L. Sharpton, M. C. Malin, S. N. Lyons, and K. Feely. Morphology and Morphometry of Impact Craters. In S. W. Bougher, D. M. Hunten, and R. J. Phillips, editors, *Venus II: Geology, Geophysics, Atmosphere, and Solar Wind Environment*, page 1015, 1997.

H. Hiesinger, O. Ruesch, D. A. Williams, A. Nathues, T. H. Prettyman, F. Tosi, M. C. De Sanctis, J. E. C. Scully, P. M. Schenk, R. Aileen Yingst, B. W. Denevi, R. Jaumann, C. A. Raymond, and C. T. Russell. An in-depth study of Marcia Crater, Vesta. In *EGU General Assembly Conference Abstracts*, volume 16 of *EGU General Assembly Conference Abstracts*, page 10635, May 2014a.

H. Hiesinger, O. Ruesch, D. A. Williams, A. Nathues, T. H. Prettyman, F. Tosi, M. C. De Sanctis, J. E. C. Scully, P. M. Schenk, R. A. Yingst, B. W. Denevi, R. Jaumann, C. A. Raymond, and C. T. Russell. Investigating Vesta's Marcia crater with Dawn data. *European Planetary Science Congress 2014*, 9:EPSC2014-701, April 2014b.

T. Öhman. *The Structural Control of Polygonal Impact Craters*. PhD thesis, University of Oulu, October 2009.

T. Öhman, M. Aittola, V.-P. Kostama, M. Hyvärinen, and J. Raitala. Polygonal impact craters in the Argyre region, Mars: Evidence for influence of target structure on the final crater morphology. *Meteoritics & Planetary Science*, 41(8):1163–1173, 2006. ISSN 1945-5100. doi: 10.1111/j.1945-5100.2006.tb00513.x.

T. Öhman, M. Aittola, J. Korteniemi, V.-P Kostama, and J. Raitala. Polygonal impact craters in the Solar System: Observations and implications. In R. L. Gibson and W. U. Reimold, editors, *Large Meteorite Impacts and Planetary Evolution IV*, volume 465, pages 51–65. Geological Society of America, September 2010. ISBN 9780813724652. doi: 10.1130/2010.2465(04).

C. J. A. Howett, J. R. Spencer, T. Hurford, A. Verbiscer, and M. Segura. PacMan returns: An electron-generated thermal anomaly on Tethys. *Icarus*, 221:1084–1088, November 2012. doi: 10.1016/j.icarus.2012.10.013.

C. J. A. Howett, J. R. Spencer, and A. Verbiscer. Thermophysical Property Variations on Saturn's icy moons: A system-wide perspective. *European Planetary Science Congress 2013*, 8:EPSC2013-358, September 2013.

C. J. A. Howett, J. R. Spencer, T. Hurford, A. Verbiscer, and M. Segura. Thermophysical property variations across Dione and Rhea. *Icarus*, 241:239–247, October 2014. doi: 10.1016/j.icarus.2014.05.047.

C. J. A. Howett, J. R. Spencer, T. Hurford, A. Verbiscer, and M. Segura. Thermal properties of Rhea's poles: Evidence for a meter-deep unconsolidated subsurface layer. *Icarus*, 272:140–148, July 2016. doi: 10.1016/j.icarus.2016.02.033.

K. H. G. Hughson, C. T. Russell, J.-P. Combe, J. E. C. Scully, T. Platz, S. Marchi, P. M. Schenk, D. L. Buczkowski, D. A. Williams, and E. Ammannito. Shedding Light on Oxo Crater: A Detailed Investigation of the Geology and Morphology of One of Ceres' Youngest Features Using Dawn Spacecraft Data. In *Lunar and Planetary Science Conference*, volume 47 of *Lunar and Planetary Science Conference*, page 2387, March 2016.

IAU. Gazetteer of Planetary Nomenclature, Planetary Names. `https://planetarynames.wr.usgs.gov/`, 2017. Accessed: 2017-04-14.

L. Iess, N. J. Rappaport, P. Tortora, J. Lunine, J. W. Armstrong, S. W. Asmar, L. Somenzi, and F. Zingoni. Gravity field and interior of Rhea from Cassini data analysis. *Icarus*, 190:585–593, October 2007. doi: 10.1016/j.icarus.2007.03.027.

R. Jaumann, D. A. Williams, D. L. Buczkowski, R. A. Yingst, F. Preusker, H. Hiesinger, N. Schmedemann, T. Kneissl, J. B. Vincent, D. T. Blewett, B. J. Buratti, U. Carsenty, B. W. Denevi, M. C. De Sanctis, W. B. Garry, H. U. Keller, E. Kersten, K. Krohn, J.-Y. Li, S. Marchi, K. D. Matz, T. B. McCord, H. Y. McSween, S. C. Mest, D. W. Mittlefehldt, S. Mottola, A. Nathues, G. Neukum, D. P. O'Brien, C. M. Pieters, T. H. Prettyman, C. A. Raymond, T. Roatsch, C. T. Russell, P. Schenk, B. E. Schmidt, F. Scholten, K. Stephan, M. V. Sykes, P. Tricarico, R. Wagner, M. T. Zuber, and H. Sierks. Vesta's Shape and Morphology. *Science*, 336:687, May 2012. doi: 10.1126/science.1219122.

R. Jaumann, A. Nass, K. Otto, K. Krohn, K. Stephan, T. B. McCord, D. A. Williams, C. A. Raymond, D. T. Blewett, H. Hiesinger, R. A. Yingst, M. C. De Sanctis, E. Palomba, T. Roatsch, K.-D. Matz, F. Preusker, F. Scholten, and C. T. Russell. The geological nature of dark material on Vesta and implications for the subsurface structure. *Icarus*, 240:3–19, September 2014. doi: 10.1016/j.icarus.2014.04.035.

JPL. JPL Small-Body Database Browser 4 Vesta. `https://ssd.jpl.nasa.gov/sbdb.cgi?sstr=4`, 2017. Accessed: 2017-06-14.

M. Jutzi, E. Asphaug, P. Gillet, J.-A. Barrat, and W. Benz. The structure of the asteroid 4 Vesta as revealed by models of planet-scale collisions. *Nature*, 494:207–210, February 2013. doi: 10.1038/nature11892.

S. Karimi and A. J. Dombard. On the possibility of viscoelastic deformation of the large south polar craters and true polar wander on the asteroid Vesta. *Journal of Geophysical Research (Planets)*, 121:1786–1797, September 2016. doi: 10.1002/2016JE005064.

K. K. Khurana, C. T. Russell, and M. K. Dougherty. Magnetic portraits of Tethys and Rhea. *Icarus*, 193:465–474, February 2008. doi: 10.1016/j.icarus.2007.08.005.

M. R. Kirchoff and P. Schenk. Impact cratering records of the mid-sized, icy saturnian satellites. *Icarus*, 206:485–497, April 2010. doi: 10.1016/j.icarus.2009.12.007.

H. Kriegel, S. Simon, U. Motschmann, J. Saur, F. M. Neubauer, and M. K. Dougherty. Hybrid simulation of moon-magnetosphere interactions at Saturn: Tethys and Enceladus. In D. N. Arabelos and C. C. Tscherning, editors, *EGU General Assembly Conference Abstracts*, volume 11 of *EGU General Assembly Conference Abstracts*, page 8388, April 2009.

K. Krohn, R. Jaumann, D. Elbeshausen, T. Kneissl, N. Schmedemann, R. Wagner, J. Voigt, K. Otto, K. D. Matz, F. Preusker, T. Roatsch, K. Stephan, C. A. Raymond, and C. T. Russell. Asymmetric craters on Vesta: Impact on sloping surfaces. *Planetary Space Science*, 103:36–56, November 2014. doi: 10.1016/j.pss.2014.04.011.

S. Kukkonen, M. Aittola, and T. Öhman. The Structural Control of Venusian Impact Crater Formation - Tectonic Case Studies. In *Lunar and Planetary Science Conference*, volume 45 of *Lunar and Planetary Science Conference*, page 2859, March 2014.

S. Kukkonen, M. Aittola, and T. Öhman. An Update on the Structural Control of Venusian Polygonal Impact Craters. In *Lunar and Planetary Science Conference*, volume 46 of *Lunar and Planetary Science Conference*, page 2005, March 2015.

L. Le Corre, V. Reddy, J. A. Sanchez, T. Dunn, E. A. Cloutis, M. R. M. Izawa, P. Mann, and A. Nathues. Exploring exogenic sources for the olivine on Asteroid (4) Vesta. *Icarus*, 258:483–499, September 2015. doi: 10.1016/j.icarus.2015.01.018.

J.-Y. Li, L. A. McFadden, J. W. Parker, E. F. Young, S. A. Stern, P. C. Thomas, C. T. Russell, and M. V. Sykes. Photometric analysis of 1 Ceres and surface mapping from HST observations. *Icarus*, 182:143–160, May 2006. doi: 10.1016/j.icarus.2005.12.012.

D.R. Lide. *CRC Handbook of Chemistry and Physics, 86th Edition*. Taylor & Francis, 2005. ISBN 9780849304866.

A. Longobardo, E. Palomba, M. C. De Sanctis, A. Zinzi, J. E. C. Scully, F. Capaccioni, F. Tosi, F. Zambon, E. Ammannito, J.-P. Combe, C. A. Raymond, and C. T. Russell. Mineralogical and spectral analysis of Vesta's Gegania and Lucaria quadrangles and comparative analysis of their key features. *Icarus*, 259:72–90, October 2015. doi: 10.1016/j.icarus.2015.04.031.

S. Marchi, H. Y. McSween, D. O'Brien, P. Schenk, M. C. De Sanctis, R. Gaskell, H. Hiesinger, R. Jaumann, S. Mottola, F. Preusker, C. A. Raymond, T. Roatsch, C. T. Russell, and R. A. Yingst. Vesta Collisional History Revealed by Dawn: Building a Vesta Global Crater Catalog. In *Lunar and Planetary Science Conference*, volume 43 of *Lunar and Planetary Science Conference*, page 1617, March 2012a.

S. Marchi, H. Y. McSween, D. P. O'Brien, P. Schenk, M. C. De Sanctis, R. Gaskell, R. Jaumann, S. Mottola, F. Preusker, C. A. Raymond, T. Roatsch, and C. T. Russell. The Violent Collisional History of Asteroid 4 Vesta. *Science*, 336:690, May 2012b. doi: 10.1126/science.1218757.

S. Marchi, W. F. Bottke, D. P. O'Brien, P. Schenk, S. Mottola, M. C. De Sanctis, D. A. Kring, D. A. Williams, C. A. Raymond, and C. T. Russell. Small crater populations on Vesta. *Planetary Space Science*, 103:96–103, November 2014. doi: 10.1016/j.pss.2013.05.005.

S. Marchi, D. P. O'Brien, P. Schenk, R. Fu, A. Ermakov, M. C. De Sanctis, E. Ammannito, D. A. Williams, S. C. Mest, C. A. Raymond, and C. T. Russell. Cratering on Ceres: The Puzzle of the Missing Large Craters. In *Lunar and Planetary Science Conference*, volume 47 of *Lunar and Planetary Science Conference*, page 1281, March 2016.

T. B. McCord and C. Sotin. Ceres: Evolution and current state. *Journal of Geophysical Research (Planets)*, 110:E05009, May 2005. doi: 10.1029/2004JE002244.

H. Y. McSween, D. W. Mittlefehldt, A. W. Beck, R. G. Mayne, and T. J. McCoy. HED Meteorites and Their Relationship to the Geology of Vesta and the Dawn Mission. *Space Science Reviews*, 163:141–174, December 2011. doi: 10.1007/s11214-010-9637-z.

H. Y. McSween, E. Ammannito, V. Reddy, T. H. Prettyman, A. W. Beck, M. Cristina De Sanctis, A. Nathues, L. L. Corre, D. P. O'Brien, N. Yamashita, T. J. McCoy, D. W. Mittlefehldt, M. J. Toplis, P. Schenk, E. Palomba, D. Turrini, F. Tosi, F. Zambon, A. Longobardo, F. Capaccioni, C. A. Raymond, and C. T. Russell. Composition of the Rheasilvia basin, a window into Vesta's interior. *Journal of Geophysical Research (Planets)*, 118:335–346, February 2013. doi: 10.1002/jgre.20057.

H. J. Melosh and D. Dzurisin. Mercurian global tectonics - A consequence of tidal despinning. *Icarus*, 35:227–236, August 1978. doi: 10.1016/0019-1035(78)90007-6.

H. J. Melosh and B. A. Ivanov. Impact Crater Collapse. *Annual Review of Earth and Planetary Sciences*, 27:385–415, 1999. doi: 10.1146/annurev.earth.27.1.385.

J. M. Moore and J. L. Ahern. The geology of Tethys. *Journal of Geophysics Research*, 88:A577–A584, January 1983. doi: 10.1029/JB088iS02p0A577.

J. M. Moore, V. M. Horner, and R. Greeley. The geomorphology of Rhea: implications for geologic history and surface processes. *Journal of Geophysics Research*, 90:C785–C795, January 1985. doi: 10.1029/JB090iS02p0C785.

J. M. Moore, P. M. Schenk, L. S. Bruesch, E. Asphaug, and W. B. McKinnon. Large impact features on middle-sized icy satellites. *Icarus*, 171:421–443, October 2004. doi: 10.1016/j.icarus.2004.05.009.

NASA. Meteor Crater (Barringer Crater). `https://solarsystem.nasa.gov/galleries/meteor-crater-barringer-crater`, 2004. Accessed: 2017-09-18.

NASA. PIA08400: The Crown of Tethys. `https://photojournal.jpl.nasa.gov/catalog/PIA08400`, 2007. Accessed: 2017-07-26.

NASA. PIA09861: A Stressed Surface. `https://photojournal.jpl.nasa.gov/catalog/PIA09861`, 2008. Accessed: 2017-07-25.

NASA. Well Lit Rhea. `https://www.nasa.gov/mission_pages/cassini/multimedia/pia12648.html`, 2010. Accessed: 2017-07-23.

NASA. Cassini Finds a Video Gamers' Paradise at Saturn. `https://saturn.jpl.nasa.gov/news/2745/cassini-finds-a-video-gamers-paradise-at-saturn/`, 2012. Accessed: 2017-07-26.

NASA. Flying Over Dione. `https://solarsystem.nasa.gov/galleries/flying-over-dione`, 2013. Accessed: 2017-07-25.

NASA. Saturnian Satellite Fact Sheet. `https://nssdc.gsfc.nasa.gov/planetary/factsheet/saturniansatfact.html`, 2015. Accessed: 2016-12-04.

NASA. A Moon's Contrasts. `https://www.nasa.gov/image-feature/jpl/pia20492/a-moons-contrasts`, 2016. Accessed: 2017-07-25.

NASA. Rays of Creusa. `https://www.nasa.gov/image-feature/jpl/pia20521/rays-of-creusa`, 2017. Accessed: 2017-07-25.

NASA Ceres. Ceres: In Depth. `https://solarsystem.nasa.gov/planets/ceres/indepth`, 2017. Accessed: 2017-04-23.

NASA Dione. Dione: In Depth. `https://solarsystem.nasa.gov/planets/dione/indepth`, 2017. Accessed: 2017-04-26.

NASA JPL. Full View of Asteroid Vesta. `https://www.nasa.gov/mission_pages/dawn/multimedia/pia15678.html`, 2013. Accessed: 2017-06-14.

NASA JPL. Dawn Survey Orbit Image 10. `https://www.nasa.gov/jpl/pia19578/dawn-survey-orbit-image-10`, 2015. Accessed: 2017-07-28.

NASA JPL. Ceres: By the Numbers. `https://solarsystem.nasa.gov/planets/ceres/facts`, 2016a. Accessed: 2017-06-20.

NASA JPL. Dione: By the Numbers. `https://solarsystem.nasa.gov/planets/dione/facts`, 2016b. Accessed: 2016-12-10.

NASA JPL. Rhea: By the Numbers. https://solarsystem.nasa.gov/planets/rhea/facts, 2017. Accessed: 2017-04-21.

NASA Rhea. Rhea: In Depth. https://solarsystem.nasa.gov/planets/rhea/indepth, 2017. Accessed: 2017-09-18.

NASA Tethys. Tethys: In Depth. https://solarsystem.nasa.gov/planets/tethys/indepth, 2017. Accessed: 2017-07-26.

NASA Vesta. 4 Vesta: In Depth. https://solarsystem.nasa.gov/planets/4vesta/indepth, 2017. Accessed: 2017-05-12.

NASA/JPL. Dawn Takes a Closer Look at Occator. https://www.nasa.gov/image-feature/jpl/dawn-takes-a-closer-look-at-occator, 2015a. Accessed: 2017-07-28.

NASA/JPL. Occator Crater in Perspective. https://www.nasa.gov/image-feature/jpl/pia20179/occator-crater-in-perspective, 2015b. Accessed: 2017-07-28.

NASA/JPL. Ahuna Mons on Ceres Seen From Low-Altitude Mapping Orbit. https://www.nasa.gov/image-feature/jpl/pia20348/ahuna-mons-seen-from-lamo, 2016a. Accessed: 2017-07-28.

NASA/JPL. Ceres' Mountain Ahuna Mons: Side View. https://www.nasa.gov/image-feature/jpl/pia20915/ahuna-mons-side-view, 2016b. Accessed: 2017-07-28.

NASA/JPL. Topographic cross-sectional profile across Rheasilvia impact basin. https://dawn.jpl.nasa.gov/multimedia/images/slide4_image.jpg, 2017a. Accessed: 2017-06-14.

NASA/JPL. Dawn discovers surprise 2nd giant south pole impact basin at strikingly dichotomous Vesta. https://www.universetoday.com/wp-content/uploads/2011/10/slide2_image.jpg, 2017b. Accessed: 2017-06-14.

NASA/JPL. Colorized shaded-relief map showing identification of older 375-kilometer-wide impact basin beneath more recent Rheasilvia impact structure. https://dawn.jpl.nasa.gov/multimedia/images/slide5_image.jpg, 2017c. Accessed: 2017-06-14.

NASA/JPL. Sinuous Gullies, Close-up. https://dawn.jpl.nasa.gov/multimedia/sinuous_gullies_close-up.asp, 2017d. Accessed: 2017-06-14.

NASA/JPL. Dawn Image of the Day / August 2011. https://dawn.jpl.nasa.gov/multimedia/image_of_the_day_Aug11.asp, 2017e. Accessed: 2017-06-14.

NASA/JPL. Numisia. https://dawn.jpl.nasa.gov/multimedia/numisiaI.asp, 2017f. Accessed: 2017-06-14.

A. Nathues, M. Hoffmann, M. Schaefer, L. Le Corre, V. Reddy, T. Platz, E. A. Cloutis, U. Christensen, T. Kneissl, J.-Y. Li, K. Mengel, N. Schmedemann, T. Schaefer, C. T. Russell, D. M. Applin, D. L. Buczkowski, M. R. M. Izawa, H. U. Keller, D. P. O'Brien, C. M. Pieters, C. A. Raymond, J. Ripken, P. M. Schenk, B. E. Schmidt, H. Sierks, M. V. Sykes, G. S. Thangjam, and J.-B. Vincent. Sublimation in bright spots on (1) Ceres. *Nature*, 528:237–240, December 2015. doi: 10.1038/nature15754.

A. Neesemann, T. Kneissl, N. Schmedemann, S. Walter, C. Raymond, and C. T. Russell. Size-Frequency Distributions of Small Impact Craters on Vesta - Implications for Secondary Cratering. In *Lunar and Planetary Science Conference*, volume 45 of *Lunar and Planetary Science Conference*, page 1712, March 2014.

T. Neidhart, J. Leitner, and M. Firneis. Polygonal Impact Craters on selected Minor Bodies: Rhea, Dione, Tethys, Ceres, and Vesta. In *EGU General Assembly Conference Abstracts*, volume 19 of *EGU General Assembly Conference Abstracts*, page 10081, April 2017a.

T. Neidhart, J. J. Leitner, and M. G. Firneis. Polygonal Impact Craters on Rhea, Dione, Tethys, Ceres, and Vesta. In *Lunar and Planetary Science Conference*, volume 48 of *Lunar and Planetary Science Conference*, page 1625, March 2017b.

D. P. O'Brien, S. Marchi, A. Morbidelli, W. F. Bottke, P. M. Schenk, C. T. Russell, and C. A. Raymond. Constraining the cratering chronology of Vesta. *Planetary Space Science*, 103:131–142, November 2014. doi: 10.1016/j.pss.2014.05.013.

T. Öhman, M. Aittola, V.-P. Kostama, and J. Raitala. Polygonal Impact Craters as an Indicator of Fracturing – An Example from Greater Hellas Region, Mars. In S. Mackwell and E. Stansbery, editors, *Lunar and Planetary Science Conference*, volume 34 of *Lunar and Planetary Science Conference*, March 2003.

T. Öhman, M. Aittola, V.-P. Kostama, J. Raitala, and J. Korteniemi. Polygonal impact craters in Argyre region, Mars: Implications for geology and cratering mechanics. *Meteoritics and Planetary Science*, 43:1605–1628, October 2008. doi: 10.1111/j.1945-5100.2008.tb00632.x.

S. J. Ostro, R. D. West, L. C. Wye, H. A. Zebker, M. A. Janssen, B. Stiles, K. Kelleher, Y. Z. Anderson, R. A. Boehmer, P. Callahan, Y. Gim, G. A. Hamilton, W. T. K. Johnson, C. Veeramachaneni, R. D. Lorenz, and The Cassini Radar Team. New Cassini RADAR results for Saturn's icy satellites. *Icarus*, 206:498–506, April 2010. doi: 10.1016/j.icarus.2009.07.041.

K. A. Otto, R. Jaumann, K. Krohn, D. L. Buczkowski, I. von der Gathen, E. Kersten, S. Mest, A. Nass, A. Neesemann, F. Preusker, T. Roatsch, S. E. Schröder, F. Schulzeck, J. E. C. Scully, K. Stephan, R. Wagner, D. A. Williams, C. A. Raymond, and C. T. Russell. Origin and Distribution of Polygonal Craters on (1) Ceres. In *Lunar and Planetary Science Conference*, volume 47 of *Lunar and Planetary Science Conference*, page 1493, March 2016.

E. Palomba, A. Longobardo, M. C. De Sanctis, F. Zambon, F. Tosi, E. Ammannito, F. Capaccioni, A. Frigeri, M. T. Capria, E. A. Cloutis, R. Jaumann, J.-P. Combe, C. A. Raymond, and C. T. Russell. Composition and mineralogy of dark material units on Vesta. *Icarus*, 240:58–72, September 2014. doi: 10.1016/j.icarus.2014.04.040.

E. Palomba, A. Longobardo, M. C. De Sanctis, A. Zinzi, E. Ammannito, S. Marchi, F. Tosi, F. Zambon, M. T. Capria, C. T. Russell, C. A. Raymond, and E. A. Cloutis. Detection of new olivine-rich locations on Vesta. *Icarus*, 258:120–134, September 2015. doi: 10.1016/j.icarus.2015.06.011.

R. S. Park, A. S. Konopliv, B. G. Bills, N. Rambaux, J. C. Castillo-Rogez, C. A. Raymond, A. T. Vaughan, A. I. Ermakov, M. T. Zuber, R. R. Fu, M. J. Toplis, C. T. Russell, A. Nathues, and

F. Preusker. A partially differentiated interior for (1) Ceres deduced from its gravity field and shape. *Nature*, 537:515–517, September 2016. doi: 10.1038/nature18955.

R. J. Pike. Genetic Implications of the Shapes of Martian and Lunar Craters. *Icarus*, 15:384–395, December 1971. doi: 10.1016/0019-1035(71)90117-5.

R. J. Pike. Size-dependence in the shape of fresh impact craters on the moon. In D. J. Roddy, R. O. Pepin, and R. B. Merrill, editors, *Impact and Explosion Cratering: Planetary and Terrestrial Implications*, pages 489–509, 1977.

R. J. Pike. Formation of complex impact craters - Evidence from Mars and other planets. *Icarus*, 43:1–19, July 1980. doi: 10.1016/0019-1035(80)90083-4.

Planetary Society. Map of the Moon's crustal density inferred from GRAIL's gravity map. `http://www.planetary.org/multimedia/space-images/earth/moon-crust-density-grail.html`, December 2012. Accessed: 2017-09-20.

T. Platz, A. Nathues, M. Schäfer, M. Hoffmann, T. Kneissl, N. Schmedemann, J.-B. Vincent, I. Büttner, P. Gutierrez-Marques, J. Ripken, C. T. Russell, T. Schäfer, and G. S. Thangjam. Dawn Framing Camera: Morphology and morphometry of impact craters on Ceres. *European Planetary Science Congress 2015*, 10:EPSC2015-466, October 2015.

T. Platz, A. Nathues, M. Schaefer, P. Schenk, T. Kneissl, M. Hoffmann, N. Schmedemann, H. Hiesinger, M. V. Sykes, C. A. Raymond, and C. T. Russell. Impact Cratering on Ceres: The Simple-to-Complex Transition. In *Lunar and Planetary Science Conference*, volume 47 of *Lunar and Planetary Science Conference*, page 2308, March 2016.

M. H. Poelchau, T. Kenkmann, and D. A. Kring. Rim uplift and crater shape in Meteor Crater: Effects of target heterogeneities and trajectory obliquity. *Journal of Geophysical Research (Planets)*, 114:E01006, January 2009. doi: 10.1029/2008JE003235.

H. A. Pohn and T. W. Offield. Lunar crater morphology and relative age determination of lunar geologic units - Part 1, Classification. In *Geological Survey Research 1970 - Chapter C*, pages C153–C162. U.S. Geological Survey, 1970.

C. C. Porco, E. Baker, J. Barbara, K. Beurle, A. Brahic, J. A. Burns, S. Charnoz, N. Cooper, D. D. Dawson, A. D. Del Genio, T. Denk, L. Dones, U. Dyudina, M. W. Evans, B. Giese, K. Grazier, P. Helfenstein, A. P. Ingersoll, R. A. Jacobson, T. V. Johnson, A. McEwen, C. D. Murray, G. Neukum, W. M. Owen, J. Perry, T. Roatsch, J. Spitale, S. Squyres, P. C. Thomas, M. Tiscareno, E. Turtle, A. R. Vasavada, J. Veverka, R. Wagner, and R. West. Cassini Imaging Science: Initial Results on Phoebe and Iapetus. *Science*, 307:1237–1242, February 2005. doi: 10.1126/science.1107981.

T. H. Prettyman, D. W. Mittlefehldt, N. Yamashita, A. W. Beck, W. C. Feldman, J. S. Hendricks, D. J. Lawrence, T. J. McCoy, H. Y. McSween, P. N. Peplowski, R. C. Reedy, M. J. Toplis, L. Corre, H. Mizzon, V. Reddy, T. N. Titus, C. A. Raymond, and C. T. Russell. Neutron absorption constraints on the composition of 4 Vesta. *Meteoritics and Planetary Science*, 48:2211–2236, November 2013. doi: 10.1111/maps.12244.

T. H. Prettyman, N. Yamashita, R. C. Reedy, H. Y. McSween, D. W. Mittlefehldt, J. S. Hendricks, and M. J. Toplis. Concentrations of potassium and thorium within Vesta's regolith. *Icarus*, 259: 39–52, October 2015. doi: 10.1016/j.icarus.2015.05.035.

L. Prockter, P. Thomas, M. Robinson, J. Joseph, A. Milne, B. Bussey, J. Veverka, and A. Cheng. Surface Expressions of Structural Features on Eros. *Icarus*, 155:75–93, January 2002. doi: 10. 1006/icar.2001.6770.

W. L. Quaide, D. E. Gault, and R. A. Schmidt. Gravitative effects on lunar impact structures. *Annals of the New York Academy of Sciences*, 123:563–572, November 1965. doi: 10.1111/j.1749-6632.1965. tb20388.x.

J. Raitala. The bedrock of the Vaasa circular structure, western Finland. *Earth Moon and Planets*, 33:133–155, October 1985. doi: 10.1007/BF00116791.

C. A. Raymond, R. S. Park, S. W. Asmar, A. S. Konopliv, D. L. Buczkowski, M. C. De Sanctis, H. Y. McSween, C. T. Russell, R. Jaumann, and F. Preusker. The Crust and Mantle of Vesta's Southern Hemisphere. *European Planetary Science Congress 2013*, 8:EPSC2013-1002, September 2013.

C. A. Raymond, S. Marchi, M. T. Bland, J. C. Castillo-Rogez, R. S. Park, C. T. Russell, K. G. Hughson, and J. E. C. Scully. Regional Heterogenity In Ceres' Subsurface. In *EGU General Assembly Conference Abstracts*, volume 18 of *EGU General Assembly Conference Abstracts*, page 11045, April 2016.

T. Roatsch, M. Wählisch, A. Hoffmeister, E. Kersten, K.-D. Matz, F. Scholten, R. Wagner, T. Denk, G. Neukum, P. Helfenstein, and C. Porco. High-resolution Atlases of Mimas, Tethys, and Iapetus derived from Cassini-ISS images. *Planetary Space Science*, 57:83–92, January 2009. doi: 10.1016/ j.pss.2008.10.014.

D. J. Roddy. Pre-Impact Conditions and Cratering Processes at Meteor Crater, Arizona, a Typical Bowl-Shaped Crater. In *Lunar and Planetary Science Conference Proceedings*, volume 9 of *Lunar and Planetary Science Conference Proceedings*, 1978.

L. B. Ronca and J. W. Salisbury. Lunar history as suggested by the circularity index of lunar craters. *Icarus*, 5:130–138, 1966. doi: 10.1016/0019-1035(66)90016-9.

E. M. Royer and A. R. Hendrix. Far-Ultraviolet Photometric Characteristics of Tethys, Dione and Mimas. In *Lunar and Planetary Science Conference*, volume 44 of *Lunar and Planetary Science Conference*, page 2338, March 2013.

O. Ruesch, H. Hiesinger, D. T. Blewett, D. A. Williams, D. Buczkowski, J. Scully, R. A. Yingst, T. Roatsch, F. Preusker, R. Jaumann, C. T. Russell, and C. A. Raymond. Geologic map of the northern hemisphere of Vesta based on Dawn Framing Camera (FC) images. *Icarus*, 244:41–59, December 2014a. doi: 10.1016/j.icarus.2014.01.035.

O. Ruesch, H. Hiesinger, M. C. De Sanctis, E. Ammannito, E. Palomba, A. Longobardo, F. Zambon, F. Tosi, M. T. Capria, F. Capaccioni, A. Frigeri, S. Fonte, G. Magni, C. A. Raymond, and C. T.

Russell. Detections and geologic context of local enrichments in olivine on Vesta with VIR/Dawn data. *Journal of Geophysical Research (Planets)*, 119:2078–2108, September 2014b. doi: 10.1002/2014JE004625.

O. Ruesch, H. Hiesinger, D. A. Williams, A. Nathues, T. H. Prettyman, F. Tosi, M. C. De Sanctis, J. E. C. Scully, P. M. Schenk, R. A. Yingst, B. W. Denevi, R. Jaumann, C. A. Raymond, and C. T. Russell. Marcia Crater, Vesta: Geology, Mineralogy, Composition, and Thermal Properties. In *Lunar and Planetary Science Conference*, volume 45 of *Lunar and Planetary Science Conference*, page 2010, March 2014c.

O. Ruesch, T. Platz, P. Schenk, L. A. McFadden, J. C. Castillo-Rogez, L. C. Quick, S. Byrne, F. Preusker, D. P. O'Brien, N. Schmedemann, D. A. Williams, J.-Y. Li, M. T. Bland, H. Hiesinger, T. Kneissl, A. Neesemann, M. Schaefer, J. H. Pasckert, B. E. Schmidt, D. L. Buczkowski, M. V. Sykes, A. Nathues, T. Roatsch, M. Hoffmann, C. A. Raymond, and C. T. Russell. Cryovolcanism on Ceres. *Science*, 353:aaf4286, September 2016. doi: 10.1126/science.aaf4286.

C. T. Russell, C. A. Raymond, A. Coradini, H. Y. McSween, M. T. Zuber, A. Nathues, M. C. De Sanctis, R. Jaumann, A. S. Konopliv, F. Preusker, S. W. Asmar, R. S. Park, R. Gaskell, H. U. Keller, S. Mottola, T. Roatsch, J. E. C. Scully, D. E. Smith, P. Tricarico, M. J. Toplis, U. R. Christensen, W. C. Feldman, D. J. Lawrence, T. J. McCoy, T. H. Prettyman, R. C. Reedy, M. E. Sykes, and T. N. Titus. Dawn at Vesta: Testing the Protoplanetary Paradigm. *Science*, 336:684, May 2012. doi: 10.1126/science.1219381.

C. T. Russell, C. A. Raymond, R. Jaumann, H. Y. McSween, M. C. De Sanctis, A. Nathues, T. H. Prettyman, E. Ammannito, V. Reddy, F. Preusker, D. P. O'Brien, S. Marchi, B. W. Denevi, D. L. Buczkowski, C. M. Pieters, T. B. McCord, J.-Y. Li, D. W. Mittlefehldt, J.-P. Combe, D. A. Williams, H. Hiesinger, R. A. Yingst, C. A. Polanskey, and S. P. Joy. Dawn completes its mission at 4 Vesta. *Meteoritics and Planetary Science*, 48:2076–2089, November 2013. doi: 10.1111/maps.12091.

C. T. Russell, C. A. Raymond, and Dawn Science Team. Dawn mission to (4) Vesta and (1) Ceres. In K. Muinonen, A. Penttilä, M. Granvik, A. Virkki, G. Fedorets, O. Wilkman, and T. Kohout, editors, *Asteroids, Comets, Meteors 2014*, July 2014a.

C. T. Russell, C. A. Raymond, H. Y. McSween, R. Jaumann, M. C. DeSanctis, A. Nathues, T. Prettyman, M. T. Capria, C. Pieters, L. McFadden, E. Ammannito, M. V. Sykes, T. B. McCord, M. Zuber, D. Smith, M. Hoffman, J. E. C. Scully, and D. Buczkowski. Lessons from Vesta and Ceres. *European Planetary Science Congress 2014, EPSC Abstracts, Vol. 9, id. EPSC2014-18*, 9: EPSC2014-18, April 2014b.

C. T. Russell, C. A. Raymond, E. Ammannito, D. L. Buczkowski, M. C. DeSanctis, H. Hiesinger, R. Jaumann, H. Y. McSween, A. Nathues, R. S. Park, and C. M. Pieters. Exploration of a Small Volatile-Rich World: New Light on Ceres. In *EGU General Assembly Conference Abstracts*, volume 18 of *EGU General Assembly Conference Abstracts*, page 5093, April 2016.

M. Schäfer, T. Schäfer, E. A. Cloutis, M. R. M. Izawa, T. Platz, J. C. Castillo-Rogez, M. Hoffmann, G. S. Thangjam, T. Kneissl, A. Nathues, K. Mengel, D. A. Williams, J. Kallisch, J. Ripken, and

C. T. Russell. Ceres' Yellow Spots - Observations with Dawn Framing Camera. In *EGU General Assembly Conference Abstracts*, volume 18 of *EGU General Assembly Conference Abstracts*, page 14495, April 2016.

P. Schenk, S. Marchi, D. P. O'Brien, J. B. Vincent, R. Jaumann, R. Gaskell, T. Roatsch, H. Keller, B. W. Denevi, C. A. Raymond, and C. T. Russell. Impact Cratering on a Mid-Sized Planetary Body: Insights from Morphology as seen by Dawn at Vesta. In *Lunar and Planetary Science Conference*, volume 43 of *Lunar and Planetary Science Conference*, page 2677, March 2012a.

P. Schenk, D. P. O'Brien, S. Marchi, R. Gaskell, F. Preusker, T. Roatsch, R. Jaumann, D. Buczkowski, T. McCord, H. Y. McSween, D. Williams, A. Yingst, C. Raymond, and C. Russell. The Geologically Recent Giant Impact Basins at Vesta's South Pole. *Science*, 336:694, May 2012b. doi: 10.1126/science.1223272.

P. Schenk, J.-B. Vincent, D. P. O'Brien, R. Jaumann, and D. Williams. Impact crater morphologies on Vesta. In *European Planetary Science Congress 2012*, pages EPSC2012–700, September 2012c.

P. Schenk, J.-B. Vincent, V. Bray, and G. Kramer. Cratering on a Small Planet: Morphologies of Fresh Craters and the Simple-Complex Transition on Vesta. In *Vesta in the Light of Dawn: First Exploration of a Protoplanet in the Asteroid Belt*, volume 1773 of *LPI Contributions*, page 2042, February 2014.

P. Schenk, S. Marchi, D. O'Brien, K. Otto, R. Jaumann, D. Williams, C. Raymond, and C. Russell. Impact Craters on Ceres: Evidence for Water-Ice Mantle? *European Planetary Science Congress 2015*, 10:EPSC2015-400, October 2015.

P. Schenk, S. Marchi, D. O'Brien, M. Bland, T. Platz, T. Hoogenboom, G. Kramer, S. Schroeder, M. De Sanctis, D. Buczkowski, M. Sykes, L. McFadden, O. Ruesch, L. Le Corre, B. Schmidt, K. Hughson, C. T. Russell, J. Scully, and C. Raymond. Impact Cratering on the Small Planets Ceres and Vesta: S-C Transitions, Central Pits, and the Origin of Bright Spots. In *Lunar and Planetary Science Conference*, volume 47 of *Lunar and Planetary Science Conference*, page 2697, March 2016.

N. Schmedemann, T. Kneissl, B. A. Ivanov, G. G. Michael, R. J. Wagner, G. Neukum, O. Ruesch, H. Hiesinger, K. Krohn, T. Roatsch, F. Preusker, H. Sierks, R. Jaumann, V. Reddy, A. Nathues, S. H. G. Walter, A. Neesemann, C. A. Raymond, and C. T. Russell. The cratering record, chronology and surface ages of (4) Vesta in comparison to smaller asteroids and the ages of HED meteorites. *Planetary Space Science*, 103:104–130, November 2014. doi: 10.1016/j.pss.2014.04.004.

N. Schmedemann, G. Michael, B. A. Ivanov, T. Kneissl, A. Neesemann, H. Hiesinger, R. Jaumann, C. A. Raymond, and C. T. Russell. Preliminary Results from Initial Investigations of Ceres' Cratering Record from Dawn Imaging Data. In *EGU General Assembly Conference Abstracts*, volume 17 of *EGU General Assembly Conference Abstracts*, page 6486, April 2015.

J. Schön. *Petrophysik: Physikalische Eigenschaften von Gesteinen und Mineralen.* Enke, 1983. ISBN 3-432-92971-4.

F. Scipioni, F. Tosi, F. Capaccioni, P. Cerroni, K. Stephan, and G. Filacchione. Spectroscopic identification and comparison of Dione's and Rhea's terrain based on Cassini VIMS data. In *European Planetary Science Congress 2012*, pages EPSC2012–640, September 2012.

F. Scipioni, F. Tosi, M. Ciarniello, F. Capaccioni, G. Filacchione, K. Stephan, and P. Cerroni. Spectroscopic Identification and Classification of Terrain Units on Dione's and Rhea's Surfaces Based on Cassini/Vims Data. In *Lunar and Planetary Science Conference*, volume 44 of *Lunar and Planetary Science Conference*, page 1995, March 2013.

F. Scipioni, F. Tosi, K. Stephan, G. Filacchione, M. Ciarniello, F. Capaccioni, and P. Cerroni. Spectroscopic classification of icy satellites of Saturn II: Identification of terrain units on Rhea. *Icarus*, 234:1–16, May 2014. doi: 10.1016/j.icarus.2014.02.010.

F. Scipioni, P. Schenk, and F. Tosi. Spectroscopic Variation of Water Ice Abundance and Sub-Micron Ice Grains Across Enceladus, Mimas, and Tethys' Surface Using Cassini VIMS Data. In *Lunar and Planetary Science Conference*, volume 46 of *Lunar and Planetary Science Conference*, page 1919, March 2015.

J. E. C. Scully, A. Yin, C. T. Russell, D. L. Buczkowski, D. A. Williams, D. T. Blewett, O. Ruesch, H. Hiesinger, L. Le Corre, C. Mercer, R. A. Yingst, W. B. Garry, R. Jaumann, T. Roatsch, F. Preusker, R. W. Gaskell, S. E. Schröder, E. Ammannito, C. M. Pieters, and C. A. Raymond. Geomorphology and structural geology of Saturnalia Fossae and adjacent structures in the northern hemisphere of Vesta. *Icarus*, 244:23–40, December 2014. doi: 10.1016/j.icarus.2014.01.013.

J. E. C. Scully, D. L. Buczkowski, D. A. Williams, S. C. Mest, C. A. Raymond, J.-P. Combe, A. Neesemann, J. H. Pasckert, K. Hughson, T. Kneissl, O. Ruesch, A. Frigeri, C. T. Russell, A. Naas, A. Ermakov, R. Jaumann, M. Hoffmann, A. Nathues, R. Park, C. M. Pieters, T. Platz, F. Preusker, T. Roatsch, and M. Schaefer. Geologic History of the Ezinu Quadrangle of Ceres, Derived from a Geologic Map Based on Data from the Dawn Mission. In *Annual Planetary Geologic Mappers Meeting*, volume 1920 of *LPI Contributions*, page 7018, June 2016.

E. M. Shoemaker. *Impact Mechanics at Meteor Crater, Arizona.* 1963.

E.M. Shoemaker. *Penetration Mechanics of High Velocity Meteorites: Illustrated by Meteor Crater, Arizona.* Berlingske bogtr., 1960.

B. A. Smith, L. Soderblom, R. F. Beebe, J. M. Boyce, G. Briggs, A. Bunker, S. A. Collins, C. Hansen, T. V. Johnson, J. L. Mitchell, R. J. Terrile, M. H. Carr, A. F. Cook, J. N. Cuzzi, J. B. Pollack, G. E. Danielson, A. P. Ingersoll, M. E. Davies, G. E. Hunt, H. Masursky, E. M. Shoemaker, D. Morrison, T. Owen, C. Sagan, J. Veverka, R. Strom, and V. E. Suomi. Encounter with Saturn - Voyager 1 imaging science results. *Science*, 212:163–191, April 1981. doi: 10.1126/science.212.4491.163.

B. A. Smith, L. Soderblom, R. M. Batson, P. M. Bridges, J. L. Inge, H. Masursky, E. Shoemaker, R. F. Beebe, J. Boyce, G. Briggs, A. Bunker, S. A. Collins, C. Hansen, T. V. Johnson, J. L. Mitchell, R. J. Terrile, A. F. Cook, J. N. Cuzzi, J. B. Pollack, G. E. Danielson, A. P. Ingersoll, M. E. Davies, G. E. Hunt, D. Morrison, T. Owen, C. Sagan, J. Veverka, R. Strom, and V. E. Suomi. A new look at the Saturn system - The Voyager 2 images. *Science*, 215:504–537, January 1982. doi: 10.1126/science.215.4532.504.

K. Stephan, R. Jaumann, R. Wagner, R. N. Clark, D. P. Cruikshank, B. Giese, C. A. Hibbitts, T. Roatsch, K.-D. Matz, R. H. Brown, G. Filacchione, F. Cappacioni, F. Scholten, B. J. Buratti, G. B. Hansen, P. D. Nicholson, K. H. Baines, R. M. Nelson, and D. L. Matson. The Saturnian satellite Rhea as seen by Cassini VIMS. *Planetary Space Science*, 61:142–160, February 2012. doi: 10.1016/j.pss.2011.07.019.

K. Stephan, R. Jaumann, R. Wagner, R. N. Clark, D. P. Cruikshank, C. Dalle Ore, G. B. Hansen, R. H. Brown, B. Giese, T. Roatsch, D. Matson, K. Baines, G. Filiacchione, S. Rodriguez, B. J. Buratti, P. D. Nicholson, and C. Sotin. The Saturnian satellite Tethys observed by the Cassini-VIMS instrument. In *EGU General Assembly Conference Abstracts*, volume 15 of *EGU General Assembly Conference Abstracts*, page 13734, April 2013.

K. Stephan, R. Jaumann, M. C. De Sanctis, F. Tosi, E. Ammannito, K. Krohn, F. Zambon, S. Marchi, O. Ruesch, K.-D. Matz, F. Preusker, T. Roatsch, C. A. Raymond, and C. T. Russell. Small fresh impact craters on asteroid 4 Vesta: A compositional and geological fingerprint. *Journal of Geophysical Research (Planets)*, 119:771–797, April 2014. doi: 10.1002/2013JE004388.

K. Stephan, R. Jaumann, R. Wagner, R. N. Clark, D. P. Cruikshank, C. Dalle Ore, R. H. Brown, B. Giese, T. Roatsch, D. Matson, K. H. Baines, G. Filacchione, F. Capaccione, B. J. Burratti, P. D. Nicholson, and S. Rodriguez. Tethys - Geological and Spectral Properties. In *EGU General Assembly Conference Abstracts*, volume 17 of *EGU General Assembly Conference Abstracts*, page 7306, April 2015.

K. Stephan, R. Wagner, R. Jaumann, R. N. Clark, D. P. Cruikshank, R. H. Brown, B. Giese, T. Roatsch, G. Filacchione, D. Matson, C. D. Ore, F. Capaccioni, K. H. Baines, S. Rodriguez, N. Krupp, B. J. Buratti, and P. D. Nicholson. Cassini's geological and compositional view of Tethys. *Icarus*, 274:1–22, August 2016. doi: 10.1016/j.icarus.2016.03.002.

R. G. Strom, M. C. Malin, and M. A. Leake. Geologic Map of the Bach (H-15) Quadrangle of Mercury: USGS Miscellaneous Investigations Series Map I-2015. In *Atlas of Mercury, 1:5,000,000*, 1990.

B. D. Teolis and J. H. Waite. Cassini discovers seasonal changes in Rhea's exosphere. In *EPSC-DPS Joint Meeting 2011*, page 1651, October 2011.

B. D. Teolis and J. H. Waite. Cassini Measurements Show Seasonal O_2 - CO_2 Exospheres and Possible Seasonal CO_2 Frosts at Rhea and Dione. In *Lunar and Planetary Science Conference*, volume 43 of *Lunar and Planetary Science Conference*, page 2923, March 2012.

B. D. Teolis and J. H. Waite. Dione and Rhea seasonal exospheres revealed by Cassini CAPS and INMS. *Icarus*, 272:277–289, July 2016. doi: 10.1016/j.icarus.2016.02.031.

B. D. Teolis, G. H. Jones, P. F. Miles, R. L. Tokar, B. A. Magee, J. H. Waite, E. Roussos, D. T. Young, F. J. Crary, A. J. Coates, R. E. Johnson, W.-L. Tseng, and R. A. Baragiola. Cassini Finds an Oxygen-Carbon Dioxide Atmosphere at Saturn's Icy Moon Rhea. *Science*, 330:1813, December 2010. doi: 10.1126/science.1198366.

B. D. Teolis, G. H. Jones, P. F. Miles, R. L. Tokar, B. A. Magee, J. H. Waite, E. Roussos, D. T. Young, F. J. Crary, A. J. Coates, R. E. Johnson, W.-L. Tseng, and R. A. Baragiola. Formation, Distribution and Loss of Rhea's O_2-CO_2 Exosphere. In *Lunar and Planetary Science Conference*, volume 42 of *Lunar and Planetary Science Conference*, page 2663, March 2011.

G. Thangjam, A. Nathues, K. Mengel, M. Hoffmann, M. Schäfer, V. Reddy, E. A. Cloutis, U. Christensen, H. Sierks, L. L. Corre, J.-B. Vincent, and C. T. Russell. Olivine-rich exposures at Bellicia and Arruntia craters on (4) Vesta from Dawn FC. *Meteoritics and Planetary Science*, 49:1831–1850, October 2014. doi: 10.1111/maps.12356.

C. Thomas, J. W. Head, and Galileo SSI Team. Morphology of Byblus Sulcus, Ganymede from Galileo SSI Data. In *Lunar and Planetary Science Conference*, volume 29 of *Lunar and Planetary Science Conference*, March 1998.

P. C. Thomas. Sizes, shapes, and derived properties of the saturnian satellites after the Cassini nominal mission. *Icarus*, 208:395–401, July 2010. doi: 10.1016/j.icarus.2010.01.025.

P. C. Thomas, R. P. Binzel, M. J. Gaffey, A. D. Storrs, E. N. Wells, and B. H. Zellner. Impact excavation on asteroid 4 Vesta: Hubble Space Telescope results. *Science*, 277:1492–1495, September 1997. doi: 10.1126/science.277.5331.1492.

P. C. Thomas, J. W. Parker, L. A. McFadden, C. T. Russell, S. A. Stern, M. V. Sykes, and E. F. Young. Differentiation of the asteroid Ceres as revealed by its shape. *Nature*, 437:224–226, September 2005. doi: 10.1038/nature03938.

P. C. Thomas, J. A. Burns, P. Helfenstein, S. Squyres, J. Veverka, C. Porco, E. P. Turtle, A. McEwen, T. Denk, B. Giese, T. Roatsch, T. V. Johnson, and R. A. Jacobson. Shapes of the saturnian icy satellites and their significance. *Icarus*, 190:573–584, October 2007. doi: 10.1016/j.icarus.2007.03.012.

M. J. Toplis, H. Mizzon, O. Forni, M. Monnereau, J. A. Barrat, T. H. Prettyman, H. Y. McSween, T. J. McCoy, D. W. Mittlefehldt, M. C. De Sanctis, C. A. Raymond, and C. T. Russell. Chondritic Models of 4 Vesta: Comparison of Predicted Internal Structure and Surface Composition/Mineralogy with Data from the Dawn Mission. In *Lunar and Planetary Science Conference*, volume 43 of *Lunar and Planetary Science Conference*, page 2152, March 2012.

P. Tortora, M. Zannoni, D. Hemingway, F. Nimmo, R. A. Jacobson, L. Iess, and M. Parisi. Rhea gravity field and interior modeling from Cassini data analysis. *Icarus*, 264:264–273, January 2016. doi: 10.1016/j.icarus.2015.09.022.

F. Tosi, M. T. Capria, M. C. De Sanctis, J.-P. Combe, F. Zambon, A. Nathues, S. E. Schröder, J.-Y. Li, E. Palomba, A. Longobardo, D. T. Blewett, B. W. Denevi, E. Palmer, F. Capaccioni, E. Ammannito, T. M. Titus, D. W. Mittlefehldt, J. M. Sunshine, C. T. Russell, and C. A. Raymond. Thermal measurements of dark and bright surface features on Vesta as derived from Dawn/VIR. *Icarus*, 240:36–57, September 2014. doi: 10.1016/j.icarus.2014.03.017.

USGS. Map a Planet 2. `https://astrogeology.usgs.gov/tools/map-a-planet-2`, 2016. Accessed: 2016-12-18.

USGS. ISIS Integrated Software for Imagers and Spectrometers. `https://isis.astrogeology.usgs.gov/`, 2017. Accessed: 2017-09-18.

P. Vernazza, T. Mothé-Diniz, M. A. Barucci, M. Birlan, J. M. Carvano, G. Strazzulla, M. Fulchignoni, and A. Migliorini. Analysis of near-IR spectra of 1 Ceres and 4 Vesta, targets of the Dawn mission. *Astronomy and Astrophysics*, 436:1113–1121, June 2005. doi: 10.1051/0004-6361:20042506.

J. Veverka, P. Thomas, A. Harch, B. Clark, J. F. Bell, III, B. Carcich, J. Joseph, C. Chapman, W. Merline, M. Robinson, M. Malin, L. A. McFadden, S. Murchie, S. E. Hawkins, III, R. Farquhar, N. Izenberg, and A. Cheng. NEAR's Flyby of 253 Mathilde: Images of a C Asteroid. *Science*, 278: 2109, December 1997. doi: 10.1126/science.278.5346.2109.

J.-B. Vincent, P. Schenk, A. Nathues, H. Sierks, M. Hoffmann, R. W. Gaskell, S. Marchi, D. P. O'Brien, M. Sykes, C. T. Russell, M. Fulchignoni, H. U. Kellerg, C. Raymond, E. Palmer, and F. Preusker. Crater depth-to-diameter distribution and surface properties of (4) Vesta. *Planetary Space Science*, 103:57–65, November 2014. doi: 10.1016/j.pss.2013.09.003.

R. Wagner, K. Stephan, N. Schmedemann, T. Roatsch, E. Kersten, G. Neukum, and C. C. Porco. Regional geology and stratigraphy of Saturn's icy moon Tethys. In *EGU General Assembly Conference Abstracts*, volume 15 of *EGU General Assembly Conference Abstracts*, pages EGU2013–11009, April 2013a.

R. J. Wagner, G. Neukum, B. Giese, T. Roatsch, T. Denk, U. Wolf, and C. C. Porco. Geology of Saturn's Satellite Rhea on the Basis of the High-Resolution Images from the Targeted Flyby 049 on Aug. 30, 2007. In *Lunar and Planetary Science Conference*, volume 39 of *Lunar and Planetary Science Conference*, page 1930, March 2008.

R. J. Wagner, B. Giese, T. Roatsch, G. Neukum, T. Denk, U. Wolf, and C. C. Porco. Tectonic features on Rhea's trailing hemisphere: a first look at the Cassini ISS camera data from orbit 121, Nov. 21, 2009. In *EGU General Assembly Conference Abstracts*, volume 12 of *EGU General Assembly Conference Abstracts*, page 6731, May 2010a.

R. J. Wagner, G. Neukum, B. Giese, T. Roatsch, T. Denk, U. Wolf, and C. C. Porco. The Geology of Rhea: A First Look at the ISS Camera Data from Orbit 121 (Nov. 21, 2009) in Cassini's Extended Mission. In *Lunar and Planetary Science Conference*, volume 41 of *Lunar and Planetary Science Conference*, page 1672, March 2010b.

R. J. Wagner, G. Neukum, U. Wolf, N. Schmedemann, T. Denk, K. Stephan, T. Roatsch, and C. C. Porco. Bright Ray Craters on Rhea and Dione. In *Lunar and Planetary Science Conference*, volume 42 of *Lunar and Planetary Science Conference*, page 2249, March 2011.

R. J. Wagner, K. Stephan, N. Schmedemann, T. Roatsch, E. Kersten, G. Neukum, and C. C. Porco. Geology and stratigraphy of Saturn's moon Tethys. *European Planetary Science Congress 2013*, 8:EPSC2013-713, September 2013b.

R. J. Wagner, N. Schmedemann, K. Stephan, R. Jaumann, T. Kneissl, A. Neesemann, K. Krohn, K. Otto, F. Preusker, E. Kersten, T. Roatsch, H. Hiesinger, D. A. Williams, A. Yingst, D. A. Crown, S. C. Mest, C. A. Raymond, and C. T. Russell. Global, regional and local stratigraphy of dwarf planet (1) Ceres: results from geologic and topographic mapping using images of the Dawn camera. In *EGU General Assembly Conference Abstracts*, volume 18 of *EGU General Assembly Conference Abstracts*, page 13328, April 2016a.

R. J. Wagner, N. Schmedemann, K. Stephan, R. Jaumann, T. Kneissl, A. Neesemann, K. Krohn, K. Otto, F. Preusker, E. Kersten, T. Roatsch, H. Hiesinger, D. A. Williams, R. A. Yingst, D. A. Crown, S. C. Mest, C. A. Raymond, and C. T. Russell. Stratigraphy of (1) Ceres from Geologic and Topographic Mapping and Crater Counts Using Images of the Dawn FC2 Camera. In *Lunar and Planetary Science Conference*, volume 47 of *Lunar and Planetary Science Conference*, page 2156, March 2016b.

W. A. Watters. Structure of Polygonal Craters at Meridiani Planum, Mars, and a Model Relating Target Structure to Crater Shape. In S. Mackwell and E. Stansbery, editors, *37th Annual Lunar and Planetary Science Conference*, volume 37 of *Lunar and Planetary Science Conference*, March 2006.

G. Weihs. Polygonal Impact Craters on Mercury. Bachelor's thesis, University of Vienna, February 2012.

G. T. Weihs, J. J. Leitner, and M. G. Firneis. Relative Age of Polygonal Impact Craters on Venus. *European Planetary Science Congress 2014, EPSC Abstracts, Vol. 9, id. EPSC2014-708*, 9:EPSC2014-708, April 2014.

G. T. Weihs, J. J. Leitner, and M. G. Firneis. Polygonal impact craters on mercury. *Planetary Space Science*, 111:77–82, June 2015. doi: 10.1016/j.pss.2015.03.014.

O. L. White and P. M. Schenk. Crater Shapes on the Saturnian Satellites: New Measurements Using Cassini Stereo Images. In *Lunar and Planetary Science Conference*, volume 42 of *Lunar and Planetary Science Conference*, page 2283, March 2011.

D. Williams, S. Mest, T. Kneissl, J. Hendrik Pasckert, H. Hiesinger, A. Neesemann, N. Schmedemann, D. Buczkowski, J. Scully, S. Marchi, P. Schenk, R. Jaumann, T. Roatsch, F. Preusker, A. Nathues, M. Schaefer, M. Hoffmann, C. Raymond, and C. Russell. Geological Mapping of the Ac-H-7 Kerwan Quadrangle of Ceres from NASA Dawn Mission. In *EGU General Assembly Conference Abstracts*, volume 18 of *EGU General Assembly Conference Abstracts*, page 8161, April 2016.

D. A. Williams, B. W. Denevi, D. W. Mittlefehldt, S. C. Mest, P. M. Schenk, R. A. Yingst, D. L. Buczkowski, J. E. C. Scully, W. B. Garry, T. B. McCord, J.-P. Combe, R. Jaumann, C. M. Pieters, A. Nathues, L. Le Corre, M. Hoffmann, V. Reddy, M. Schäfer, T. Roatsch, F. Preusker, S. Marchi, T. Kneissl, N. Schmedemann, G. Neukum, H. Hiesinger, M. C. De Sanctis, E. Ammannito, A. Frigeri, T. H. Prettyman, C. T. Russell, and C. A. Raymond. The geology of the Marcia quadrangle of asteroid Vesta: Assessing the effects of large, young craters. *Icarus*, 244: 74–88, December 2014a. doi: 10.1016/j.icarus.2014.01.033.

D. A. Williams, D. P. O'Brien, P. M. Schenk, B. W. Denevi, U. Carsenty, S. Marchi, J. E. C. Scully, R. Jaumann, M. C. De Sanctis, E. Palomba, E. Ammannito, A. Longobardo, G. Magni, A. Frigeri, C. T. Russell, C. A. Raymond, and T. M. Davison. Lobate and flow-like features on asteroid Vesta. *Planetary Space Science*, 103:24–35, November 2014b. doi: 10.1016/j.pss.2013.06.017.

D. A. Williams, R. A. Yingst, and W. B. Garry. Introduction: The geologic mapping of Vesta. *Icarus*, 244:1–12, December 2014c. doi: 10.1016/j.icarus.2014.03.001.

C. A. Wood, J. W. Head, and M. J. Cintala. Crater degradation on Mercury and the moon - Clues to surface evolution. In R. B. Merril, editor, *Lunar and Planetary Science Conference Proceedings*, volume 8 of *Lunar and Planetary Science Conference Proceedings*, pages 3503–3520, 1977.

N. Yamashita, T. H. Prettyman, D. W. Mittlefehldt, M. J. Toplis, T. J. McCoy, A. W. Beck, R. C. Reedy, W. C. Feldman, D. J. Lawrence, P. N. Peplowski, O. Forni, H. Mizzon, C. A. Raymond, and C. T. Russell. Distribution of iron on Vesta. *Meteoritics and Planetary Science*, 48:2237–2251, November 2013. doi: 10.1111/maps.12139.

R. A. Yingst, S. C. Mest, D. C. Berman, W. B. Garry, D. A. Williams, D. Buczkowski, R. Jaumann, C. M. Pieters, M. C. De Sanctis, A. Frigeri, L. Le Corre, F. Preusker, C. A. Raymond, V. Reddy, C. T. Russell, T. Roatsch, and P. M. Schenk. Geologic mapping of Vesta. *Planetary Space Science*, 103:2–23, November 2014. doi: 10.1016/j.pss.2013.12.014.

F. Zambon, M. C. De Sanctis, S. Schröder, F. Tosi, A. Longobardo, E. Ammannito, D. T. Blewett, D. W. Mittlefehldt, J.-Y. Li, E. Palomba, F. Capaccioni, A. Frigeri, M. T. Capria, S. Fonte, A. Nathues, C. M. Pieters, C. T. Russell, and C. A. Raymond. Spectral analysis of the bright materials on the asteroid Vesta. *Icarus*, 240:73–85, September 2014. doi: 10.1016/j.icarus.2014.04.037.

N. E. B. Zellner, S. Gibbard, I. de Pater, F. Marchis, and M. J. Gaffey. Near-IR imaging of Asteroid 4 Vesta. *Icarus*, 177:190–195, September 2005. doi: 10.1016/j.icarus.2005.03.024.

M. Zolotov. Planetary science: Salty Ceres. *Nature Geoscience*, 9:476–477, July 2016. doi: 10.1038/ngeo2756.

M. T. Zuber, D. E. Smith, A. F. Cheng, J. B. Garvin, O. Aharonson, T. D. Cole, P. J. Dunn, Y. Guo, F. G. Lemoine, G. A. Neumann, D. D. Rowlands, and M. H. Torrence. The Shape of 433 Eros from the NEAR-Shoemaker Laser Rangefinder. *Science*, 289:2097–2101, September 2000. doi: 10.1126/science.289.5487.2097.